Electrowetting Liquid Lens Oscillations for Optical Applications

David Schipf

A dissertation
submitted in partial fulfillment of the
requirements for the degree of

Doctor of Philosophy

University of Washington

2019

Reading Committee:

Wei-Chih Wang, Chair

Mark Tuttle, Chair

John Kramlich

Program Authorized to Offer Degree:
Mechanical Engineering

University of Washington

Abstract

Electrowetting Liquid Lens Oscillations for Optical Applications

David Schipf

Co-Chairs of the Supervisory Committee:
Affiliate Professor Wei-Chih Wang
Mechanical Engineering

Professor Emeritus Mark Tuttle
Mechanical Engineering

The ability to modulate the phase of a transmitted beam over space and time is valuable in optical systems. Adaptive optics systems, such as retina imaging systems, can require dynamic wavefront correction and shaping of coherent beams. A two liquid cell with dissimilar refractive indices and a user defined meniscus profile can modulate a wavefront with polarization insensitivity. This can be done in transmission, and with cost-effective materials, by controlling the meniscus profile with electrowetting. While the use of a static meniscus profile shape in electrowetting lenses is well documented, the use of oscillations on the meniscus profile has just recently begun to be explored. The superposition of electrowetting liquid lens oscillations can form an arbitrary profile for user defined wavefront correction or beam shaping. If only one electrode around the liquids is used, radially symmetric oscillations are present, while multiple electrodes enables asymmetric oscillation patterns. Models for the dynamics of an electrowetting liquid lens are given and discussed in this thesis. A method for measuring the liquid-liquid meniscus profile over space and time using digital holographic interferometry (DHI) is detailed. Measurements of a commercial electrowetting liquid lens driven from $f_f = 10$–200Hz are presented and analyzed. A frequency response is given, as well as an analysis of the oscillation frequencies and profile spatial spectrum. Non-linear effects that were observed at higher forcing amplitudes are noted. A new application application of an oscillating electrowetting liquid lenses in random phase mask optical image

cryptography is also presented. Through the presentation of experimental, theoretical and numerical work, the usefulness of oscillating electrowetting lenses for optical applications is investigated.

TABLE OF CONTENTS

Page

LIST OF FIGURES

ACKNOWLEDGMENTS

The author wishes to express sincere appreciation to Kurt Samson, Amir Amini, and Bud Homsy for discussions on the modeling of liquid lens oscillations. The author would like to thank his advisor, Wei-Chih Wang, for the opportunity to spend nearly two years in Taiwan conducting research. The author would like to thank the National Security Education Program for one year of funding in Taiwan through the Boren Fellowship for International Studies. Finally, the author would also like to acknowledge the Department of Physics, the Mechanical Engineering Department, the William B. Boeing Department of Aeronautics and Astronautics, the University of Washington Bothell Mechanical Engineering Department, and the Office for the Advancement of Engineering Teaching and Learning for funding by instructor or teaching assistance assignments during his Ph.D. program.

Soli Deo gloria.

DEDICATION

To the memory of Robert George Schipf, and the future of Abraham Robert Schipf

Chapter 1

INTRODUCTION AND MOTIVATION

The manipulation of electromagnetic waves in the optical band is commonly performed by tunable diffraction gratings, tunable mirrors, spatial light modulators (SLMs), and mechanically adjustable mirrors and lens systems [1, 2, 3, 4]. Transmission mode devices work by changing the phase of the beam as it passes through the device, while mirrors change the phase by reflection [1]. Transmission beam steering, beam shaping, and adjustable focusing is desirable in applications with footprint considerations, including consumer electronics [5, 6, 7], optical image encryption [8], and in biomedical imaging [9, 10, 11, 12, 13, 14].

The shaping of optical beams for image improvement is called wavefront correction. Aberrations that change over time need to be dynamically corrected, giving a need for wavefront correction devices that dynamically change their transmission functions [1]. Wavefront correcting devices are used in adaptive optics systems with images that suffer from aberrations due to atmospheric effects, human eye corneas, or defects in mirrors or lenses [1]. Wavefront correction can come from a change in dielectric permittivity, a change in polarization, or a change in optical path length [2, 3, 15].

Wavefront correction is useful for imaging the human retina, and for human eye image compensation. Aberrations introduced from the human cornea, which is unique, need to be compensated for high resolution optical coherence tomography (OCT) imaging of the retina [16, 17, 18]. It has long been a goal to dynamically correct for aberrations seen by the human eye with wavefront correctors [19]. In both of these applications, wavefront correction needs to be tunable, and the reduction of weight, size, and cost of the wavefront correction device is desirable.

Augmented reality head mounted display systems use phase modulating devices and beam steering for the projection of user-defined images. Phase modulating devices can be used to solve vision correction problems in augmented reality systems [20]. Freeform lenses,

which are static wavefront correction devices that in theory could be dynamic, have been used to improve image quality in head-mounted displays [7]. Beam steering waveplates can be used for eye tracking, which is desired for improving user experiences [21]. The industry continues to move toward devices with small footprints, low cost, low mass, and high performance.

Wavefront shaping in the form of tuning paraboloid surfaces is useful for applications in which the focal plane needs to be changed quickly. Tunable focal length lenses have been employed by biomedical researchers [14, 9, 10, 12] and consumer electronic companies [22, 5]. Liquid lenses have been used as variable focal lenses in low-cost, portable OCT systems [9]. For higher speed variation of the focal length of a lens, oscillations were excited on a membrane lens for high-speed photoacoustic microscopy [10]. Tunable focal length lenses have also been proposed for small cameras [22, 5]. Optofluidic lenses with tunable focal length were developed by Phillips for cellular phone cameras in 2004 [5]. The need for lenses with tunable focal length continues to grow, with the goal of faster than ever focal length switching.

In this dissertation, we study a type of transmission beam shaping device that uses a difference in refractive indices between two non-miscible liquids. We investigate the addition of degrees of freedom to liquid beam shaping surfaces, and the improvement of focal length switching speed by using oscillations. A new application in optical image encryption for liquid surface oscillations is also introduced. In this introduction, a background of liquid systems for optical applications is given, followed by a brief discussion of electrowetting liquid lenses. Finally, the relatively new field of oscillations on electrowetting liquid lenses is reviewed.

1.1 Fluids for optical phase modulation

Optofluidic devices offer the advantage of having a continuous surface for manipulating the phase of a beam, and come in many forms. One example of a continuous surface formed by a fluid is a liquid deformable mirror (LDMs). Recently, LDMs have been demonstrated to be a suitable approach for wavefront correction [23, 24, 25, 26, 27, 28], at a fraction of the cost of other deformable mirrors [29, 30]. With an LDM, the continuous phase correcting

surface is in stark contrast to micro-electro-mechanical-system (MEMS) mirrors, which are a collection of discrete surfaces. LDMs inspire similar efforts to use liquid continuous profiles for dynamic transmission mode phase changes.

Tunable transmission optofluidic devices that can change properties for focusing or defocusing beams can be classified by three categories. The first type, shown in Figure 1.1(a), have two liquids of differing refractive indices to change phase by change of optical path length. the second type, shown in Figure 1.1(b), also change phase by path length change, but do so with a solid bending membrane. The third type have a tunable refractive index, as shown in Figure 1.1(c).

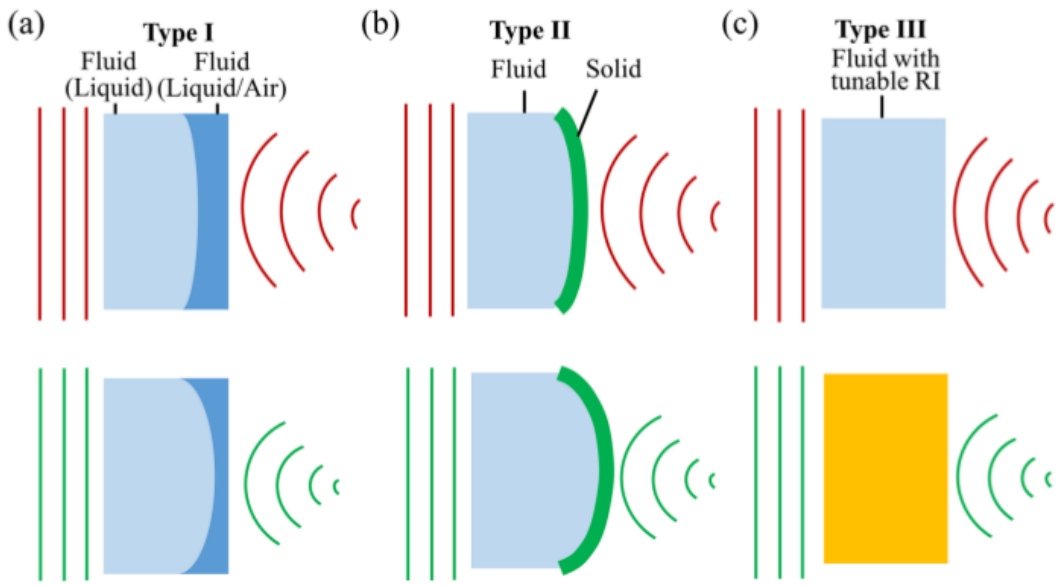

Figure 1.1: The three classifications of tunable fluid lenses. The first type (a) have changing liquid-liquid meniscus. The second type (b) have a membrane over a fluid region. The third type (c) have a tunable refractive index fluid medium. Reprinted with permission from [31], IOPscience.

An example of the third type of tunable transmission lens in Figure 1.1 are acoustic optical lenses. Have been the subject of research for years, the tunable acoustic gradient index (TAG) lens is now available commercially. The TAG lens uses acoustic waves in a fluid to alter the electric permittivity (and therefore the index of refraction), creating a

gradient lens [32, 33, 34]. This lens has a quick response time [34] at time scales of 1 μs and can be used to oscillate the focal length at frequencies > 1kHz [32]. One disadvantage of its use is the wavelength dependence of the phase change, and its high power consumption.

Ferroelectric liquid crystal spatial light modulators (SLMs) are another example of a third type of tunable transmission optofluidic device that can shape a beam with different phase changes at discrete locations in a grid [1]. SLMs also have a quick response time, with the ability to change phase on the order of milliseconds [35]. Commercial transmission liquid crystal SLMs enable a high amount of degrees of freedom, but are expensive and polarization sensitive [36].

An example of the second type is a liquid filled, membrane electrically tunable lens. Commercially available lenses of this type are made by Optotune [37]. These lenses offer reliable focus switching by moving fluid with a deformable membrane [38]. These lenses have been driven at the first resonance frequency for fast focal length oscillation in a microscopy application [10].

One example of the first type of tunable transmission optofluidic device is a 2mm thick fluid lens actuated by a PZT transducer. As shown in Figure 1.2(a) and Figure 1.2(b) The bottom of the ring shape PZT transducer is connected to a thin Polydimethylsiloxane (PDMS) slab. The transducer vibrates in both the transverse (horizontal) and vertical directions (shown in Figure 1.2(c)). The resulting fluid potential is a superposition of the potential from the ring vibration, treating the bottom PDMS slab as a rigid plate, the potential from the bottom plate treating the ring as rigid, and the sloshing mode of the fluid [39].

Another example of the first type is electrowetting lenses. Developed initially in France, electrowetting lenses uses two non-miscible liquids with dissimilar refractive indices for a tunable optical path length change [40, 41]. The liquid-liquid interface is much simpler than a membrane pumping liquid in and out of channels, as is the case for membrane lenses [42], and doesn't involve any movement of the top and bottom windows like the aforementioned PZT lens [39], and is a capacitive element that will consume less power. Electrowetting lenses have been demonstrated to have quick response times on the order of milliseconds and overall effectiveness in shaping optical beams [43, 40, 41, 44, 5, 45]. The focus of

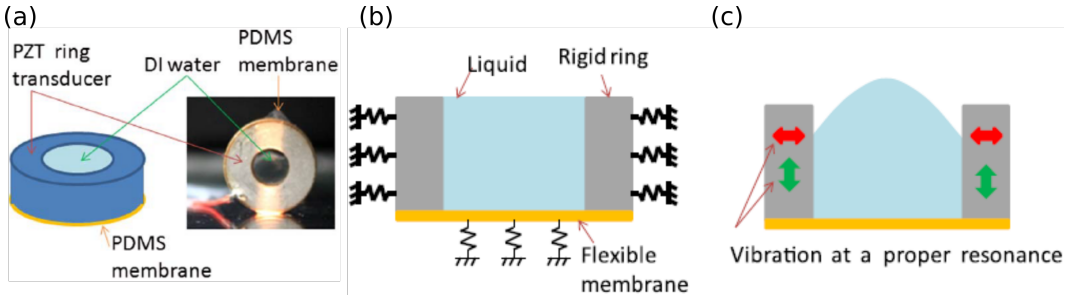

Figure 1.2: Example of a PZT transducer actuated liquid lens with a ring transducer and a PDMS bottom. A photo and diagram of the lens' construction are shown in (a), the mechanical spring diagram is shown in (b), and the resulting liquid lens shape is shown in (c). Modified and reprinted with permission from [39], Optical Society of America (OSA).

this study is on electrowetting lenses because of their potential for simplicity [5], lack of movement [40, 5], low-cost [40], low-power usage [46], and continuous profile [40, 5].

1.2 Electrowetting Lenses

Electrowetting lenses offer fast focal length tuning in a small package. The focal length is tuned by an electric potential change [40, 5, 41, 44], which alters the balance of forces at the contact line between the two liquids and the side-wall, causing the contact line to move [40, 41]. This forces a shift in the meniscus between the two liquids, resulting in a change in radius of curvature, and therefore a change in focal length for a propagating beam. The phase change from this optical path length change is not polarization dependent like liquid crystal spatial light modulators [40]. Commercial electrowetting lenses provide fast switching between stable radius of curvature with low hysteresis [44]. Electrowetting lenses have been fabricated with two different shapes: cylindrical prism and conical frustum. An example of a cylindrical lens, fabricated by researchers at the University of Colorado Boulder, is shown in Figure 1.3.

The fabrication of electrowetting lenses requires several steps, and in some cases requires specialty transparent electrodes. Currently, non-membrane electrowetting lenses are sold exclusively by Corning (previously Varioptic) [47] and are made with a conical frustum shape and opaque side-walls. However, cylindrical electrowetting lenses with transparent side-walls

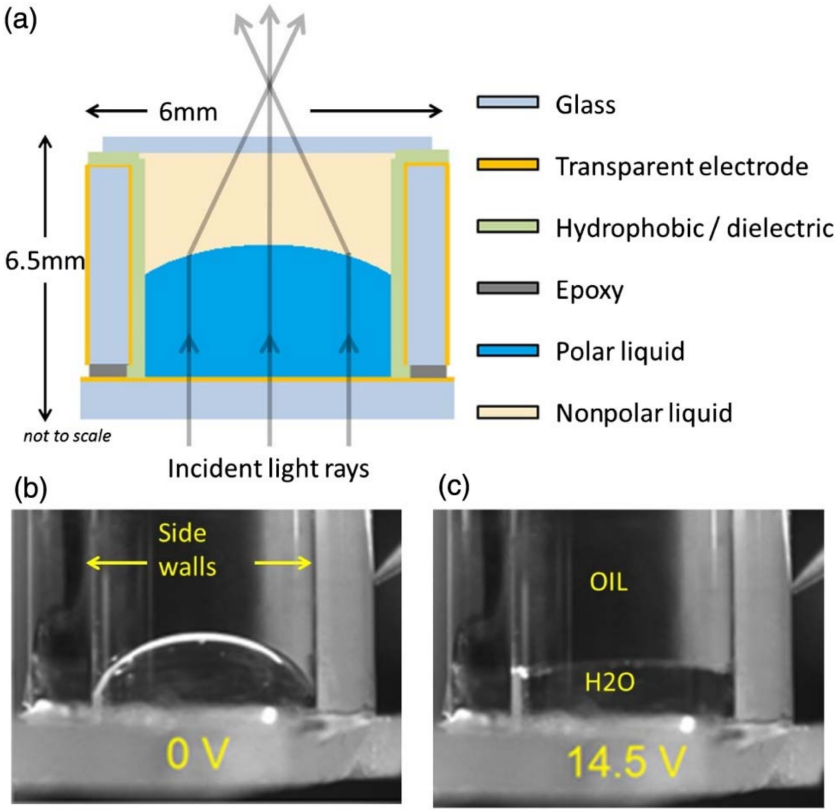

Figure 1.3: Electrowetting lens in a cylindrical prism using two immiscible fluids: one polar and one non-polar. In this case, oil and water were used for the two liquids. (a) Diagram of the cross-section. (b) The fluid lens has a curved meniscus for an applied voltage < 14.5V, and (c) a flat shape with a bias voltage of 14.5V. Reprinted with permission from [46], Optical Society of America (OSA).

for measurement purposes are currently fabricated by the aforementioned researchers at the University of Colorado, Boulder [45, 46, 48]. A diagram of the fabrication process used by this group to produce two-electrode electrowetting liquid lenses is shown in Figure 1.4.

The diagram in Figure 1.4 shows the main fabrication steps for electrowetting lenses 1.4. The first step is cleaning, and application of tape to areas where a conductor is unwanted. The next step is the application of a metal or transparent conductor. In the example shown in Figure 1.4, a transparent conductor Indium-zirconium-oxide (IZO) is used so that the meniscus can be view-able from the side. The third step involves the application of a dielectric layer and a hydrophobic layer. the dielectric layer is the medium through which

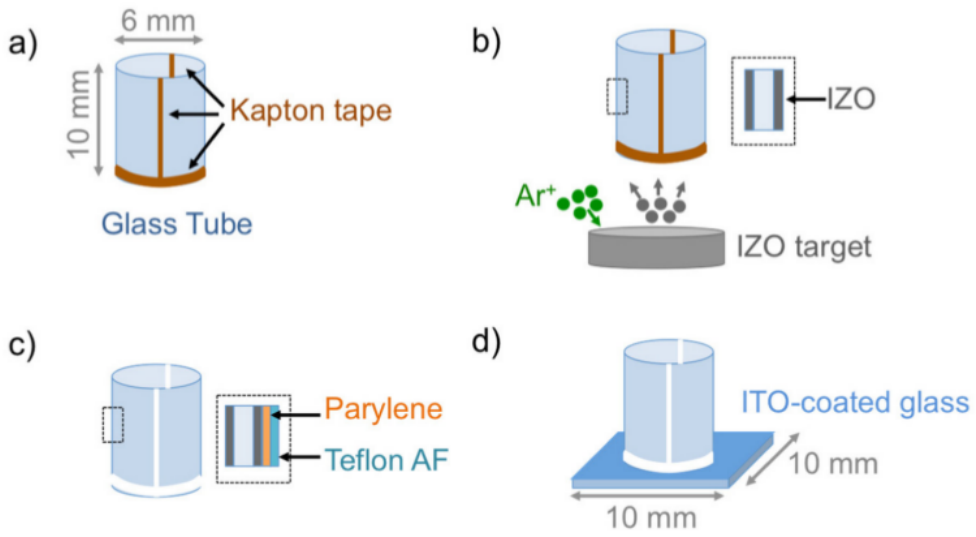

Figure 1.4: The fabrication of a two-electrode cylindrical electrowetting liquid lens. (a) The dimensions of the lens. (b) the deposition of indium-zirconium-oxide (IZO) for the outer electrode. (c) The deposition of two dielectric layers for the inside of the lens. (d) The application of a conductive optical window to transmit current through the polar liquid. Reprinted with permission from [46], Optical Society of America (OSA).

an electric field from the polar liquid to the outer electric is applied. The hydrophobic layer allows for the non-polar liquid to initially be wetting [49], and is necessary for reduction of hysteresis effects [45]. Optical windows can be applied to the top and bottom of liquid lenses to trap the liquids [46, 5].

In addition to focusing, tunable wavefront shaping and modulation is possible using a near static lens shape, but requires more electrodes or multiple lenses. Multiple electrodes around the outside of a lens can be used for asymmetric wavefront correction [50]. Alternatively, multiple lenses positioned in an array with individually controlled electrodes produces a spatially discrete tunable wavefront correction device [13]. With either of these design concepts, degrees of freedom are added at the cost of multiple electrodes and complexity.

1.3 Electrowetting Lens Oscillations

While it is most often desired that tunable fluid optical elements have stable geometries, or geometries oscillating in shape at frequencies too high to affect the application, fluid

systems such as fluid lenses can exhibit surface waves at low amplitudes with spatially varying patterns that oscillate in shape at constant time-frequencies. The mysterious and memorizing beauty of parametrically forced wave patterns has been known since the time of Michael Faraday [51], and are still the subject of study [52, 53, 54, 55, 56, 57]. Parametric driven surface waves have a form, frequencies of oscillation, and amplitude that depend on the geometry of the fluid container, fluid properties, and the method of excitation. Fluid surface waves, such as parametrically driven waves, are inherently rich in user defined information, and contain more degrees of freedom than static shapes.

Though there are many ways to generate fluid surface waves, generation by moving the fluid filled container or by electrowetting are the easiest to reproduce. Surface waves generated by bobbing sources share similarities with parametrically forced surface waves [58, 59]. However, such a fluid system would be difficult to scale down to the meso and micro scales. Oscillations on the meniscus profile of electrowetting liquid lenses are practical, and can be excited easily by the application of a voltage source without movement.

The first studies of oscillations in electrowetting lenses was on the step response of conical frustum [43] and cylindrical shaped liquid lenses [5]. A step response is of interest for lenses that are expected to change focal length and maintain a near-static profile. Therefore, the design goal for focal length switching liquid lenses is to exhibit a step response with minimum overshoot, but with a fast response time.

The standing wave oscillation shapes of a conical frustum Corning lens [47] when forced harmonically were modeled and measured by Strauch et al. in 2017 [60]. The propagation pattern was measured, and the intensity of the center node was used to calculate a first resonance frequency. Measurements for meniscus profiles from voltage pulses was published also by Strauch et al. in [61]. Measurements of the entire liquid meniscus over time, and a frequency response from 23–100Hz, for a Corning lens under harmonic forcing were presented recently in [62]. These three studies show that there is a great promise for practical use of electrowetting lens oscillations for beam shaping and fast focusing.

Applications for liquid lens oscillations have recently been proposed and demonstrated. There exist articles on focal length sweeping using resonant oscillations for biomedical imaging applications [10, 14]. There are also studies of optical phase modulation [60, 61] using

combined oscillations from multiple driving frequencies or pulses and time-dependent image encryption [8]. Combined, multi-mode oscillations provide more degrees of freedom than a stable profile, offering the ability to create a user-defined lens profile. This document focuses on meniscus profile oscillations from one outer electrode, though in future studies oscillations from multiple electrodes could be realized for axis-asymmetric profile shapes.

In this paper, we present an experimental study of electrowetting lens meniscus oscillations. We use digital holographic interferometry (DHI) to measure the meniscus over time and space, and compare measurements to simple models based on the kinematics and geometry of the lens. A goal of this research was to further develop predictive models for oscillation shapes, amplitudes, and frequencies. At the end of the document, we present potential applications for electrowetting lens oscillations, including dynamic focusing, wavefront correction, and image encryption.

Chapter 2

MODELING THE ELECTROWETTING LIQUID LENS

For the sake of understanding and predicting the amplitude and shape of meniscus oscillations on electrowetting lenses, models of the oscillations are presented in this chapter. First, the angle of the contact line between two liquids in an electrowetting lens is modeled using lumped parameters. The equations for the contact angle given a specific voltage is discussed. Second, using a potential flow model, an analytical equation for unforced oscillation displacement between two non-miscible liquids is derived. Third, a simple model for the shape of harmonically forced meniscus oscillations given a specific frequency is discussed. Finally, an alternative model for displacement on a conical frustum shaped lens, which is the most common commercially available lens, is presented.

2.1 The Electrowetting lens contact line

The static shape of a meniscus between two non-miscible liquids is modeled by the Young-Laplace equation, which gives the change in pressure across the meniscus as [49, 63]

$$\begin{aligned} \Delta P &= \gamma_{LL} \nabla \cdot \hat{n} \\ &= \gamma_{LL} \left(\frac{1}{R_1} + \frac{1}{R_2} \right), \end{aligned} \tag{2.1}$$

where γ_{LL} is the surface tension between the two liquids, R_1 and R_2 are the radii of curvature of the surface, and $\hat{n}$ is the surface normal directional vector. This equation relates local pressure to the curvature of the meniscus profile, and is valid for an undisturbed profile.

When considering a balance of the capillary forces acting on the contact line, where the two liquids and the solid boundary meet, the natural contact angle of the polar liquid θ_E can be expressed in terms of surface tensions as [49]

$$\cos \theta_E = \frac{\gamma_{L1} - \gamma_{L2}}{\gamma_{LL}}, \tag{2.2}$$

where γ_{L1} is the surface tension between the first liquid (non-polar) and the solid boundary and γ_{L2} is the surface tension between the second liquid (polar) and the solid boundary. Most liquid lenses have a hydrophobic inner surface, so $\theta_E > \pi/2$. This is the case for the liquid systems used and presented in this document.

In electrowetting lenses, an electric potential change between the polar liquid and an electrode around the outside of the lens changes the contact angle. The arrangement of the electrodes in a simple cylindrical electrowetting lens can be seen in Figure 2.1. The simplest arrangement is with an axis-symmetric outer electrode, which allows us to view the problem in two dimensions with rotational symmetry.

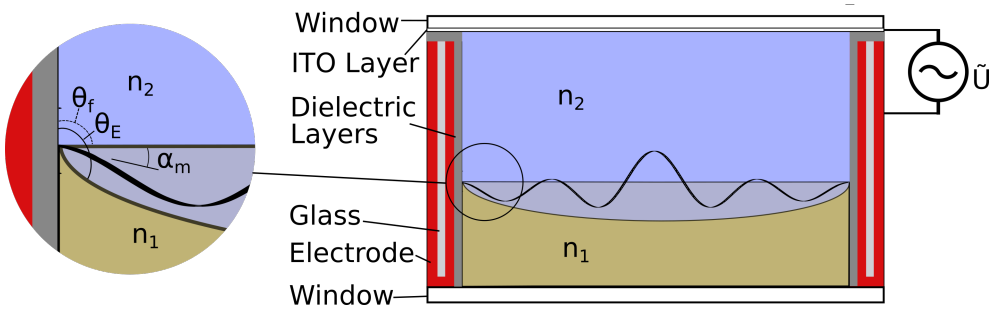

Figure 2.1: The cross-section of a cylindrical electrowetting lens. The first liquid (brown) is non-polar and has a refractive index n_1, while the second liquid (blue) is polar and has a refractive index n_2. The electric potential $\tilde{U} = U_B + U_0 cos(2\pi f_f t)$ is used to force a flat interface with a DC offset ($U_B = 48$V) and oscillations with a harmonic function.

The liquid lens can be modeled as a two-port electro-mechanical element. On one side of the element, there is an electric potential input V_{in} and a charge displacement q. On the other side of the element, you have a variable height a of one of the liquids, with an electric force f_e as the displacement [64]. A diagram of this two-port element is shown in Figure 2.2.

We can describe the energy of the element as

$$We(Q) = \frac{Q^2}{2C}, \tag{2.3}$$

or the co-energy as

$$We^*(U) = \frac{CU^2}{2}, \tag{2.4}$$

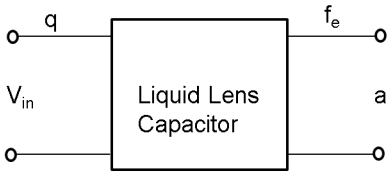

Figure 2.2: An electrowetting liquid lens modeled as a two-port element.

where U is the applied voltage and Q is the electrical charge. Using a conservation of energy analysis for the purpose of finding the electrical force on the contact line, we find [64]

$$dWe = Vdq - 2\pi a f_e da, \tag{2.5}$$

or, for the co-energy we have [64]

$$dWe^* = qdV - 2\pi a f_e da. \tag{2.6}$$

This gives us an electrical force at the contact line per unit length of

$$f_e = \frac{1}{2\pi a}\frac{\partial We^*}{\partial a} = \frac{U^2}{4\pi a}\frac{dC}{da}. \tag{2.7}$$

In most cases the capacitance C can be simply expressed as [64]

$$C = \frac{\epsilon_0 \epsilon_r \pi a^2}{d}; \tag{2.8}$$

then the electrical force is

$$f_e = \frac{\epsilon_0 \epsilon_r U^2}{2d}. \tag{2.9}$$

The force due to surface tension comes from a balance of forces, and can be found to be [49]

$$f_\gamma = -\gamma_{LL} cos(\theta_f) + \gamma_{L1} - \gamma_{L2} \tag{2.10}$$

where $L1$ is the first liquid, $L2$ is the second liquid, the contact angle measured from the polar liquid side is θ_f, and γ is surface tension. The equilibrium contact angle (with the absence of an electric field) θ_E is found by setting $f_\gamma = 0$. This equilibrium contact angle θ_E is measurable in most systems, giving a ratio of surface tension terms. When balancing

forces f_γ and f_e acting on the contact line per unit length, and then diving both sides by γ_{LL}, the electric force dependent contact angle as a function of the electric force is [65, 40]

$$\begin{aligned} cos(\theta_f) &= \frac{f_e}{\gamma_{LL}} + cos(\theta_E) \\ &= \frac{\epsilon U^2}{2d\gamma_{LL}} + cos(\theta_E). \end{aligned} \tag{2.11}$$

Equation 2.11 is commonly referred to as the Young-Lippmann equation, and is the most common equation used to model liquid lenses. The forcing term is made of the applied direct current (DC) or alternating current (AC) voltage amplitude U and the dielectric permittivity ϵ and thickness d of the side-wall. This equation can be used for alternating current (AC) forcing if the forcing frequency f_f is larger than the natural frequency of the lens, and less than the critical frequency, as defined in [66]. The critical frequency depends on the physical properties of the liquids, as well as the geometry of the electrowetting system [66], and is reported to vary between 10–100 kHz for polar liquid drops surrounded by air [66].

The Young-Lippmann equation only matches experiments within a threshold and saturation voltage range [66, 65]. The liquid minimizes surface energy, and forms a paraboloid shape in a static situation. Eq. (2.11) can therefore predict the focal length of the liquid lens at any given voltage within this range.

2.2 Oscillations on a cylindrical Liquid Lens Profile

For the modeling of the dynamic behavior of liquid lenses, the Young-Lippmann equation must be modified using a term that comes from molecular kinetic theory (MKT). An additional term in the Young-Lippmann equation is needed to accurately model the movement of molecules near the contact line that add a friction force opposing movement [49, 67, 68]. There has been relative success in modeling the dynamic behavior of electrowetting drops on dielectric layers using an MKT and electro-mechanical hybrid model and then simulating the flow with finite element analysis [68]. The modified equation for the contact angle given a voltage amplitude U is

$$cos(\theta_f) = \frac{f_e}{\gamma_{LL}} + cos(\theta_E) - \frac{f_k}{\gamma_{LL}} \tag{2.12}$$

where f_k is the friction force at the triple contact line, given as [68, 69]

$$f_k = \lambda_f u_{cl} + c_p \left[\text{sign}(u_{cl}) - \frac{2}{\pi} \tan^{-1} \left(\frac{\lambda_f u_{cl} \pi}{2 c_p} \right) \right] \tag{2.13}$$

In the above equation, u_{cl} is the velocity of the contact line. The second two terms above are from a pinning force that is at a maximum when the contact line is about to move. The coefficient c_p is from the contact angle pinning that gives rise to hysteresis in the contact angle. The friction coefficient λ_f can be found by [68, 69]

$$\lambda_f = \frac{k_B T_p}{k^0 l_a^3} \tag{2.14}$$

where k^0 is the equilibrium frequency of the random molecular displacement, T_p is the absolute temperature, and l_a is the average length of each molecular displacement. From this equation, it can be seen that the calculation of $cos(\theta_f)$ depends on the movement of the liquids near the contact line, while the unmodified Young-Lippmann equation does not. Parameters λ_f and c_p in 2.13 need to be found empirically [68, 49, 69].

2.2.1 Unforced oscillations

To predict surface amplitudes and shapes based on a voltage and the contact line behaviour, a fluid mechanics study is necessary. Meniscus waves in an electrowetting lens emerge from forces at the contact line, and are then influenced by the hydrodynamics of the two liquids [59, 58, 69]. For a simple first analysis, incompressible, irrotational flow is assumed. The coordinate system shown in Figure 2.3 is used.

The velocity potential for each liquid Φ^j, $j = 1, 2$ must satisfy the three dimensional Laplace equation. In the cylindrical coordinate system, this is [70, 58]

$$\nabla^2 \Phi^j = \frac{1}{r} \frac{\partial}{\partial r} \left(r \frac{\partial \Phi^j}{\partial r} \right) + \frac{1}{r^2} \frac{\partial^2 \Phi^j}{\partial \theta^2} + \frac{\partial^2 \Phi^j}{\partial z^2} = 0. \tag{2.15}$$

The solution for Φ^1 and Φ^2 must also satisfy the following boundary conditions [58]:

$$\left. \frac{\partial \Phi^1}{\partial r} \right|_{r=R} = 0, \tag{2.16}$$

$$\left. \frac{\partial \Phi^1}{\partial z} \right|_{z=-h_1} = 0, \tag{2.17}$$

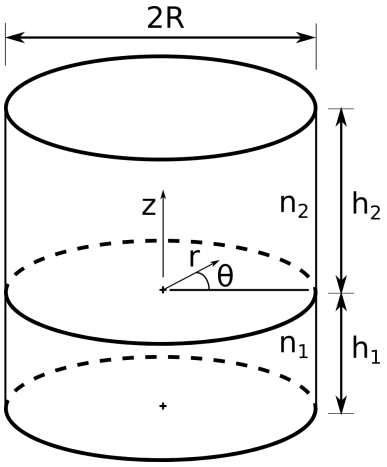

Figure 2.3: A diagram of the cylindrical geometry used for modeling the oscillations on the meniscus profile forced by electrowetting.

$$\frac{\partial \Phi^2}{\partial r}\Big|_{r=R} = 0, \tag{2.18}$$

$$\frac{\partial \Phi^2}{\partial z}\Big|_{z=h_2} = 0, \tag{2.19}$$

$$\frac{\partial \Phi^1}{\partial n}\Big|_{z=0} = \frac{\partial \Phi^2}{\partial n}\Big|_{z=0}, \tag{2.20}$$

$$\frac{\partial \Phi^1}{\partial n}\Big|_{z=0} = -\frac{\partial \eta}{\partial t}. \tag{2.21}$$

This gives the following axis-symmetric solutions [58]:

$$\Phi^1 = \sum_{n=1}^{\infty} A_n J_0(k_n r) \frac{cosh[k_n(h_1+z)]}{cosh(k_n h_1)}, \tag{2.22}$$

$$\Phi^2 = \sum_{n=1}^{\infty} A_n \frac{\tanh(k_n h_1)}{\tanh(k_n h_2)} J_0(k_n r) \frac{cosh[k_n(z-h_2)]}{cosh(k_n h_2)}, \tag{2.23}$$

with $k_n = j_{1,n}/R$, where $j_{1,n}$ are the roots of the Bessel function of the first kind, and first degree ($J_1(j_{1,n}) = 0$ for any integer n). The height or thickness of the two liquids is h_1 and h_2.

At the meniscus ($z = 0$), the normal stress balance is [63, 69]

$$[\hat{n} \cdot (\hat{n} \cdot \sigma_1)] - [\hat{n} \cdot (\hat{n} \cdot \sigma_2)] = \gamma_{LL} \nabla \cdot \hat{n}, \tag{2.24}$$

where the hydrodynamic stress tensor $\sigma = -p\boldsymbol{I} + \mu(\nabla u + \nabla u^T)$, with $\boldsymbol{I}$ as the isotropic tensor, where p is pressure, u is velocity, and μ is kinematic viscosity. The normal directional vector $\hat{n}$ is along the z axis, as labeled in Figure 2.3, and the tangential directional vector $\hat{t}$ is along the radial direction. The tangential stress balance is [63, 69]

$$\left[\hat{t}\cdot(\hat{t}\cdot\sigma_1)\right] - \left[\hat{t}\cdot(\hat{t}\cdot\sigma_2)\right] = \gamma_{LL}\nabla\cdot\hat{t}, \tag{2.25}$$

It has been shown in [63] and [69] for free surface liquid waves that we can use the normal stress balance (Equation 2.24) for oscillations with amplitudes smaller than the wavelength. In free surface oscillating drop studies, the tangential stress component is set to zero [63, 69]. This is justified by a scale argument in [49]. The displacement and velocity potential must then satisfy the normal stress balance at the meniscus ($z = 0$), which can be written as [69]

$$\begin{aligned}
[\hat{n}\cdot(\hat{n}\cdot\sigma_1)] - [\hat{n}\cdot(\hat{n}\cdot\sigma_2)] &= -p_2 + p_1 \\
&= -\rho_2 g\eta_2 - \rho_2\frac{\partial\Phi}{\partial t} + \rho_1 g\eta_1 - \rho_1\frac{\partial\Phi^1}{\partial t} \\
&= \rho\frac{\partial\Phi^1}{\partial t} - \rho\frac{\partial\Phi^2}{\partial t},
\end{aligned} \tag{2.26}$$

if we assume $\rho_1 \approx \rho_2 \equiv \rho$ and neglect viscous terms.

When using equation 2.24, we can take $\gamma_{LL}\nabla\cdot\hat{n} \approx \gamma_{LL}\nabla^2\eta$ for small oscillations [63, 49], where

$$\nabla^2 f(r,\theta) = \frac{1}{r}\frac{\partial}{\partial r}\left(r\frac{\partial f}{\partial r}\right) + \frac{1}{r^2}\frac{\partial^2 f}{\partial\theta^2} \tag{2.27}$$

in cylindrical coordinates for any function $f(r,\theta)$. This gives an expression relating displacement η, Φ^2 and Φ^1 at the meniscus ($z = 0$) of

$$\rho\frac{\partial\Phi^1}{\partial t} - \rho\frac{\partial\Phi^2}{\partial t} = \gamma_{LL}\nabla^2\eta. \tag{2.28}$$

With the z direction as the normal n direction, we can separate the velocity potential of each fluid Φ^j, $j = 1, 2$ into a function of time and space along the plane of the meniscus, and a function of z as [58, 71, 72]

$$\Phi_n^j = \tilde{\phi}(r,t)_n^j \cdot G(z)_n^j. \tag{2.29}$$

This modifies Equations 2.20 and 2.21 into

$$\frac{\partial G_n^1}{\partial z}\tilde{\phi}_n^1 = \frac{\partial G_n^2}{\partial z}\tilde{\phi}_n^2, \tag{2.30}$$

$$\frac{\partial G_n^1}{\partial z}\tilde{\phi}^1 = \frac{\partial \eta}{\partial t}. \tag{2.31}$$

After taking the partial time derivative of both sides of 2.28, and after using 2.30 and 2.31, the following equation for the nth mode is found:

$$\frac{\partial^2 \tilde{\phi}_n^1}{\partial t^2} - C_n^2 \nabla^2 \tilde{\phi}_n^1 = 0. \tag{2.32}$$

The mode dependent constant is

$$C_n^2 = \frac{\gamma_{LL}}{\rho} \frac{k_n \tanh(k_n h_1)}{1 - \frac{\tanh(k_n h_1)}{\tanh(k_n h_2)}}. \tag{2.33}$$

Equation 2.32 is the wave equation in cylindrical coordinates. This is consistent with the findings in [63] for a spherical drop, the derivation in [72], and the intuition and experimental results presented in [60] and [61].

We can solve for an analytic expression of the velocity potential by separation of variables into

$$\tilde{\phi}(r,t)_n^j = \phi(r)_n T(t)_n. \tag{2.34}$$

This gives two ordinary differential equations, one in space and one in time. The two equations can be equated to a mode dependent constant ω_n^2 as

$$\frac{\ddot{T}}{T} = \frac{C_n^2 \nabla^2 \phi}{\phi} = -\omega_n^2. \tag{2.35}$$

We first consider the spatial differential equation, which has the form of a Helmholtz equation, given as

$$\nabla^2 \phi_n + k_n^2 \phi_n = 0, \tag{2.36}$$

with

$$k_n^2 = \frac{\omega_n^2}{C_n^2}. \tag{2.37}$$

The axis-symmetric solution to Equation 2.36 is consistent with Equation 2.22, with the eigenvalues $k_n = j_{1,n}/R$.

The time differential equation can expressed in the classic harmonic oscillator form of

$$\ddot{T}_n + \omega_n^2 T = 0, \tag{2.38}$$

which gives the solution

$$T_n = L_n e^{-i\omega_n t}, \tag{2.39}$$

for some constant L_n.

The equation for the natural frequency ω_n can be found from the relation $\omega_n^2 = k_n^2 C_n^2$, which gives

$$\omega_n^2 = \frac{\gamma_{LL}}{\rho} \frac{k_n^3 \tanh(k_n h_1) \tanh(k_n h_2)}{\tanh(k_n h_1) + \tanh(k_n h_2)}. \tag{2.40}$$

This is similar to the natural frequencies found in [71] for a rectangular container filled with two liquids. The approach of separating variables to get a Helmholtz equation in variables across the meniscus plane and a harmonic oscillator equation in time was document for a more general two liquid case in [72].

When considering Eq. 2.21, a common approach is to assume a complex solution for Φ that gives a real solution for displacement. The constant in Eq. 2.39 can be altered to give $T_n = L_n(i\omega_n)e^{-i\omega t}$. This gives a solution for the displacement of

$$\eta(r,t) = \sum_{n=1}^{\infty} A_n k_n \tanh(k_n h_1) J_0(k_n r) e^{-i\omega_n t}, \tag{2.41}$$

where the mode dependent constant A_n depends on the initial conditions.

In order to understand how the natural frequency ω_n depends on the geometry of the liquid system, we define a non-dimensional natural frequency of

$$\bar{\omega}_n \equiv \omega_n \left(\frac{\rho R^3}{\gamma_L L} \right). \tag{2.42}$$

We define a characteristic length for the first liquid $L_{1,n}$, and a characteristic length for the second liquid $L_{2,n}$ as

$$L_{1,n} \equiv h_1/R; \tag{2.43}$$

$$L_{2,n} \equiv h_2/R. \tag{2.44}$$

Figure 2.4(a) shows a plot for the first non-dimensional natural frequency using different characteristic lengths L_1 and L_2. There are two liquid lenses that are mentioned and used in this thesis. The first, called the Arctic 58NO [47], has an aperture of 5.8mm, and has a conical frustum shape, similar to the one shown later in this chapter in Figure 2.5. The second, called Arctic 39NO [47], has an aperture of 3.9mm, and also has a conical frustum shape. The geometry of the Arctic 58NO is discussed later in Chapter 3. Treating these lenses as if they have cylindrical geometries, the ratio of the nth natural frequency to the first natural frequency for the 58NO and the 39NO is plotted in Figure 2.4(a).

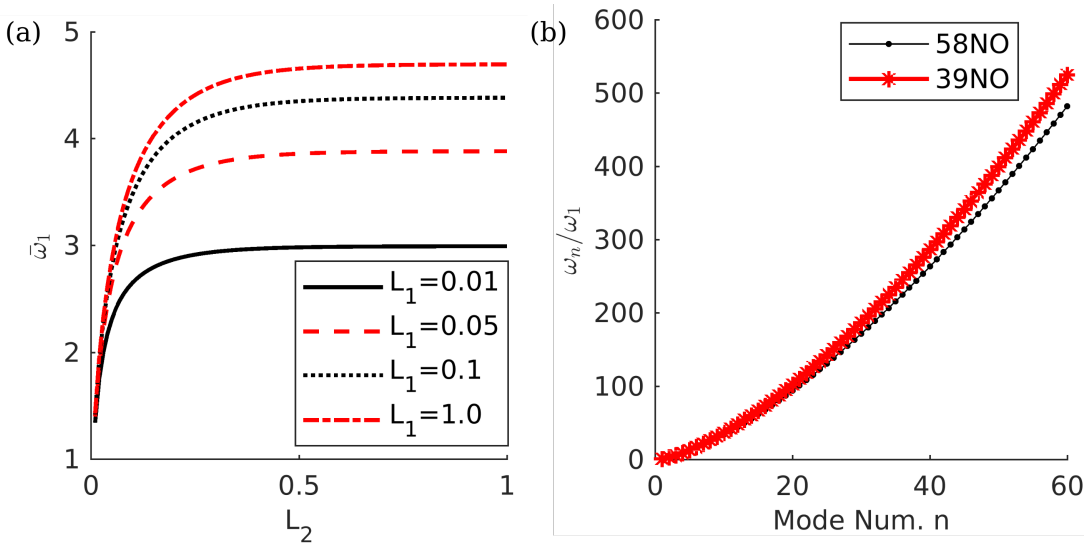

Figure 2.4: (a) The first non-dimensional natural frequency $\bar{\omega}_1$ for different characteristic lengths $L1$ and $L2$ and (b) The ratio of the nth natural frequency to the first for Corning Arctic 58NO and Arctic 39NO [47] geometries.

From Figure 2.4(a), we can see that the natural frequency ω_n increases exponentially with the mode number n. A slight change in geometry between the two lenses gives similar natural frequencies for the lower mode numbers $n < 20$, but the natural frequencies for larger mode numbers diverge.

2.2.2 Forced oscillations

For the case of forced oscillations, a point force can be placed at the boundary. We can use equations Equations 2.15–2.23, but need to modify Equation 2.26, the boundary condition at the meniscus. We take the approach used in [69] for an analytical solution to electrowetting hemispherical drop oscillations surrounded by air. In [69] a point force $W(t)$ is placed at the contact line to account for electrical and surface tension forces. This voltage dependent wetting force $W(t)$ is multiplied by a Dirac delta function to ensure that it disappears elsewhere on the meniscus. It is assumed that the deformation from bulk flows is much less than the deformation due to the wetting tension. The normal stress with this additional wetting force term is

$$-p_2 + p_1 - 2\mu_1 \frac{\partial^2 \Phi^1}{\partial z} + 2\mu_2 \frac{\partial^2 \Phi^2}{\partial z} + \frac{2}{R} W(t)\delta(r - R) = \gamma_{LL} \nabla^2 \xi. \tag{2.45}$$

The solution to the above Equation 2.45 requires a full solution to the relevant fluid dynamics equations without neglecting viscous effects. A solution is currently being developed by the author for a cylindrical two liquid electrowetting lens, but is out of the scope of this document.

In the case of excitation with a harmonic voltage, the displacement can be modeled with standing waves at a dominant mode [61, 60]. An electric potential of $\tilde{U} = U_B + U_0 \cos(2\pi f_f t)$ can excite harmonic displacements about a flat profile. This causes standing waves oscillating up and down at the driving frequency f_f. The displacement for a cylindrical lens is [61, 60]

$$\eta(r, t) = A_c \cos(2\pi f_f t) J_0 \left(\frac{2\pi f_f r}{c} \right), \tag{2.46}$$

where c is the wave speed on the meniscus, and the amplitude is a function of frequency and voltage amplitude $A_c = f(f_f, U_0)$. This model has been compared with experimental measurements of the meniscus profile of conical frustum shaped liquid lenses in [61], [60], and [62] with tuning of A_c to match the amplitudes. It has been found that this model matches measurements for a conical frustum lens only for small amplitude $U_0 < 2.0$V and small frequency $f_f < 100$Hz forcing [62]. In other words, residuals from a comparison of this model with measurements grow as frequency f_f and amplitude U_0 become larger.

2.3 Oscillations on a Conical Frustum Liquid Lens Profile

Commercially available electrowetting lenses have conical frustum shape. This design is used to extend the range of radius of curvature within the threshold and saturation limits. A diagram of the commercially available lens used for results presented in this document is given in Figure 2.5.

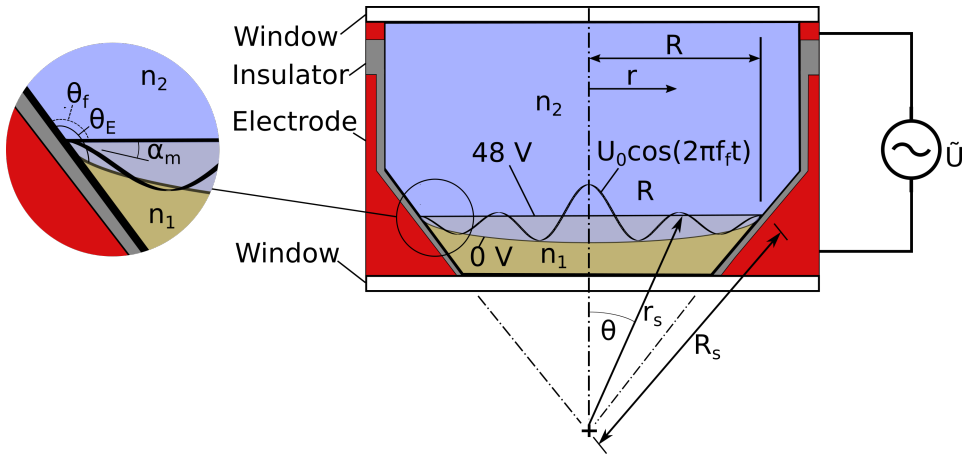

Figure 2.5: The cross-section of a conical frustum electrowetting lens. The first liquid (brown) is non-polar and has a refractive index n_1, while the second liquid (blue) is polar and has a refractive index n_2. The electric potential $\tilde{U} = U_B + U_0 cos(2\pi f_f t)$ is used to force a flat interface with a DC offset ($U_B = 48$V) and oscillations with a harmonic function.

The velocity potential must satisfy the Laplace equation. In the spherical coordinate system, this is [70]

$$\nabla^2\Phi = \frac{1}{r^2}\frac{\partial}{\partial r}\left(r^2\frac{\partial\Phi}{\partial r}\right) + \frac{1}{r^2\sin\theta}\frac{\partial}{\partial\theta}\left(\sin\theta\frac{\partial\Phi}{\partial\theta}\right) + \frac{1}{r^2\sin^2\theta}\frac{\partial^2\Phi}{\partial\varphi^2} = 0. \tag{2.47}$$

We expect a time-dependent solution $\Phi = e^{-i\omega t}\phi(r,\theta,\varphi)$, where $\Delta\phi = 0$. The solution for Φ must satisfy the following boundary conditions

$$\left.\frac{\partial\Phi}{\partial\theta}\right|_{\theta=\alpha_s} = 0, \tag{2.48}$$

$$\left.\frac{\partial\Phi}{\partial r}\right|_{r=R_b} = 0. \tag{2.49}$$

where α_s is the angle made from the center axis along the side-wall of the lens. For a conical frustum container with a meniscus and bottom surface normal in the radial direction, it has been found that [73]

$$\Phi^1 = e^{-i\omega t}\sum_{n=1}^{\infty} A_n \left[\left(\frac{r_s}{R_s}\right)^{\lambda_n} + \frac{\lambda_n k_s^{2\lambda_n+1}}{\lambda_n+1}\left(\frac{r_s}{R_s}\right)^{-\lambda_n-1}\right] P_{\lambda_n}(\cos\theta), \tag{2.50}$$

where $k = R_s/R_b$, and k_n are the eigenvalues that satisfy the boundary condition Eq. (2.48). For $h_1 \ll R_s$, we can approximate $k_s \approx 1$. Note that Equation 2.50 is similar to the solution for the sloshing dynamics of a cone volume of liquid in [58], with the important difference of the term $(r_s/R_s)^{-k_n-1}$. When solving for spherical drops, as in [63], or full cones as in [58], this term needs to be discarded from the solution due to $\phi \to \infty$ as $r \to 0$. Equation 2.50 is an approximate solution if the meniscus is flat, making use of an assumption that the normal direction of the meniscus $\hat{n} \approx \hat{r}$.

This velocity potential must solve the boundary conditions, which are

$$\frac{\partial \Phi^1}{\partial r}\Big|_{r=R_b} = 0, \tag{2.51}$$

$$\frac{\partial \Phi^1}{\partial \theta_s}\Big|_{\theta_s=\alpha_s} = 0, \tag{2.52}$$

$$\frac{\partial \Phi^1}{\partial r}\Big|_{z=0} = \frac{\partial \eta}{\partial t}. \tag{2.53}$$

The boundary condition in Equation 2.52 gives solutions for λ_n, which are only integers for certain values of α_s. Therefore, the velocity potential is a summation of fractional Legendre polynomials, which is often written as hypergeometric functions [74]. The displacement, from solving Equation 2.53, is

$$\eta(r,t) = e^{-i\omega t}\frac{A_n\lambda_n}{R_s}\left[\left(\frac{r_s}{R_s}\right)^{\lambda_n-1} - \left(\frac{r_s}{R_s}\right)^{-\lambda_n-2}\right] P_{\lambda_n}(\cos\theta) \tag{2.54}$$

It was found that the Legendre function $P_{\lambda_n}(\cos(\theta_s)) \approx J_0(k_n r)$, for $k_n = j_{1,n}/R$, and $\lambda_n \approx 1.8635k_n + 0.29683$. The linear fit used to compare λ_n to k_n is shown in Figure 2.6(b). The fit was found when the amplitude of the two models, and λ_n, were tuned until the profiles matched. An example of the Legendre function term $P_{\lambda_n}(\cos\theta)$ plotted against the

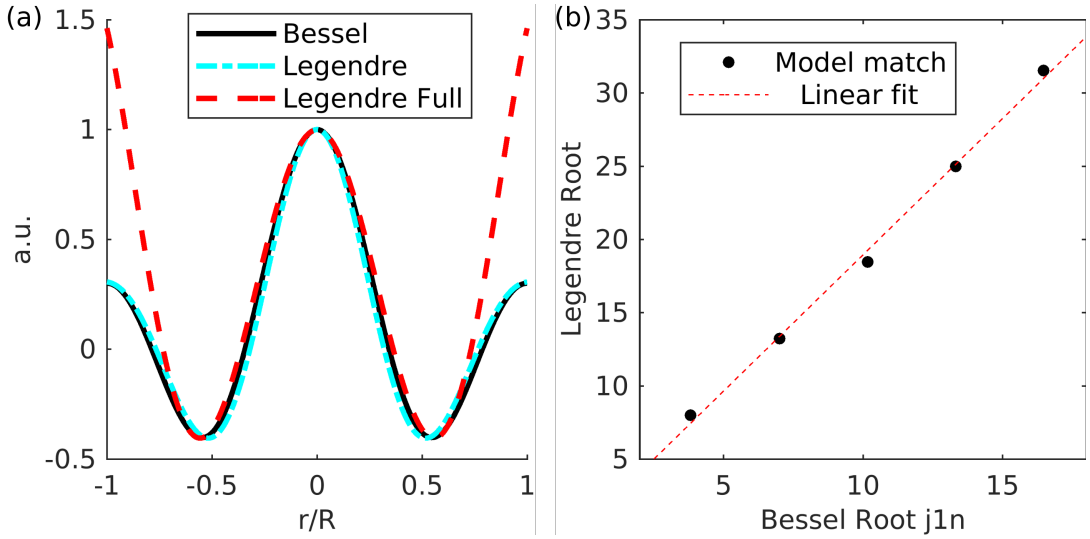

Figure 2.6: (a) The cross-section of displacement using the Legendre function model (Equation 2.54) for a conical lens and the Bessel function model (Equation 2.41) for a cylindrical lens when $k_n = j_{1,2}/R$ and $\lambda_n \approx 1.8635 * k_n + 0.29683$. (b) Linear fit of eigenfunctions from the two models when they were tuned to match.

Bessel function solution for η and the Legendre function solution for η is given in Figure 2.6(a).

The solution for η in cylindrical coordinates (Equation 2.46) and in spherical coordinates (Equation 2.54) was compared for the first four modes of the Bessel function model ($k = j_{1,n}/R$ for $n = \{1, 2, 3, 4\}$. Figure 2.7 shows this comparison plotted across the cylindrical coordinate system radial distance from the center axis divided by the radius of the meniscus (r/R).

From Figure 2.7 it can be seen that near the center axis $r = 0$, the two models produce the same shapes. However, as the distance r increases, the variation from the mean displacement with the Legendre function model becomes greater and diverges significantly from the Bessel function model. It is likely that a more accurate model will predict displacements somewhere between these two models. To find a more accurate model, Equation 2.45 must be solved in either spherical or cylindrical coordinates without the inviscid flow assumption.

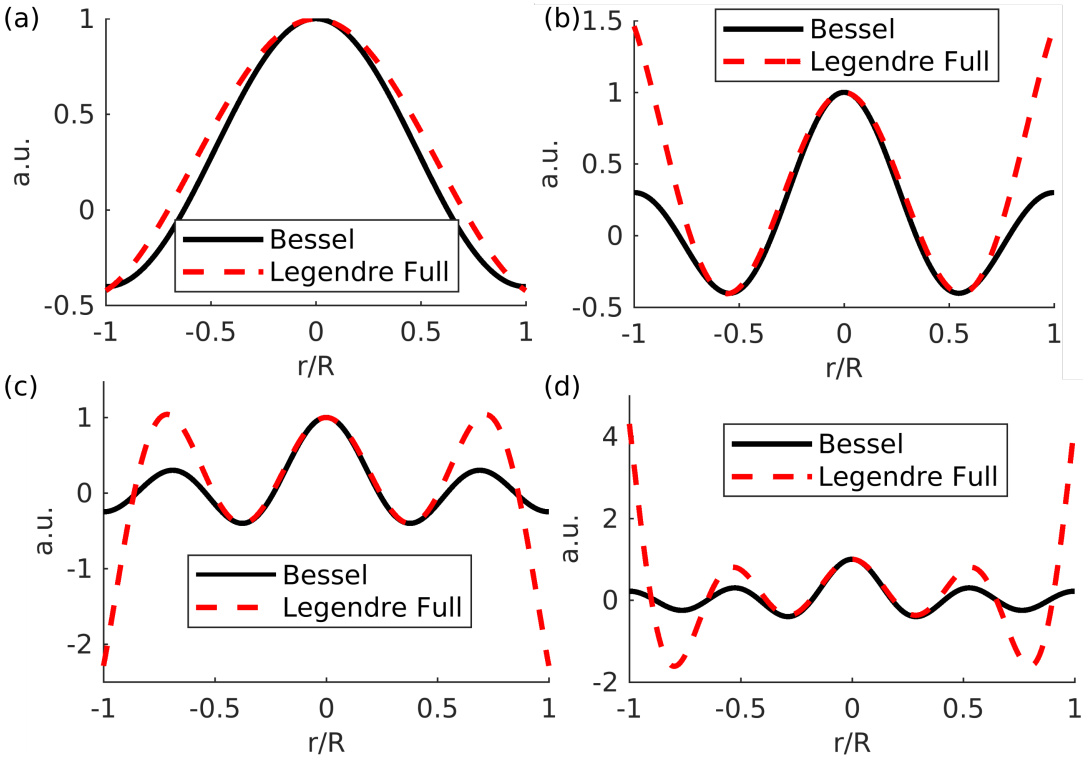

Figure 2.7: The cross-section of displacement using the Legendre function model (Equation 2.54) for a conical lens and the Bessel function model (Equation 2.46) for a cylindrical lens.

Chapter 3

DRIVING THE ELECTROWETTING LIQUID LENS

This chapter discusses the electrical characteristics of the commercial electrowetting lens that was used for oscillation experiments. The commercial liquid lens specifications are first introduced. Then, the driving circuit used for forcing the meniscus profile is presented. Finally, the peculiar charging and discharging of the lens, and the suspected physical mechanisms, are discussed.

3.1 Arctic 58NO Corning Electrowetting lens

For the experiments presented in this document, the commercial electrowetting liquid lens Arctic 58NO, made by Variopic (now Corning) was used [47]. This lens has a similar design to the Arctic 39NO lens, but with an aperture size 2.1x larger. The fluid properties are proprietary, but the geometry and refractive indices are provided by company documentation.

In a summary of lens performance, the company documentation gives an absolution transmission accuracy of 0.07%, a decentering of the polar/non-polar liquid interface of $< 700\mu m$, and a decentering of the lens in the sample holder of $< 600\mu m$. The wavefront error was measured to be as low as 20nm in ideal conditions. Variation in performance from ambient temperature swings is negligible for ordinary room temperatures. The response time is reported to be less than 1ms. The maximum hysteresis is reported to be 5 diopters at around 43V amplitude forcing [47].

The liquid lens has an aperture of 5.8mm, and a conical frustum shape, similar to the conical lens diagram shown in Figure 2.5. The lens requires housing for mounting convenience, which can either be plastic or metal. The lens comes with flexible electrical wires to connect to the voltage source. A picture of the liquid lens beside a ruler is given below in Figure 3.1. As shown in the figure, the lens is quite compact, with a thickness of only a few millimeters.

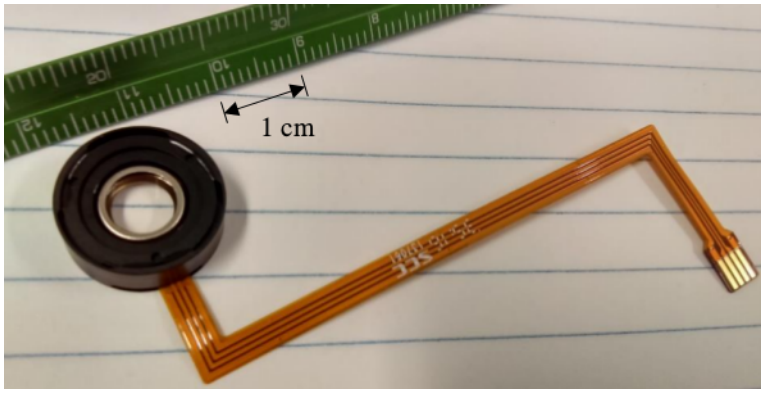

Figure 3.1: photo of one of the Arctic 58NO fluid lenses purchase from Varioptic SA (now Corning [47]).

The flexible wiring has four leads. The two outer leads are for connecting to the ground, while the two inside leads should be connected to the voltage source. The company recommends the lens to be driven by a bi-polar square wave, and so the polarity of the two inside leads is interchangeable.

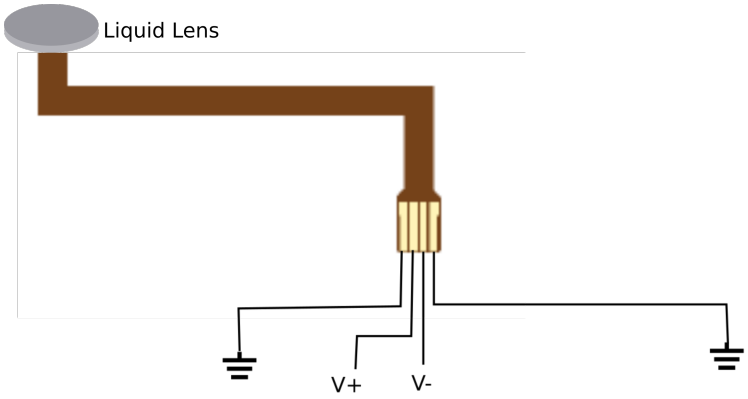

Figure 3.2: Wiring of the Arctic 58NO fluid lenses purchase from Varioptic SA (now Corning [47]).

The lens should be driven by a bipolar square wave instead of a direct current (DC) voltage for safety and performance considerations. It has long been known that electrowetting drops exhibit less hysteresis when driven by an alternating current (AC) voltage instead of a

DC voltage [66]. It has also been found that contact angle saturation occurs at a smaller angle, and therefore at a larger voltage, with AC forcing than with DC forcing. This gives the allowance for a larger radius of curvature range, and therefore a large optical power range. It has been proposed that there is less ion absorption during AC forcing than with DC forcing, which may allow for the lens to be used for more cycles before breaking completely down [66]. In the author's experience, if the maximum voltage of 60V is exceeded several times, multiple drops of the non-polar liquid are formed and the lens becomes unusable.

The geometry of the liquid lens was given by company documentation [47]. The lens follows the following equation for radius of curvature [47]

$$\frac{1}{R_s} = -(0.00006864V_{in}^2 + 0.002633V_{in} - 0.1955) for (V_{in} > 21) \tag{3.1}$$

$$\frac{1}{R_s} = 0.108V_{in} for (V_{in} \leq 21) \tag{3.2}$$

The inverse of the radius of curvature follows a polynomial function when the root mean square (RMS) voltage $V_{in} > 21$, and is linear with V_{in} when $V_{in} \leq 21$. The values $1/R_s$ is at a minimum when $V_{in} \approx 37.531$ V. this can be seen in Figure 3.3 below, where the radius of curvature is plotted vs. input voltage V_{in}. the input voltage V_{in} is considered to be the RMS voltage.

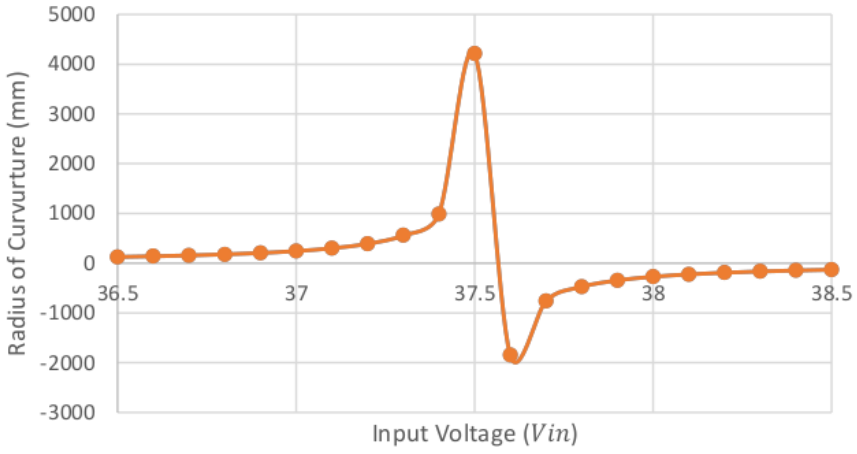

Figure 3.3: Radius of curvature for an Arctic 58NO liquid lens given an input voltage V_{in}.

Table 3.1: Measured and Estimated Properties of the Arctic 58NO liquid lens used for results presented in this document.

Property of Parameter	Symbol and Value
Height of non-polar liquid (liquid 1)	$h_1 = 0.376$ mm
Height of polar liquid (liquid 2)	$h_2 = 1.674$ mm
Refractive index of non-polar liquid (liquid 1)	$n_1 = 1.3984$
Refractive index of polar liquid (liquid 2)	$n_2 = 1.5196$
Voltage amplitude for flat meniscus	$U_0 = 48$V
Radius of flat meniscus	$R = 3.87$mm
Radius of aperture	$R_a = 2.9$mm
Bi-polar square wave forcing frequency	1070Hz

The table below gives the dimensions of the lens that were used for the calculations presented in this document.

The optical power of the liquid lens has a linear relationship with voltage amplitude between 25V–54V, as shown in Figure 3.4. Outside of this range, the lens does not show significant response to a change in electric potential.

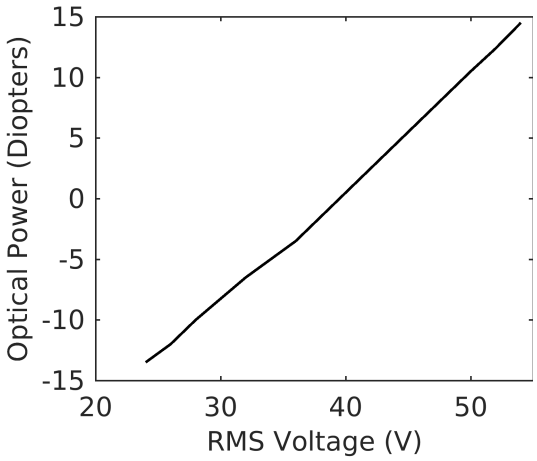

Figure 3.4: The estimated optical power of the liquid lens for given voltages, based on information given by Varioptic (now Corning) company documentation [47].

As seen in the radius of curvature plot in Figure 3.3 and the optical power plot in Figure 3.4, the liquid lens meniscus can have a convex or concave shape, depending on the voltage amplitude. A Zemax OpticsStudio [75] model comes with the lens kit, and ray tracing for different voltages applied to the lens can be found. Two examples of ray tracing are given in Figure 3.5, with forcing at 37.5V and 50V.

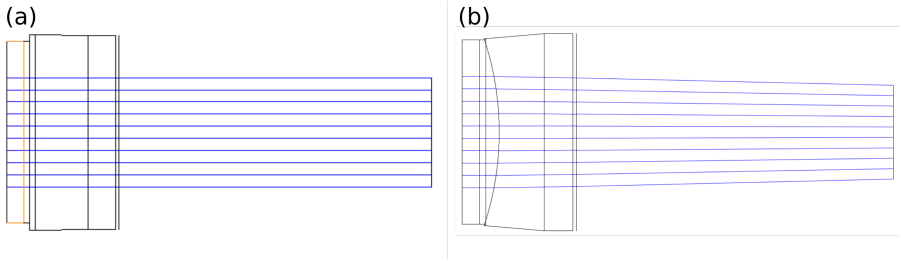

Figure 3.5: Simulated ray tracing in Zemax OpticsStudio [75] using a model of the Arctic 58NO liquid lens given a voltage input of (a) 37.5V and (b) 50V. The lens is concave when a voltage below 37.53V is applied, and convex when a voltage above 37.53V is applied.

3.2 Electrical Characteristics

To drive the electrowetting lens, a simple circuit with a DC power source and piezoelectric AC amplifier was constructed. Figure 3.6 shows a diagram of the circuit, which makes use of the PDm200B miniature high voltage amplifier [76], as well as a voltage controlled 24V DC power source, a voltage divider, and a National Instruments [77] analog to digital converter for real-time measurement of the voltage across the voltage divider. The power source was connected to ground, and has a positive DC voltage of 24V. The National Instruments [77] analog to digital converter was also used for producing bi-polar AC signals, with the positive and negative leads connected to the AC amplifier.

When the lens was forced with a bi-polar square wave, the measured voltage across the electrowetting liquid lens showed overshoot and oscillation during charging. An example measurement is given in Figure 3.7. A close-up of the measurements shown in Figure 3.7(a) is shown in Figure 3.7(b). The oscillations show the shape of a triangle function and an amplitude that remains constant for several cycles before abruptly diminishing.

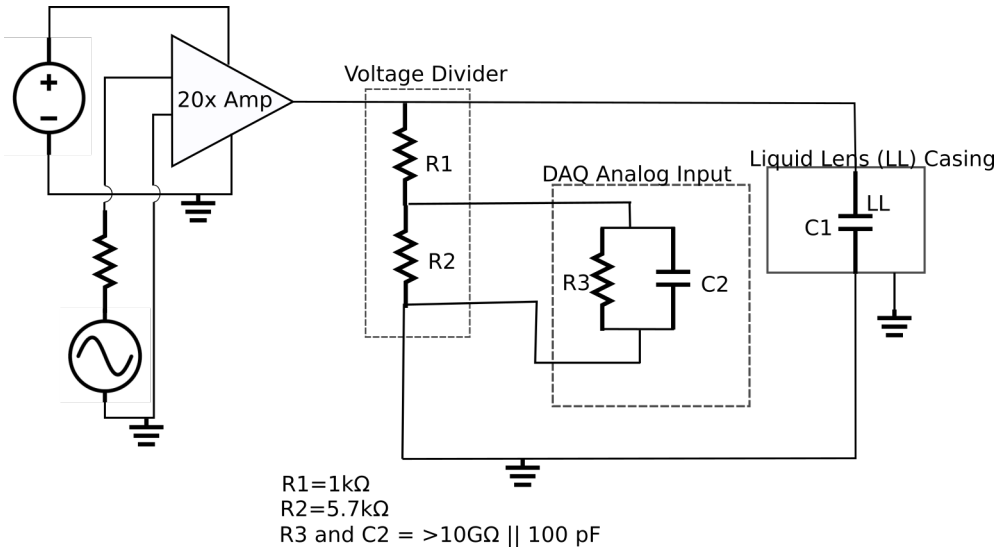

Figure 3.6: Custom circuit used to drive the electrowetting liquid lens. The symbol LL is for "liquid lens," digital acquisition system (DAQ) is for the digital acquisition system, and 20x Amp is for the AC amplifier.

The shape of the movement resembles a stick-slip condition [78, 79]. It is thought that this response is due to nano-scale surface variations on the side-wall of the lens that the liquid contact angle must overcome during charging, but not during discharging. The problem is no double exacerbated by an inability of the DC power source to maintain a stable voltage. The overshoot in Figure 3.7 was partially reduced by placing a capacitor in parallel with the liquid lens, and by changing the DC power supply. Initially a "wall-wart" 24V DC power supply was used. An Agilent E3612A DC power supply was substituted, and proved to provide a more stable voltage control. The capacitor placed in parallel with the lens increased the effective time constant of the lens, and reduced the overshoot.

The response in Figure 3.7 shows an asymmetry between charging and discharging. If the lens is modeled as a capacitor, this makes it an asymmetric capacitor, with different time constants depending on the polarity of the applied voltage step. A systematic study published by Na et al. in 2018 found that this is the case with commercial lenses from Corning [80]. In the study, Na et. al.

In the study by Na et. al., the mechanism that causes this asymmetry was elucidated

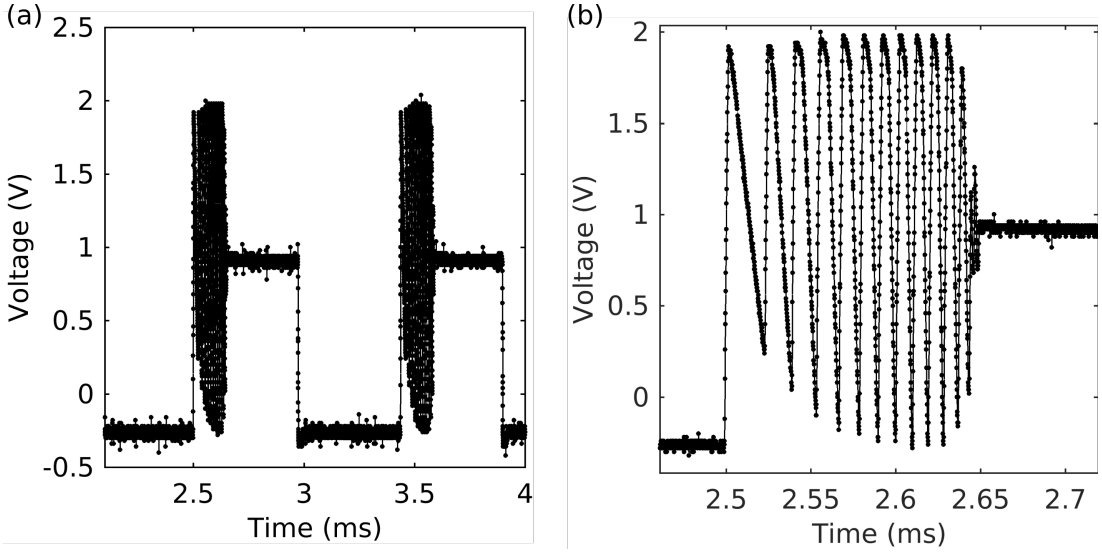

Figure 3.7: The voltage across the liquid lens over time, while the lens was driven with a 1070 Hz, 48V amplitude bi-polar square wave. The voltage was measured across a voltage divider due to range constraints of the oscilloscope. The measurements are also vertically shifted so that the mean is non-zero, which is due to the oscilloscope settings and not the actual signal.

[80]. The ions in the aqueous solution move near the contact line when the electric potential is changed. At the instant when a positive polarity voltage is applied, negative charged ions are in the dielectric layer separating the liquids from the outer electrode. These negative ions are trapped in the dielectric layer as the polar liquid switches polarity. The ions are then released, and the lens deflection reverses direction. Positive ions began diffusing into the dielectric layer. When a negative voltage is applied, the positive ions are momentarily trapped in the dielectric, but release much quicker than the negative ions. This produces an asymmetric meniscus deflection response, and an asymmetric electrical response [80].

Chapter 4

MEASURING THE MENISCUS PROFILE

Optical measurement is needed for non-contact measurement of liquid lens menisci. Though optical imaging of liquid lenses is often done through the lens side-wall [5, 46, 49], commercially available lenses do not have transparent side-walls [47]. For opaque side-walled lenses, it becomes necessary to develop an axial optical technique for measurement of the meniscus profile amplitude and shape over time. The amplitude can be measured with a photodiode [80], or with a camera positioned sufficiently far from the lens [60]. However, to measure the displacement over all spatial positions, an interferometry technique is needed.

Digital holographic interferometry (DHI) is a highly accurate, high-speed, non-contact method of measuring the shape and amplitude of refractive index and/or optical path length changes. DHI is a phase method that requires coherent illumination traveling through the top and bottom windows of the lens. DHI can measure optical path length changes on and in objects down to 1/100 of the used optical wavelength λ [81, 82].

This chapter describes in detail how DHI was used to measure a liquid lens meniscus profile. Measurements of oscillations on an Arctic 58NO [47] electrowetting liquid lens (described in Chapter 3) while being forced at frequencies from f_f = 10–200Hz and at amplitudes U_0 = 1.8V–8V are presented. These measurements are compared to predicted shapes using the Bessel function and Legendre function models discussed in Chapter 2. The displacement oscillation frequency along the center axis of the lens, as well as the shape of the oscillations over time is discussed for different forcing frequencies. Finally, conclusions on the displacement oscillations of the Arctic 58NO lens relevant to optical applications are given.

4.1 Digital Holographic Interferometry (DHI) Theory

Reference beam DHI allows for reconstruction of a complex wavefield [81, 82] at discrete times. A series of intensity interferograms recorded by a camera can be used to extract spatiotemporal phase changes between an objective beam and a reference beam. Though phase shifting interferometry [81] with a moving camera stage is often used for measurement of phase, we use an off-axis reference beam configuration for these experiments because of the dynamic nature of the oscillations. The off-axis configuration as part of a Mach-Zehnder interferometer is shown in Figure 4.1.

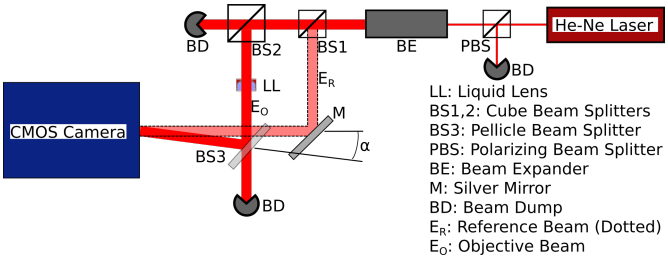

Figure 4.1: Figure 2: Mach-Zehnder interferometry set-up for DHI measurements. Red lines symbolize the coherent beam path, which separates at BS1 and combines incident upon the CMOS sensor with an angle α between the two beam paths. From [62].

The intensity from both the reference beam E_R and objective beam E_o is

$$\begin{aligned} I_h(x,y,t) &= (E_o(x,y,t) + E_R(x,y)) \cdot (E_o(x,y,t) + E_R(x,y))^* \\ &= |E_R(x,y)|^2 + |E_o(x,y,t)|^2 + E_o(x,y,t)E_R{}^*(x,y) + E_o{}^*(x,y,t)E_R(x,y). \end{aligned} \tag{4.1}$$

The last two terms contain the complex wavefield of the object beam $E_O(x,y,t)$. The dominating first two terms, the intensities of the reference and objective beams, can be approximately eliminated and neglected. This is done by first measuring the intensity of the reference beam while blocking the objective beam. With the assumption that the reference beam is not changing significantly within the measurement time, the $|E_R(x,y)|^2$ term can be subtracted. The objective beam intensity term $|E_o(x,y,t)|^2$ needs to be separated from the other terms by numerical propagation to another plane.

A Fresnel convolution approach can be used to compute a complex wavefield at the

plane of the meniscus profile from the intensity $I_h(x, y, t)$. The diffracted light-wave at the reconstruction image plane can be expressed using the Fresnel-Kirkoff integral as

$$\Gamma(\xi, \eta) = \frac{i}{\lambda} \int_{-\infty}^{\infty} \int_{-\infty}^{\infty} I_h(x, y, t) {E_R}^*(x, y) \frac{\exp(-ik\rho)}{\rho} dxdy, \tag{4.2}$$

where k is the wavenumber. The complex conjugate of the reference beam is used here so that the real image is not distorted [81]. The absolute reconstruction distance is

$$\rho = \sqrt{(x - \xi)^2 + (y - \eta)^2 + d^2}, \tag{4.3}$$

with d as the distance in the propagation direction, the coordinates (x, y) used in the hologram plane, and the coordinates (ξ, η) used for the reconstruction image plane. Equation 4.2 can be re-written as

$$\Gamma(\xi, \eta, t) = \int_{-\infty}^{\infty} \int_{-\infty}^{\infty} I_h(x, y, t) E_R^*(x, y) g(\xi, \eta, x, y) dxdy, \tag{4.4}$$

where the impulse response is

$$g(\xi, \eta, x, y) = \frac{i}{\lambda} \frac{\exp[-ik\sqrt{(x - \xi)^2 + (y - \eta)^2 + d^2}]}{\sqrt{(x - \xi)^2 + (y - \eta)^2 + d^2}}. \tag{4.5}$$

The image multiplied by the conjugate of the reference beam $I_h(x, y, t){E_R}^*(x, y)$, after the intensity of the reference beam $|E_R(x, y)|^2$ has been subtracted, gives the terms

$$I_h(x, y, t){E_R}^*(x, y) = |E_o(x, y, t)|^2 {E_R}^*(x, y) + E_o(x, y, t)({E_R}^*(x, y))^2 + {E_o}^*(x, y, t)|E_R(x, y)|^2. \tag{4.6}$$

The two-dimensional Fourier transform must be performed for reconstruction. This is done digitally, with spatial frequencies $f_x = l/(L\Delta x)$ and $f_y = w/(L\Delta y)$ where $l = 0, 1, \ldots, L-1$ and $w = 0, 1, \ldots, L-1$ are integer values representing pixels in a square array with pixel width Δx and height Δy. The absolute reconstruction distance ρ is approximated using the first three terms of a Taylor series expansion, given the assumption that the recreation distance $d \gg 2R$, where R is the radius of the liquid lens. We can write the discrete, transformed impulse response as

$$G(l, w) = \exp\left[-idk\sqrt{1 - \left(\frac{\lambda l}{L\Delta x}\right)^2 - \left(\frac{\lambda w}{L\Delta y}\right)^2}\right] \tag{4.7}$$

The reconstructed wave-field, using Fourier transforms becomes

$$\Gamma(l,w,t) = \Im^{-1}\{\Im\{I_h \cdot E_R^*\} \cdot G\}, \tag{4.8}$$

where l and w are pixel values for a grid $L \times L$ with $\Delta l = 2R/L$. Equation 4.8 can be solved discretely with fast Fourier transforms (FFTs).

This gives three distinct complex images: the reduced image from the $E_R{}^*|E_O|^2$ term, and the two conjugate images that contain phase information. A region of interest around one of the twin images gives the complex objective beam image $\Gamma_R(l,w,t)$, The difference in the phase of $\Gamma_R(l,w,t)$ from frame $n-1$ to frame n, $\Delta\phi_n = Arg\{\Gamma_R(l,w,t_n)\} - Arg\{\Gamma_R(l,w,t_{n-1})\}$ is a measurement of how the meniscus profile is changing the phase of the objective beam over discrete time changes $\Delta t = t_n - t_{n-1}$. Within a scalar diffraction approximation, the phase difference $\Delta\phi_n$ at a specific forcing frequency f_f and voltage amplitude U_0 can be equated to

$$\Delta\phi_n(l,w,t_n) = k(n_2-n_1)P(\cos(2\pi f_f t_n) - \cos(2\pi f_f t_{n-1}))J_0(2\pi f_f\sqrt{l^2+w^2}/c), \tag{4.9}$$

where k is the optical wavenumber. this takes advantage of the standing wave solution, Equation 2.46. We write this equation as $\eta(r,t) = Pcos(2\pi f_f)J_0(2\pi f_f r/c)$ for measurements in this Chapter, with the amplitude symbolized by P.

If there is a sufficient number of frames per second, the amplitude of the oscillations can be estimated by measuring the phase difference at the center ($l = w = L/2$). At time step t_n, this is

$$\Delta\phi_n(L/2,L/2) = k(n_2-n_1)P[\cos(2\pi f_f t_n) - \cos(2\pi f_f t_{n-1})] \tag{4.10}$$

$$= -2kP(n_2-n_1)\sin(\pi f_f \Delta t)\sin(2\pi f_f t_{n-1} + \pi f_f \Delta t), \tag{4.11}$$

Equation 4.11 gives the phase difference as a constant multiplied by a phase shifted sin() function. This was used to determine the amplitude, frequency, and phase of the oscillations.

4.2 DHI Measurements

A custom Mach-Zehnder interferometer was used to image the oscillations on a liquid lens. A He-Ne continuous wave laser with a wavelength $\lambda \approx 632.8$nm was used. The reference

beam and objective beam were separated by an angle of 0.01 radians, which was chosen so that the fringes were not too narrow for the pixels of the sensor [81]. The distance from the liquid lens meniscus profile to the complementary metal-oxide-semiconductor (CMOS) sensor was 613 mm. A high-speed Phantom v711 CMOS camera was used to record the combined beams at 13000 fps over an exposure time of 3 μs. The CMOS sensor had square pixels of 20 μm width and an array size of 800x600 pixels. The specifications of the Arctic 58NO lens [47] that was used are in Chapter 3. The lens was fixed in the horizontal position, with orientation of the glass top and bottom perpendicular to the plane of the optical table.

The lens was forced to an approximately flat profile with a 48V amplitude 1070 Hz square wave signal. Low frequency (f_f = 20–200Hz) harmonic signals $U_0 exp(i2\pi f_f t)$ were added to the square wave signal. While this means that the time-spectrum of the signal had higher frequency components from the square wave, it was assumed that these components were all $> 5\times$ greater than f_f.

The experimentally measured interferograms contoured periodically with a frequency that matched that of the harmonic forcing signal. Fig. 4.2(a) and Fig. 4.2(b) show a measured interferogram for what was found to be the first resonant frequency f_f = 38 Hz and Fig. 4.2(c) shows the intensity of the three images (the three terms of Equation 4.6) after numerical propagation. The phase change around the lens region $\Delta\phi_n$ is shown in Fig. 4.2(d).

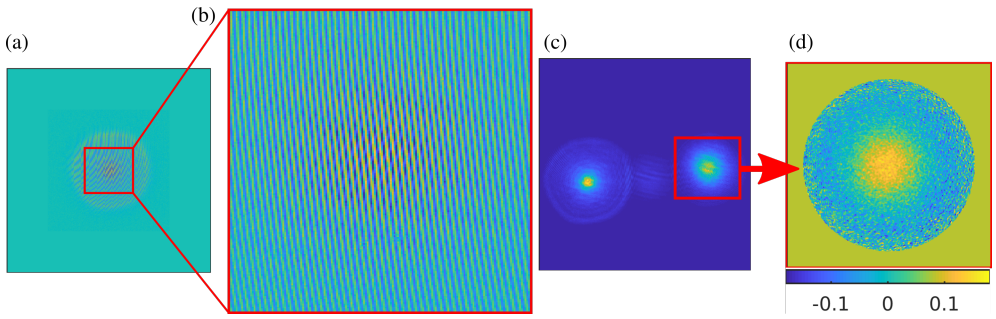

Figure 4.2: (a,b) Measured intensity interferogram while f_f = 38Hz and U_0 = 3.0V. (c) The intensity after numerical propagation to the image plane. (d) The phase difference (radians) between the current and the previous frame (not shown) in the region of interest Γ_R. From [62].

The amplitudes of oscillations were estimated using a non-linear least squares (NLLS) fit. Taking advantage of Eq. (4.11), the fitting function was $\tilde{A}sin(\tilde{B}t + \tilde{C})$. Fig. 4.3(b) shows the least-squares estimated function plotted with measurements at the center ($l = w = L/2$) when $f_f = 38$ Hz and $U_0 = 3.0$V. The adjusted r^2 value for this example was 0.95, and the mean adjusted r^2 value for the plotted measurements in Fig. 4.3(a) was 0.92. The red markers in Fig. 4.3(a) show the amplitudes P when equating $\tilde{A} = -2kP(n_2 - n_1)\sin(\pi f_f \Delta t)$ from $f_f = 20$–200Hz. The mean of the phase difference was subtracted for each frame for robustness. The mean, however, is expected to be non-zero for $2\pi f_f t_{n-1} + \pi f_f \Delta t \neq 2\pi m$, for some integer m. Therefore, this subtracts both signal and any offset from noise. If the signal mean was added back to the amplitude, Fig. 4.3(a) would maintain the same shape, but with slight amplification.

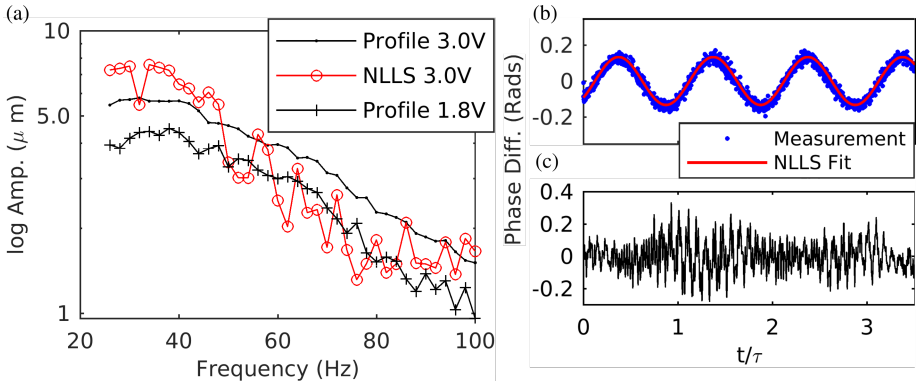

Figure 4.3: (a) The amplitude of meniscus oscillations for different forcing frequencies using the summed profile measurements (black markers) and the NLLS fit to peak amplitude measurements at each frame (red markers). (b) The amplitude of the center point after subtracting the mean over three full oscillation periods (3τ) when $f_f = 38$ Hz (blue markers), with the non-linear least squares estimation shown as a red continuous line. (c) The mean phase difference subtracted for each amplitude in (b). From [62].

The discrete time spectrum of the mean of the phase difference contained peaks at the forcing frequency f_f, $f_f/2$, and two higher frequencies 429Hz and 1468Hz. A plot of the mean phase difference for the same measurements that produced the amplitude plot in Fig. 4.3(b) is shown in Fig. 4.3(c). This amplitude offset is partially due to the meniscus profile not being perfectly stable, even without the harmonic forcing $U_0\cos(2\pi f_f t)$. The 1070 Hz

bipolar square wave can hold the liquid lens at a certain contact angle in a near equilibrium state, but slight movement persists.

To measure the amplitude of the oscillations, the phase difference can be summed over multiple frames. Using estimated peak signals, such as the one in Fig. 4.3(b), the phase of the oscillations was determined. Starting with the frame associated with a flat profile, phase changes were summed until the frame associated with a maximum amplitude profile. This was done over two oscillation periods for averaging.

Noise in the measurements was mostly zero-mean, and canceled in the summed profiles. The summed offsets $\tilde{h}$ were subtracted from the final profiles using the formula

$$\tilde{h} = \frac{\tilde{P}_p(r_c/\tilde{r}_c - 1)}{r_c - 1}, \tag{4.12}$$

where $\tilde{P}_p$ is the estimated amplitude of the Bessel function shape (with the offset), $\tilde{r}_c$ is the ratio $\tilde{P}_p/\tilde{P}_a$, where $\tilde{P}_a$ is the measured anti-node value, and r_c is the expected ratio. The expected ratio r_c does not change with frequency, and so the offset $\tilde{h}$ can be estimated with only $\tilde{P}_p$ and $\tilde{P}_a$. Fig. 4.4 shows the cross-section of a summed profile before and after the offset was subtracted. The resulting summed profiles were used to compile an amplitude

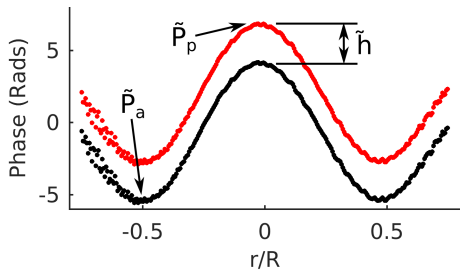

Figure 4.4: The cross-section of the measured summed profile for $f_f = 38$Hz before (black) and after (red) subtracting the offset $\tilde{h}$. From [62].

frequency response for 26–100 Hz. The amplitude of summed profiles after the offset was subtracted are shown in Fig. 4.3(a). The system is heavily damped, making resonant peaks less pronounced. The response from $U_0 = 1.8V$ has a peak at $f_1 = 38$Hz. Oscillations at this frequency are used often in this chapter as examples.

4.2.1 Measurements of the flat profile

Measurements of the profile without the $U_0 \cos(2\pi f_f t)$ forcing revealed periodic shifting of the profile.

The meniscus profile was measured when the lens was only forced with the 48V amplitude 1070Hz bi-polar square wave ($U_0 = 0$). By summing the phase changes between each frame, the displacement of the meniscus was measured at discrete times at intervals of $77\mu s$. The spectrum of this signal had one peak at what is presumed to be the first resonant frequency, 43Hz, and peaks at 429Hz and 1468 Hz, with the largest peaks at the resonance frequency and 429 Hz. The maximum amplitude was $5.15\mu m$, and the measured variance was 4.0 μm. An example measurement of the center amplitude $r = 0$ is given in Figure 4.5.

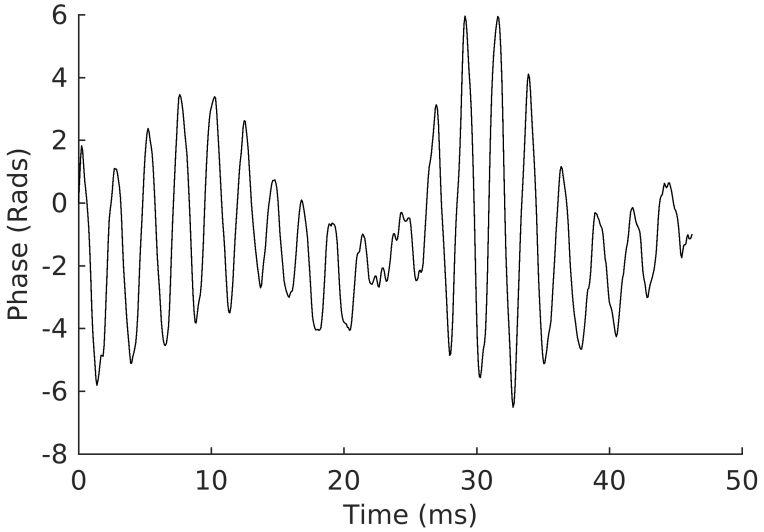

Figure 4.5: The displacement of the meniscus center over time when a square wave voltage of amplitude $U = 48$V was applied to force a flat profile, but no harmonic forcing was applied $U_0 = 0$.

The response of the lens when the voltage was changed from 41.4V to 9.2V and 41.4V to 58.8V was measured. Examples of this response are given in Figure 4.6(a) and Figure 4.6(a), where the change begins at approximation 60ms. This was not a true step response, as the voltage was ramped to avoid overshoot and oscillations. This does, however, give us a quantitative measurement on how fast the lens can change from a flat profile to an

extreme focal length. True step response measurements for the Corning lenses (previously Varioptic) have been published by Berge et al. [43].

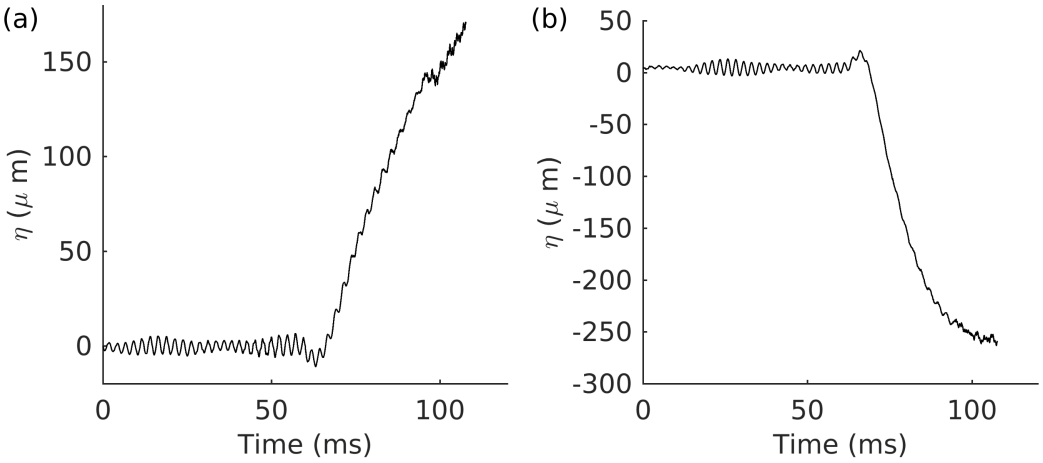

Figure 4.6: The displacement of the meniscus center over time when a ramped square wave voltage of frequency 1070Hz was applied. The voltage was changed from (a) 41.4V to 9.2V and (b) 41.4V to 58.8V.

4.2.2 Amplitude dependence on Voltage and Resonance Frequency

The amplitude of the oscillations was found to be linearly correlated to the forcing amplitude. An example of oscillation amplitudes measured at the same frequency, but with different forcing amplitudes is given in Figure 4.7 for $U_0 = 1$V to $U_0 = 3$V. A linear slope was fitted to the measurements in Figure 4.7. The resulting linear equation can be used to predict the amplitude of oscillations when $f_f = 44$Hz for certain forcing amplitudes U_0. This process can be repeated for measurements at different f_f to make predictions of oscillation amplitudes for certain f_f and U_0.

The highest amplitude measured for the same voltage amplitudes and various frequencies was initial taken to be associated with the first resonance, or natural frequency. The first method was taking the maximum amplitude of the frequency response, which is $f_1 = 38$Hz for forcing of $U_0 = 1.8$V. Using the membrane model proposed in [60, 61], the wave speed can be calculated to be $c = 2\pi R f_1 / j_{1,1} = 24 \pm 1$ cm/s, which can be compared to the

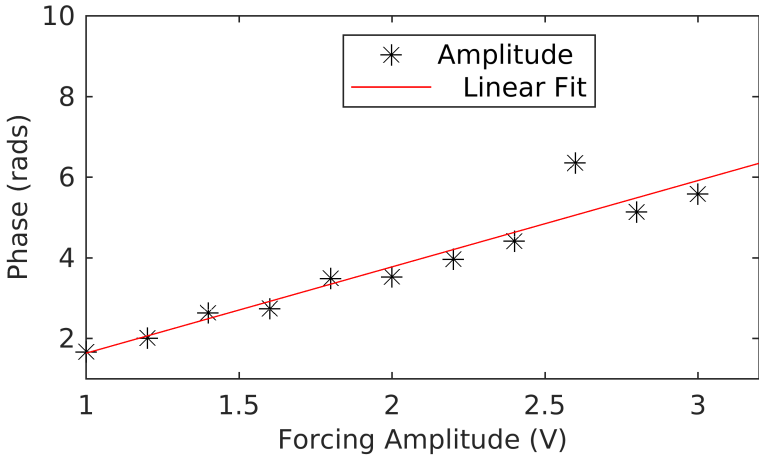

Figure 4.7: The amplitude of the oscillations at $f_f = 44$Hz for different forcing amplitudes U_0, fitted to an equation using linear regression.

calculated $c = 26 \pm 6$ cm/s in [60] for a smaller diameter lens, made by the same company. However, the frequency response in Figure 4.3(a) suggests that the system acts like a heavily damped second order dynamic system. The peak amplitude is not necessarily associated with the natural frequency in heavily damped systems, but is associated with a damped frequency $f_d < f_1$ [83].

The frequency spectrum of oscillations excited by the 1070 Hz square wave contained a frequency $f_1 \approx 43$Hz. If it is assumed that the system behaves like a harmonically forced second order system, we can take this frequency to be the first resonance frequency for the system [83]. Using this frequency, $c = 2\pi R f_1 / j_{1,1} = 27 \pm 1$ cm/s, which is closer to what was reported in [60].

4.2.3 Comparing measurements to the Bessel function model

A two-dimensional plot of the summed profile phase for $f_f = 38$Hz and $f_f = 160$Hz is shown in Fig. 4.8. The cross-sections of the measured profiles are compared with the corresponding Bessel function model for standing waves $\eta(r,t) = Pcos(2\pi f_f) J_0(2\pi f_f r/c)$. The phase measurements are once again limited to a region $r < 0.75R$ due to the 5.8mm aperture. For the $f_f = 38$Hz cross-sections, the root mean squared (RMS) difference was

25nm and 13nm for $U_0 = 1.8V$ and $U_0 = 3.0V$ when $r < 0.50R$, and 47nm and 34nm when including all data points $r < 0.75R$. If the shape of this Bessel function is plotted against a

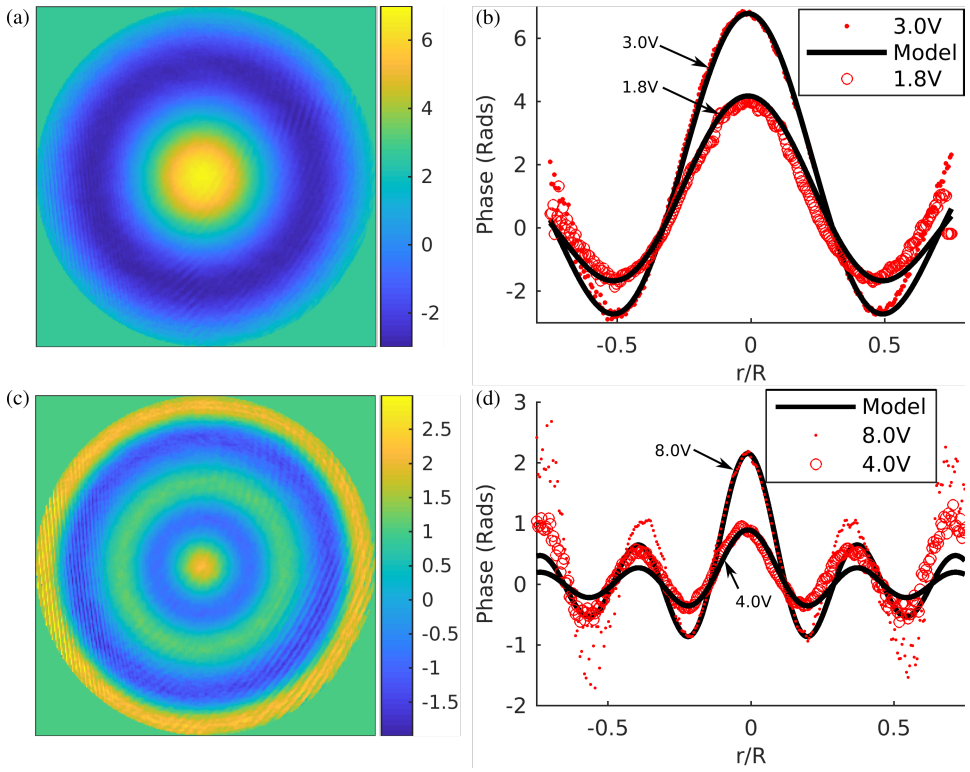

Figure 4.8: The measured amplitude profile for (a) $f_f = 38$Hz and (c) $f_f = 160$Hz. The cross-section of the measured and modeled (Equation 2.47) profiles for (b) $f_f = 38$Hz and (d) $f_f = 160$Hz with forcing amplitudes $U_0 = 1.8, 3.0, 4.0, 8.0$V. From [62].

Bessel function using $k_1 = j_{1,1}/R$, there is a near perfect match, as shown in Figure 4.9(a). However, the maximum amplitude for f_f has a different shape. If $k = 2\pi f_f/c$ is tuned so that $f_f = 38$Hz and $c = 12$cm/s, the model matches the measurements, as shown in Figure 4.9(b). The $k = 2\pi f_f/c$ model can more closely be compared to $k = j_{1,2}/R$, but does slightly depart at larger radial distances from the center. It was found that $f_f = 43$Hz made a closer match. If we assume that $f_2 = 38$Hz or $f_2 = 43$Hz, the second root can be used to calculate a wave speed of $c = 13$cm/s, which is exactly half of what was measured by Strauch et. al. in [60]. The mode shape model and the continuous frequency model match perfectly in this case.

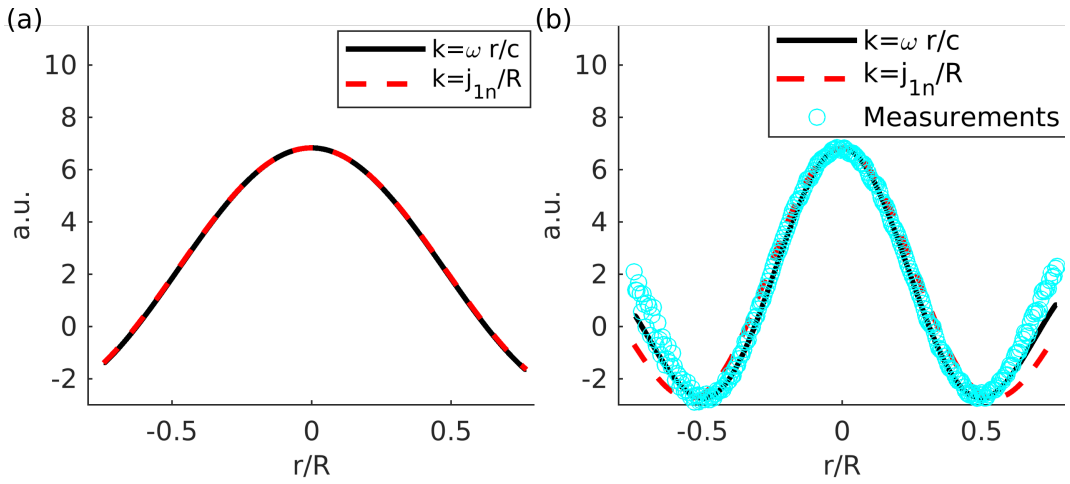

Figure 4.9: (a) The predicted amplitude of meniscus displacement for the first mode $k_1 = j_{1,1}/R$ and for $k = \omega r/c = 2\pi f_f/c$ with $f_f = 38$Hz and $c = 24$cm/s. (b) The measured amplitude of meniscus displacement for $f_f = 38$Hz and $U_0 = 3$V and the predicted amplitude using $k_2 = j_{1,2}/R$ and $k = 2\omega r/c = 2\pi(2f_f)/c$ with $f_f = 38$Hz and $c = 24$cm/s.

This can mean that $f_f = 43$Hz corresponds to the second resonance, and therefore to the second root of the Bessel function of the first kind, and second degree. Or, this can mean that twice the value of the driving frequency must be used to calculate the shape, which would give a displacement model of

$$\eta(r,t) = AJ_0\left(\frac{2\pi(2f_f)r}{c}\right) cos(2\pi f_f t) \tag{4.13}$$

where $c = 24$cm/s. The wave speed cannot remain constant in order to match predicted profiles with measurements, however. For frequencies $26 - 100$Hz, The wave speed followed a frequency dependent model $\tilde{c} = a_c 2\pi/(j_{1,1}(1 + \gamma/f_f))$, for a constant γ, but diverged for higher frequencies.

There are several problems with using the simple, one term, standing wave Bessel function model. It can be seen in Fig. 4.8(b) that the profiles compare well with the model at smaller radial values ($r \leq R/2$ for $f_f = 38$Hz), but diverge at greater radial values. Also noticeable from Fig. 4.8(b) and 4.8(d) is how this divergence increases with frequency and forcing amplitude U_0. The three phase nodes in Fig. 4.8(d) alternate in magnitude, going from high (center) to low (2nd) to high again (3rd), in contrast with a Bessel function,

which has nodes gradually decrease in value from the center. It is noted that the velocity potential of the meniscus should increase with an increase in frequency, or an increase in forcing amplitude. The velocity potential that relates to the Bessel function displacement model is a solution for a cylindrical geometry, and the Arctic 58NO has a conical frustum geometry at the bottom where the meniscus is moving.

4.2.4 Comparing measurements to the Legendre function model

The Legendre function model discussed at the end of Chapter 2 was fitted to the measurements. The amplitude A_n was tuned to match the center axis amplitude of the measurements, giving the best match between the measurements and the model near the center axis. Figure 4.10 shows a comparison of the measurements for $f_f = 38$Hz and $f_f = 160$Hz with the Bessel function and Legendre function models. These measurements are the same as the ones shown in Figure 4.8. It can be seen in Figure 4.10(a) and Figure 4.10(b) that for $U_0 = 1.8V$ and $f_f = 38$Hz, the measurements matched the Bessel function model slightly better than the Legendre function model. At the edge of the measurements ($r = 0.75R$), both models follow the measurements very closely. At the edges, however, the percent difference between the Legendre function model and the measurements was 291%, while the percent difference between the Bessel function model and the measurements was 29%. The percent difference between the measurements and the Legendre function decreased to 35% when $U_0 = 3$V, while the percent difference for the Bessel function model increased to 81%. These differences were increased for $f_f = 160$. In general, the Legendre function over-predicts amplitudes near the contact angle, while the Bessel function model under-predicts amplitudes. The Bessel function matches the measurements better for lower forcing amplitudes, and the Legendre function model mathes better for higher amplitudes. The overshoot of the Legendre function model could be due to the absence of the contact line friction and viscosity in the development of the Legendre function model. The boundary condition at $\theta_s = \alpha_s$ must be altered, and a full solution that satisfies the jump in normal stress at the contact line must be developed.

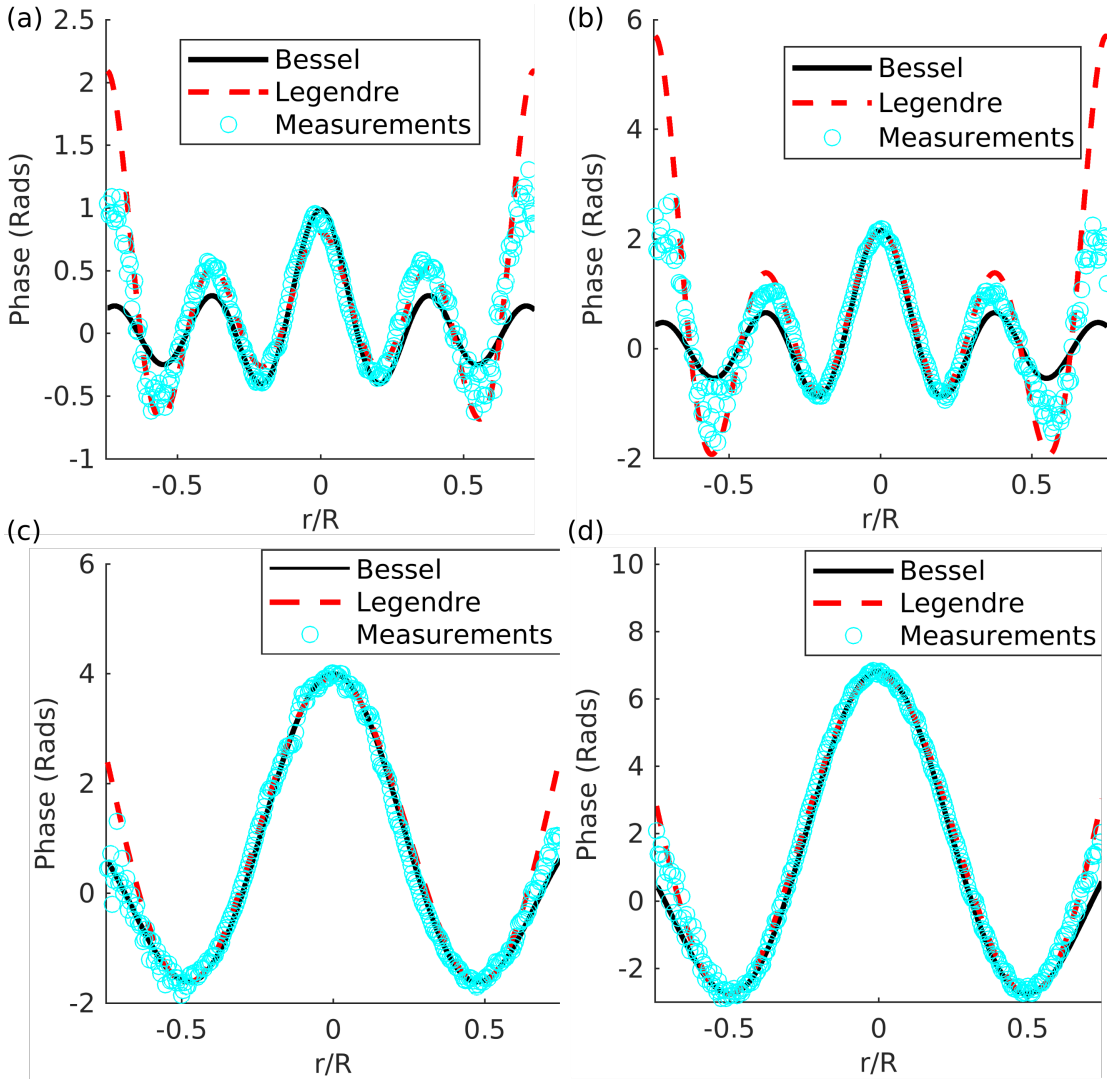

Figure 4.10: Plots of the maximum meniscus displacement measured by DHI and modeled using the Legendre function model (conical shape solution) and Bessel function model (cylindrical shape solution) for (a) $f_f = 160$Hz and $U_0 = 4$V, (b) $f_f = 160$Hz and $U_0 = 8$V, (c) $f_f = 38$Hz and $U_0 = 1.8$V, (d)$f_f = 38$Hz and $U_0 = 3$V.

4.2.5 Oscillation Frequencies

The liquid mensicus was observed to oscillation at multiple frequencies. The phase difference time series measurements at frequencies near the resonance frequency showed the liquid oscillation frequency matched the forcing frequency. However, measurements of the summed

amplitude peak ($r = 0$) for higher forcing frequencies showed two dominant oscillation frequencies, one at the forcing frequency f_f, and one at $f_f/2$. Another frequency at $f_f =$ 430Hz was also observed. An example of this is shown in Figure 4.11, which has three center amplitude vs. time plots for $f_f = \{100, 90, 80\}$Hz forcing.

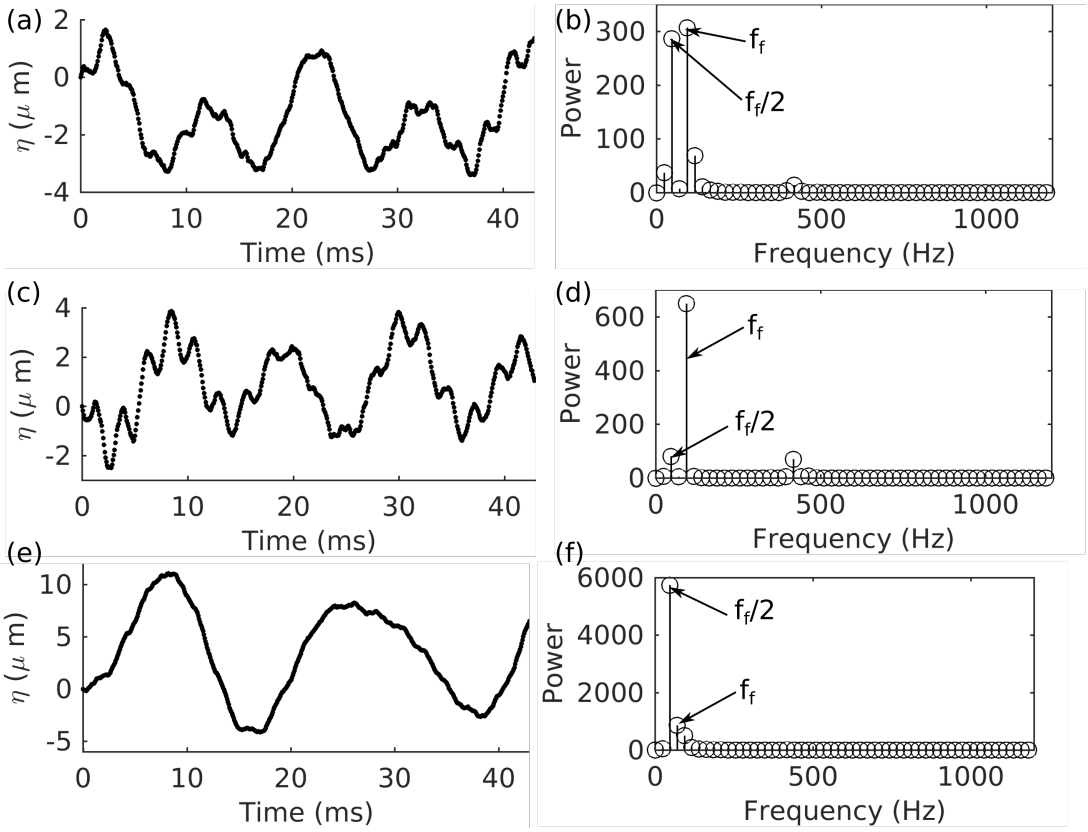

Figure 4.11: The maximum meniscus displacement measured by DHI at the center axis $r = 0$ for (a) and (b) $f_f = 100$Hz and $U_0 = 3$V, (a) and (b) $f_f = 90$Hz and $U_0 = 3$V, (a) and (b) $f_f = 80$Hz and $U_0 = 3$V. Plots (b), (d), and (f) are the time-series frequency spectrum of the time-series plots (a), (c), and (e).

The center peak oscillations for $f_f = 80$Hz show a cross-over into dominant sub-harmonic oscillations. In Figure 4.11(a), the liquid oscillations when $f_f = 100$Hz contain two dominate frequencies associated with f_f and $f_f/2$, which is shown in 4.11(b). The spectrum shows these frequencies at nearly the same power. the time-series in Figure 4.11(c) for $f_f = 90$Hz similarly has two dominant frequencies, plotted in 4.11(d). However, Figure 4.11(e) and

Figure 4.11(f) show that the $f_f/2$ frequency is the highest power frequency for $f_f = 80$Hz. This is similar to what is observed in Faraday parametric forcing of liquid-air systems with a shallow depth [52, 57, 84, 85, 86]. In parametric forcing, sub-harmonic oscillations often occur when the forcing frequency is approximately twice the natural frequency $f_f \approx 2f_1$ [85, 84]. In the case of the tested electrowetting lens, the forcing is likely also twice the natural frequency for the system $f_1 \approx 43$Hz and near twice the peak amplitude at 38Hz. It is difficult to comment on the cause of the dominant sub-harmonic oscillations. It could be the case that sub-harmonic oscillations are caused by non-linear effects that will not show up linear models that are discussed in Chapter 2 of this document.

4.2.6 Decomposing measurements into components

The simplest method of defining the shape of the meniscus oscillations on an electrowetting liquid lens is to expand the measured amplitude in a Fourier-Bessel series. Bessel functions are orthogonal, and can be infinitely summed to represent a continuous function. The Fourier-Bessel series for the meniscus profile amplitude is

$$\eta(r) = \sum_{n=1}^{\infty} F_n J_0(kr) \tag{4.14}$$

The coefficients F_n can be found using the orthogonality property of Bessel functions [87]. For the amplitude of η, the coefficients are

$$F_n = \frac{2}{R^2 J_1^2(k_n R)} \int_0^R \eta(r) J_0(k_n r) r dr \tag{4.15}$$

The above equation is sufficient when the eigenvalues $k_n = j_{0,n}/R$, where $j_{0,n}$ are the roots of the Bessel function of the first kind and zeroth order. We assume that there is no displacement in the radial direction, giving a boundary condition

$$\frac{\partial \eta}{\partial r}\Big|_{r=R} = 0. \tag{4.16}$$

This produces eigenvalues $k_n = j_{1,n}/R$, where $j_{1,n}$ are the roots of the Bessel function of the first kind and first order. This gives the following modified equation for the coefficients of the Fourier Bessel series:

$$F_n = \frac{2}{R^2 J_0^2(k_n R)} \int_0^R \eta(r) J_0(k_n r) r dr \tag{4.17}$$

where the Bessel function of the zeroth order has replaced the Bessel function of the first order in the denominator. When working with functions or sets of data defined in a non-periodic domain, the Hankel transform can be used to calculate a Bessel spectrum. The Hankel transform is related to the Fourier-Bessel series in much the same way that Fourier transforms are related to Fourier series [87], with one on a periodic domain and one on an infinite domain.

To study the modes of the electrowetting liquid lens meniscus profile oscillations at certain forcing frequencies, discrete Hankel transforms were performed on the amplitude measurements. An example of a measurement that was decomposed into a discrete Bessel spectrum is given in Figure 4.12. The spectral Bessel components of the profiles shown in

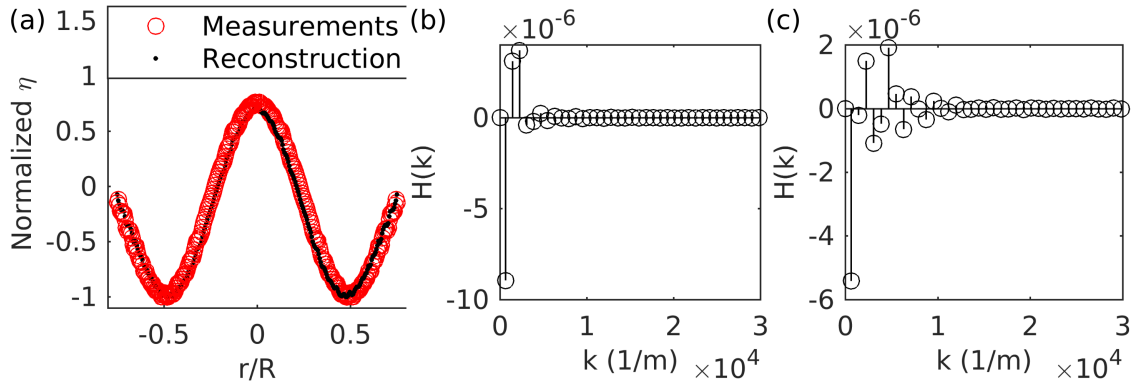

Figure 4.12: (a) Measured amplitude of the meniscus displacement when $f_f = 38$ and $U_0 = 3$V, and the corresponding amplitude after a discrete Hankel transform was performed on the measurements, and then an inverse discrete Hankel transform was used for reconstruction in the spatial domain. (b) Spectral components F_n from taking the discrete Hankel transform of the measurements in (a). (c) Spectral components F_n from taking the Discrete Hankel transform of measured amplitudes when $f_f = 160$ and $U_0 = 8$V

Figure 4.12(a) and Figure 4.12(b) have very different mode contributions. The spectrum for the displacement from $f_f = 38$Hz contains only three main low mode contributions, while the $f_f = 160$ measurements contain several higher order modes. The $f_f = 38$Hz amplitude shown in Figure 4.12(a) only needs 6 modes for 95% of the total summed value of all components, while the amplitude for $f_f = 160$ needs 30 modes.

The number of modes needed for 95% of the measured profiles was calculated for am-

plitudes at each forcing frequency f_f. Figure 4.13 shows a plot of the number of modes for frequencies $f_f = 20$–200Hz.

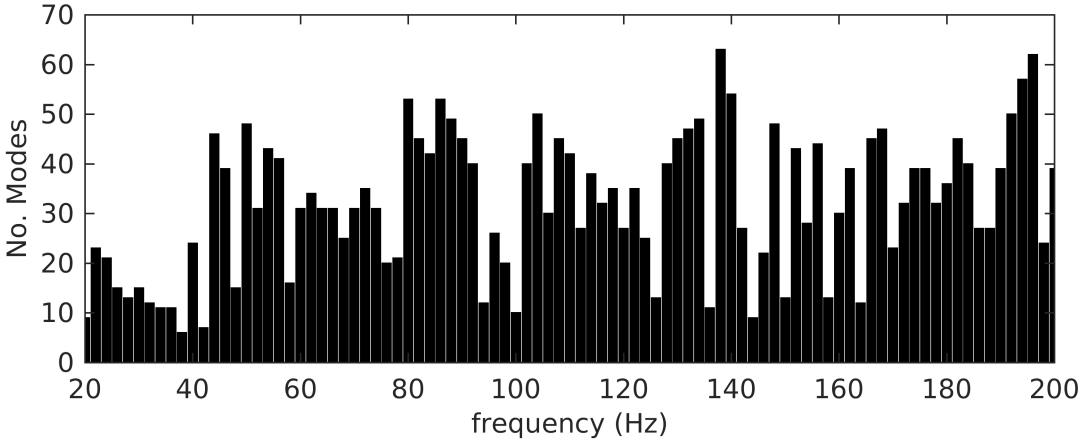

Figure 4.13: The number of modes needed for 95% of the Hankel spectrum power, for meniscus displacement amplitudes for frequencies $f_f = 20$–200Hz.

In general, the number of Bessel modes needed to reconstruct the measurements grows with an increasing forcing function f_f. Figure 4.13 shows the number of modes gradually increasing with forcing frequency f_f, though significant variation is also shown. When $f_f < 44$Hz, the number of modes never surpasses 24. The frequencies $f_f < 44$Hz are all below or around the resonant frequency for the lens, and therefore excite fewer, but more dominant modes in the lens.

The Hankel transform was also calculated for the profiles at other times during an oscillation period. It was discovered that the meniscus profile has a different shape during half of the oscillation period for forcing above the resonant frequency. An example of this is shown in Figure 4.14 for $f_f = 80$Hz, and $U_0 = 3$V.

As shown in Figure 4.14, the profile of the meniscus changes shape during a liquid oscillation period. During the first and last part of the oscillation, denoted by (a) and (d) in Figure 4.14, the profile shape has one large peak in the center, with two side peaks or nodes near $r = 0.75R$. The Hankel spectrum is similar for (a) and (d) in Figure 4.14, but changes at times (b) and (c). The shapes in (b) and (c) resemble a higher mode than the

shapes in (a) and (d). While viewing a video of the oscillations, it was observed that during the oscillation, at a time between (a) and (c), the peak amplitude at $r = 0$ folded into itself and a new mode shape emerged. This effect has been simulated using two oscillations in superposition, one at f_f and one at $f_f/2$. The sub-harmonic oscillation is of a lower order mode than the f_f oscillation.

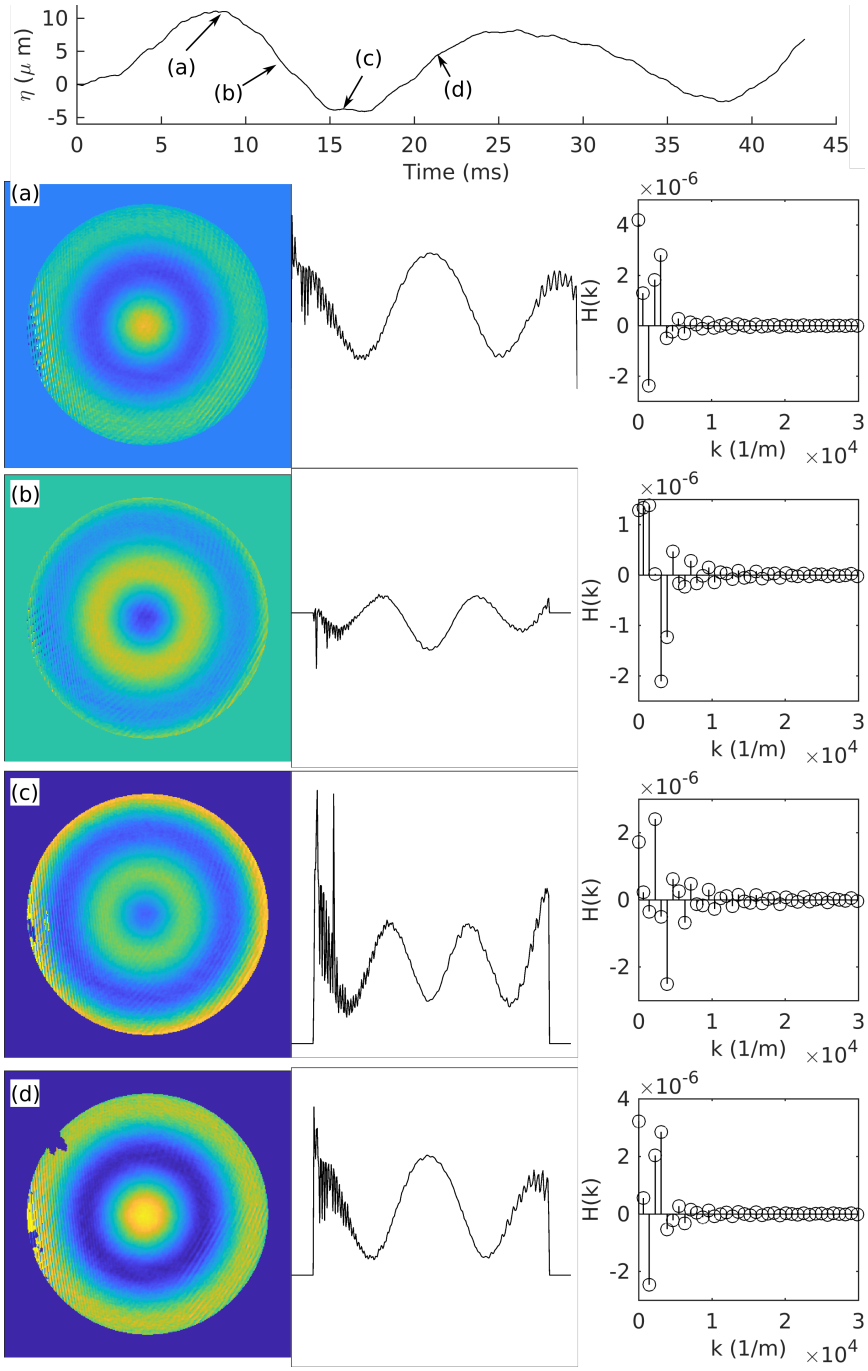

Figure 4.14: The meniscus profile 2-D image (left) and cross-section (middle) of the electrowetting lens when the forcing frequency $f_f = 80$Hz and $U_0 = 3$V. The Hankel transform spectrum (right) is plotted for each cross-section profile. (a-d) denote times, as labeled in the center amplitude plotted vs. time (top).

Chapter 5

SPATIAL PHASE MODULATION AND FAST FOCUSING APPLICATIONS

This chapter describes two practical applications of electrowetting lens oscillations: fast focus switching and wavefront correction. Oscillations at a single frequency can be used for focus switching, while oscillations excited by multi-frequency or pulsed forcing can be used to create a user-defined meniscus height profile and correct the wavefront of the beam. We describe the theory behind these two applications and give examples from recent publications.

5.1 Focus switching

Focus switching is the change in focal length of a lens system. This has been achieved in tunable liquid [88] and membrane lenses [10] with AC forcing at the resonance frequency. Liquid lenses offer the ability to continuously switch focal length as the meniscus oscillates. An example application of continuous focus switching in photoacoustic microscopy was demonstrated by Lee et al. in 2017 [10], and is illustrated in Figure 5.1. In the example from [10], the axial focal length of a tunable membrane lens was oscillated at the first resonance frequency. This allowed for an increase in the scanning speed of the sample. The changing focal length of the tunable membrane lens changed the effective focal length of the lensing system into the sample (shown in Figure 5.1), creating a larger axial scanning range in the sample. This same action could potentially be performed by electrowetting lenses that are driven at the resonance frequency.

For an electrowetting liquid lens with two non-miscible liquids of refractive index n_1 and n_2, the focal length can be calculated as a function of amplitude, frequency, and time. If a displacement on the meniscus of $\eta(r,t) = AJ_0(2\pi f_f r/c)\cos(2\pi f_f t)$ is assumed, the change in focal length of the center node can be estimated for a given amplitude A and a given

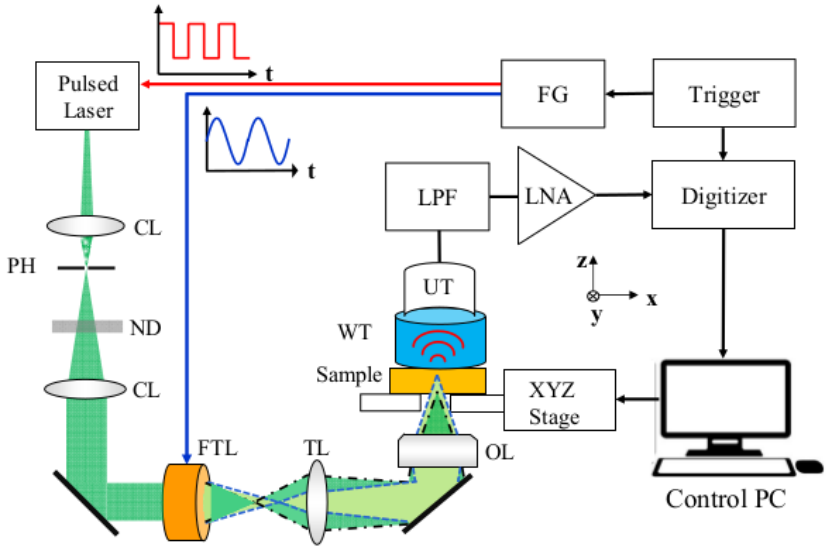

Figure 5.1: A diagram of a photoacoustic microscopy system that utilizes an oscillating tunable membrane lens to scan through a sample in the axial direction. PH denotes pin hole, CL is for the convex lenses, ND is a neutral density filter, FTL is the focus tunable lens, or tunable membrane lens, TL is a tube lens, OL is an objective lens, WT is a water tank, UT is an ultrasonic transducer, LPF is a low pass filter, and LNA is a low noise amplifier. Reprinted with permission from [10], Optical Society of America (OSA).

oscillation frequency f_f. Expanding the Bessel function about $r = 0$ in a Taylor series gives

$$J_0(\frac{2\pi f_f r}{c}) = 1 - \frac{(2\pi f_f)^2 r^2}{4c^2} + \frac{(2\pi f_f)^4 r^4}{64c^4} - \cdots \pm H.O.Ts. \tag{5.1}$$

where $H.O.Ts.$ symbolizes higher order terms. If we approximate the Bessel function by taking only the first two terms, the phase change at any time t and for any radial distance from the center r becomes

$$\Delta\phi = k(n_1 - n_2)A(1 - \frac{(2\pi f_f)^2 r^2}{4c^2}\cos(2\pi f_f t) \tag{5.2}$$

The transfer function with this approximation is

$$\begin{aligned} t_l &= \exp\left[jk(n_1 - n_2)A\cos(2\pi f_f t)\right] \exp\left[-jk(n_1 - n_2)\frac{A(2\pi f_f)^2}{2c^2}\frac{r^2}{2}\cos(2\pi f_f t)\right] \\ &= \exp\left[jk(n_1 - n_2)A\cos(2\pi f_f t)\right] \exp\left[\frac{-jkr^2\cos(2\pi f_f t)}{2f}\right], \end{aligned} \tag{5.3}$$

where the first exponential gives a spatially constant, but time-varying phase change, while the second exponential term gives a spatially and time varying phase change. The optical power becomes

$$\frac{1}{f} = \frac{(n_1 - n_2)A(2\pi f_f)^2 \cos(2\pi f_f t)}{2c^2} \tag{5.4}$$

and the focal length is

$$f = \frac{2c^2}{(n_1 - n_2)A(2\pi f_f)^2} \frac{1}{\cos(2\pi f_f t)} \tag{5.5}$$

For a given frequency f_f, the focal length is inversely proportional to the amplitude of the oscillations $f \propto 1/A$. As shown in Chapter 2 and Chapter 4, the width of the center node is inversely proportional to the frequency f_f. Additionally, the range of focal lengths possible is inversely related to the difference in refractive indices $n_1 - n_2$. In the design of electrowetting lenses, the difference in refractive index is maximized, while the densities are matched [45]. A large difference in the refractive indices $n_1 - n_2$ would also be beneficial for continuous fast focal length switching if a large optical power range is desired.

5.2 Wavefront Correction

Oscillations on the meniscus of axis-symmetric liquid lenses can be used for on-demand axis-symmetric wavefront correction. Strauch et al. showed in 2018 [61] that a voltage pulse can excite user-defined axis-symmetric meniscus shapes for momentary phase change on the propagating optical beam. The principles of the approach in [61] will be explained here, as well as the conclusions from the results.

Given a desired meniscus deflection $\eta_c(r,t)$, The Bessel function components of the profile $\eta_c(r,t)$ can be found by taking the zeroth order Hankel transform $H_0\{\eta_c\}$ [87, 61]. If we assume that an applied voltage excites oscillations on an electrowetting lens with meniscus radius R, modeled by $\eta(r,t) = A\cos(2\pi f_f t)J_0(2\pi f_f r/c)$, the Hankel transform $H_0\{\eta_c\}$ can be related to a voltage spectrum needed to produce the desired deflection by [61]

$$U(f) \sim \left(\frac{2\pi f}{c}\right)^2 J_1\left(\frac{2\pi f R}{c}\right) H_0(\eta_c). \tag{5.6}$$

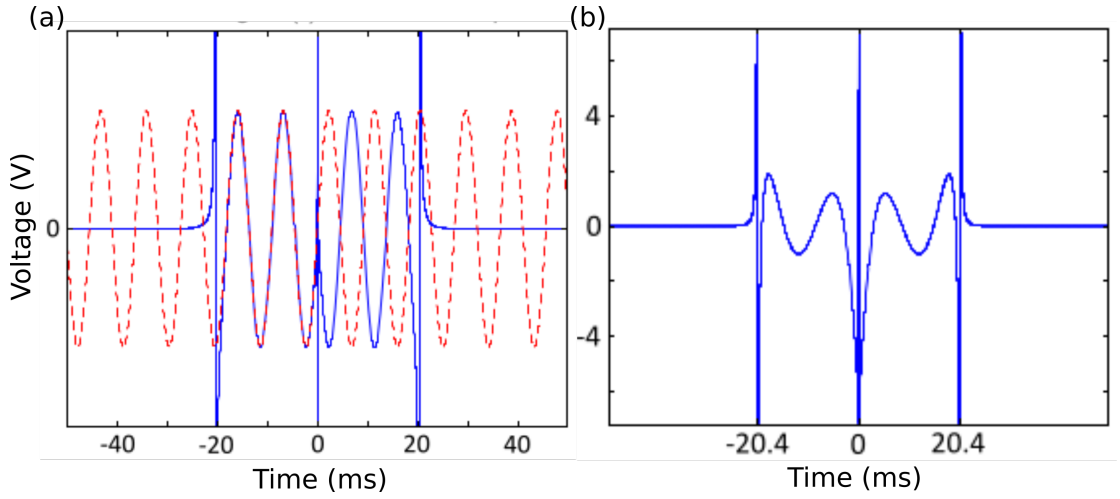

Figure 5.2: Voltage pulses centered at time $t = 0$ that create (a) a single Bessel function mode at time $t = 0$, and (b) Zernike mode Z_4^0 at $t = 0$. From [61] with permission, licensed under a Creative Commons Attribution (CC BY) license.

The time domain voltage signal can then be found by taking the continuous inverse Fourier transform

$$U(t) = \int_{-\infty}^{\infty} U(f) \exp(i2\pi ft) df. \tag{5.7}$$

This produces the desired profile η_c at the time $t = 0$. An example of a voltage pulse given in [61] to excite the second Bessel function mode is shown in Figure 5.2(a), and an example pulse to excite a Zernike Z_4^0 mode is shown in Figure 5.2(b). The negative time portion of the pulses shown in Figure 5.2 creates deflection on the meniscus profile. The profile only has the desired shape at time $t = 0$. The positive time portion of the pulses shown in Figure 5.2 reduces the deflection of the meniscus back to a flat profile, canceling the excited shape from the negative time pulse portion.

The instantaneous profile, both predicted and measured for the Zernike mode that was excited with the pulses shown in Figure 5.2(b). The predicted and measured instantaneous profile for an axicon shape and a square wave shape are shown in Figure 5.3(b) and Figure 5.3(c), respectively. The excitation of the Zernike Z_4^0 mode shape and the axicon shape produced a measured liquid meniscus profile that matched the desired shape down to less than $0.5\mu m$. The square wave, or top-hat shape, shown in Figure 5.3(c), was less successful

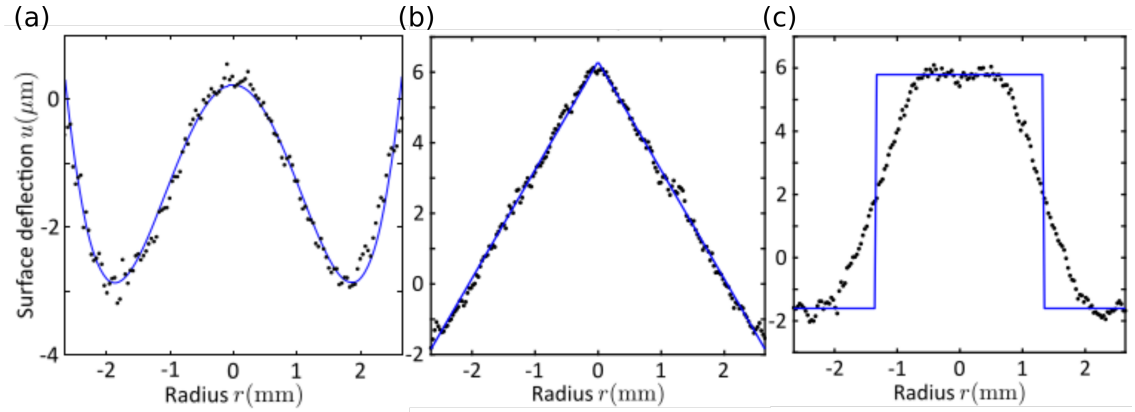

Figure 5.3: Cross-sectional plots of predicted and measured meniscus displacement for a created (a) Zernike Z_4^0 mode, (b) axicon, and (c) square pulse using equations 5.6 and 5.7. From [61] with permission, licensed under a Creative Commons Attribution (CC BY) license.

due to the required high frequency components needed for the creation [61].

In future work on the creation of user-defined profiles for wavefront correction, the excitation of higher frequency components will help produce a greater variety of shapes. A fundamental limit of the Corning commercial electrowetting lenses [47] is that they produce predictable oscillations at frequencies lower than 1kHz. If a lens was designed to support higher frequency oscillations, it would potentially be a candidate for more diverse meniscus deflection creation using voltage pulses. Another limitation that might need to be addressed is the ineffective predictions from the single term Bessel function model for oscillations at frequencies greater than the resonance frequency. If the discrete Hankel transform for mode shapes is used to inform the voltage spectrum in Equation 5.6, a more accurate result might be achieved.

Electrowetting lenses with one outer electrode can potentially correct any wavefront composed of Zernike Z_0^0, Z_2^0, Z_4^0 modes [1]. The Z_2^0 mode can be generated with the same method as the Z_4^0 mode, shown in Figure 5.3. An electrowetting lens with an additional two side chambers for Zernike Z_0^0 (piston) adjustment was recently demonstrated [89]. A lens with this design gives the possibility of piston correction without moving the liquid lens position.

Lenses with multiple electrodes arranged outside of the liquids could potentially be used for producing profiles with axis-asymmetry. Lenses with multiple electrodes have been used experimentally [90] and simulated [50] to produce quasi-static meniscus shapes for wavefront correction. Figure 5.4(a) shows the design from [90], with 8 electrode segments arranged around the liquid-liquid cell. Oscillations created from designs like the one shown in Figure 5.4(a) would add degrees of freedom to the creation of user-defined meniscus profiles, theoretically producing any shape on the meniscus. This is limited, of course, by the maximum allowable slope of the liquids, which is related to the surface tension between the liquids γ_{LL} [49]. To illustrate the change in the oscillation modes as electrodes are added, Figure 5.4(b) shows a plot of modes from uni-direction excitation (top), and two-direction excitation (bottom). The oscillation modes for two-direction excitation were previously found for liquid sloshing surrounded by air [58], and the shape is expected to be the same for a liquid-liquid interface. The equation for the liquid surface height of mode n when two electrodes are used to excite oscillations would be

$$\eta_n(r, \theta_l, t) = A_n \cos(\omega t) \cos(\theta_l) J_1(\lambda_n r), \tag{5.8}$$

where λ_n is the eigenfrequency, θ_l is the angle in the plane of the meniscus, r is the radial distance from the center axis (in and out of the page in Figure 5.4), A_n is the amplitude, and t is time.

If modes shapes similar to the ones shown in Figure 5.4 are excited and combined in superposition, more Zernike modes can be produced for wavefront correction. Zernike modes Z_1^{-1}, Z_1^1, Z_3^{-1}, Z_3^1, Z_5^{-1}, and Z_5^1 are all possible with combinations of the modes shapes from Equation 5.8 [1]. If more electrodes are added, such as with the design in Figure 5.4, the full set of Zernike modes could be achieved, allowing for correction of any form of aberrations.

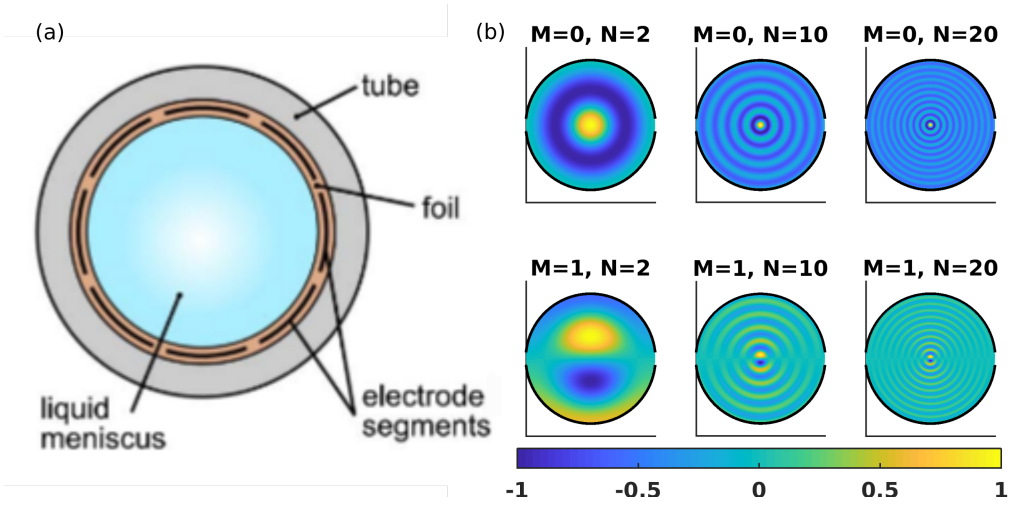

Figure 5.4: (a) the design of a multiple electrode liquid lens, from [90] with permission. (b) The axis-symmetric (top) and asymmetric (bottom) liquid sloshing modes for a cylindrical container, corresponding the the oscillation patterns from single electrode and two-electrode liquid lens systems. (a) is reprinted with permission from [90], Optical Society of America (OSA).

Chapter 6

OPTICAL IMAGE CRYPTOGRAPHY WITH LIQUID LENSES

This chapter covers a recently developed application of electrowetting liquid lens oscillations: time-dependent optical image encryption. This was first introduced by the author in [8] as a potential method to protect optical image encryption systems from adversarial attacks. In this chapter, oscillations in a cylindrical lens are used for the encryption and decryption model. Numerical experiments presented in [8] are also presented here to address initial security considerations, as well as practical recording concerns.

6.1 Motivation and Background

Optical applications that require secure transfer of information contained in images are potential applications for optical image cryptography. Some security systems are optical by nature, such as bar code (intensity image) verification or eye scan verification [44, 91]. Remote sensing of sensitive scenes may require encryption during measurement, instead of after the images have been recorded [92]. Future optical communications may make use of spatial beam phase modulation more and more to carry a higher information density [93]. All of these current and future applications use the advantages of optics, and can gain from fast and secure encryption at the optical layer.

The use of optical processes for encryption allows for alteration of polarization, phase, and intensity for encoding [92]; even bit entanglement is possible [94, 95]. Mathematical transforms, such as the Fourier transform, can be performed on wave-fields at the speed of light for near instantaneous encoding of images. Optical cryptography continues to evolve toward quicker, safer transfer of information.

In general, optical image cryptography systems take, as input, a binary, grayscale, or color images, and transform them into noisy images without distinguishable features. Optical image cryptography systems must then, be able to do this in reverse, which is the say

take these noisy images and transform them back into distinguishable images containing the plaintext. A diagram of this process is shown in Figure 6.1.

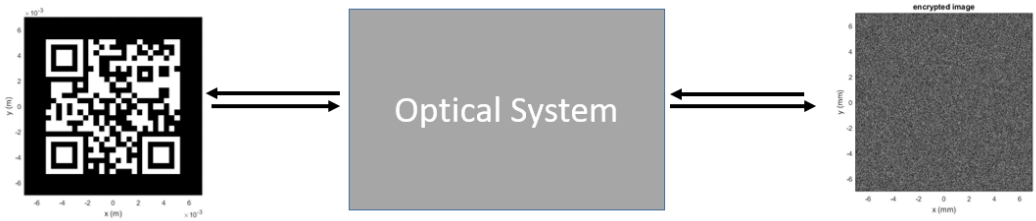

Figure 6.1: Diagram showing concept of optical encryption; in this case encryption of a quick response (QR) code.

Random phase mask encryption is an extensively studied optical cryptography technique that uses optical Fourier transforms to encode wave-fields. Although one of the simplest, the double random phase encryption (DRPE) system, has been shown to be formidable against brute force attacks [96, 97]. In the DRPE, two random phase masks constitute the keyspace of a DRPE system, with one phase mask placed between two lenses in the Fourier plane.

Many additions and modifications have been suggested for the DRPE. These adaptations have sought to increase complexity in the keyspace for added security and to provide different designs more suitable for certain application. One variant of the DRPE is the lens-less Fresnel transform system [98]. Another design uses the placement of random phase elements in the fractional Fourier domains [99, 100, 101, 102, 103], creating a system mathematically similar to the Fresnel transforming system [98].

While more recently proposed optical encryption/decryption systems such as the iterative phase-retrieval encryption system, photon counting optical encryption, and phase truncated optical encryption [104, 105, 106, 107, 108] show promise as more secure systems with larger keyspaces than the DRPE, they do not possess the same simplicity of implementation. The use of specialty equipment in photon counting and phase truncation make these methods more expensive and inflexible for implementation. The iterative phase-retrieval encryption system is an effective design, but requires a mechanical stage to move in increments

during recording. The DRPE is still a simple design choice for optical encryption, and a useful system to study when researching new methods to solve security concerns found in most optical encryption systems.

The DRPE can be exploited by chosen-plaintext and known-plaintext attacks, and in certain circumstances by ciphertext-only attacks. A chosen-plaintext attack on the DRPE can be performed with a point light source plaintext image as an approximate spatial Dirac delta function, yielding the impulse response of the system in the resulting encrypted image. This type of attack may be too suspicious for security systems if only one chosen plaintext image is used. Ciphertext-only attacks take advantage of purely phase modulation in the Fourier plane to retrieve the phase mask keys from a captured encrypted image. Given only one encrypted image, this attack has been successfully demonstrated for plaintext images with less than 1/4 of the pixels containing non-zero values [109]. This pixel limitation, however, may change with multiple encrypted images available to the adversary [109]. When multiple plaintext-encrypted image pairs from a DRPE system fall into the hands of an adversary, the phase mask keys can also be recovered by a known-plaintext attack [110, 111]. If the image intensity is the plaintext, the system is vulnerable to a known-plaintext attack using a single or multiple binary intensity images. If the plaintext is a phase image, constituting what is herein called fully-phase DRPE, the system is vulnerable with multiple pairs of binary phase images [111]. While potentially requiring multiple images or pairs of images, known-plaintext and ciphertext-only attacks may be less recognizable by system security than the single image chosen-plaintext attack. Table 6.1 is given below to summarize the vulnerabilities of the DRPE.

A solution to address multiple image or image pair attack vulnerabilities is to have the optical transfer function of a DRPE system change over time or periodically between uses [110]. Most experimental DRPE systems use spatial light modulators (SLMs), which are spatially discrete by nature, relatively expensive, and polarization sensitive. To change the transfer function between consecutive attacks, an SLM would consistently need to be refreshed with a new random phase grid. An alternative approach would be to change the transfer function of the system over time by adding a thin liquid system with a controllable surface topology. With the use of a liquid system, random phase mask encryption can

Table 6.1: Security conclusions based on simulations of known-plaintext attacks on DRPE systems [110, 111].

Plaintext Image	No. of Image Pairs	Intensity DRPE	Fully-Phase DRPE
Binary	One	Vulnerable	Resistant
Binary	Multiple	Vulnerable	Vulnerable
Multivalued	One	Resistant	Resistant
Multivalued	Multiple	Resistant	Resistant

use fixed, static phase masks (non-SLM phase masks) without the need to change, while the system can have a time-dependent transfer function by the user-defined liquid surface. A time-changing liquid surface, augmenting the use of random phase masks, can prevent adversarial attacks that depend on multiple ciphertext images or plaintext-ciphertext image pairs.

As demonstrated in Chapter 4 of this document, commercially available electrowetting lenses driven by sinusoidal voltages have been shown to exhibit predictable, low amplitude axis symmetric surface wave patterns that match with a Bessel function mathematical model [60, 61]. Surface waves on the meniscus of an electrowetting lens contain information regarding fluid properties, geometry, and the forcing function [60, 61].

A numerical study on the security of using a liquid system with two random phase masks for image encryption/decryption is presented. Low amplitude ($< \mu$m), axis symmetric and asymmetric oscillating liquid surface patterns, in combination with random phase masks, for optical encryption and decryption are used. A simple liquid lens design, such as the one shown in Figure 1 of Chapter 2 is used. Even though many variations of random phase mask encryption exist [100, 112, 101, 103, 98, 113, 114, 107, 106], the integration of a liquid system with a phase-only two random phase mask encryption system is first explored, with one mask in the object plane and one in the Fourier plane. Due to the similarity of the two random phase mask system with many of the more recently proposed optical encryption systems, subsequent studies can be performed using different combinations of random phase masks, lenses, and other optical systems. Only one oscillating liquid system is used in this

study to focus on changing the transfer function over time for the prevention of multiple image or image pair adversarial attacks.

6.2 A liquid lens double random phase mask crypto-system

A simple and practical placement of the liquid system for optical encryption is used. The liquid system can be placed after the plaintext image and first phase mask, but before the first lens in the system. Another option is to use the liquid system both as the first lens and as the time-dependent phase modulating mechanism, as shown in Figure 6.2. This choice reduces the amount of optical elements in the system, and enables a simpler expression for the encrypted image using Fresnel approximations. Placing the liquid system between the two random phase masks ensures concealment of the liquid surface behavior in the encrypted image.

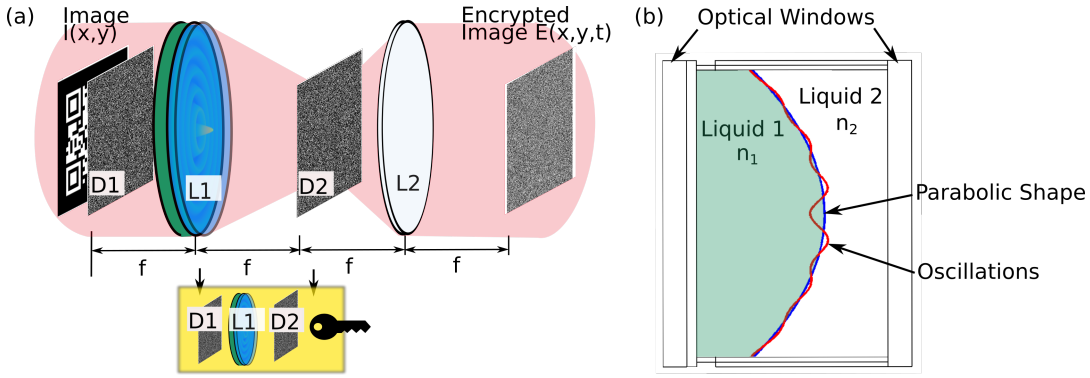

Figure 6.2: (a) A modified double random phase mask encryption system with a tunable liquid lens. The liquid system has an oscillating convex surface, making it also the first lens L1. The red area is the light propagating through the system, while the yellow boxed area contains the keys. The system includes lens L2, and phase masks D1 and D2. (b) The liquid system used for this study, with two immiscible liquids of differing refractive indices n_1 and n_2. From [8].

The liquid system is assumed to be a simple two-liquid lens geometry: two immiscible liquids, enclosed by optical windows and a cylindrical dielectric side-wall, as shown in Figure 6.2(b), and as introduced in Chapter 2. While the thickness of the liquid system remains constant, the meniscus profile between the two liquids can change over time. To model the

thickness of the first liquid in the (x, y) plane, we use the equation [8]

$$\Delta_l = w - \frac{x^2 + y^2}{2R} + \eta(x, y, t) \tag{6.1}$$

where w is the nominal width of the first liquid, R is the radius of curvature, and $\eta(x, y, t)$ is the height of the liquid relative to the static parabolic shape. With the radius of curvature set as the focal length of a $4f$ system ($R = f$), and the refractive indices of the two liquids given as n_1 and n_2, the transmission function is given as [2, 8]

$$t_l(x, y, t) = \exp(jk\phi_w) \exp[jk\eta(n_1 - n_2)] \exp\left[-jk(n_1 - n_2)\frac{x^2 + y^2}{2R}\right] \tag{6.2}$$

where wavenumber $k = 2\pi/\lambda$ with optical wavelength λ, and the constant phase retardation due to the nominal thickness of the liquids and the optical windows is ϕ_w. The notation $\exp(.)$ represents an exponential function.

Standing wave oscillations on a cylindrical lens, as described in Chapter 2, is used. For a maximum phase shift of ϕ_w, an amplitude of $A = \lambda/[2(n_1 - n_2)]$ for all modes n is assumed. The equation for the liquid surface height is

$$\eta_n m(r, \theta_l, t) = A\cos(\omega t)\cos(m\theta_l)J_m(\lambda_n r) \tag{6.3}$$

where $m = 0$ gives axis-symmetric oscillations, such as those measured in Chapter 4, and $m = 1$ gives asymmetric oscillations. This equation for surface height was derived for liquid sloshing modes in open air tanks [58], and it is used here to give the general shape that can be expected from meniscus oscillations in electrowetting lenses.

In this study, the encryption and decryption of a phase image is performed through monochromatic, coherent light. the plaintext $P(x, y) \in \{0, 1\}$ is stored in the phase of an intensity image $I(x, y) = \exp[j2\phi_w P(x, y)]$ which is attached to a 16-bit phase mask $D_1(x, y) = \exp[j\phi_{DP1}(x, y)]$ with phase altering values $\phi_{DP1}(x, y) \in \{0, \ldots, 2\pi\}$ from a uniform distribution. The (x, y) coordinates given here are in the direction of the object plane and image planes, while the perpendicular z direction is the direction of propagation in the $4f$ system. The complex Fourier distribution from the image, first phase mask, and liquid lens, according to the Fresnel diffraction approximation, is modeled as [2]

$$U(x_f, y_f, t) = \frac{1}{j\lambda f} \exp\left[\frac{jk(n_1 - n_2)}{2f}(x_f^2 + y_f^2)\right] \iint_{-\infty}^{\infty} F(x, y, t) \exp\left[\frac{-jk}{f}(xx_f + yy_f)\right] dx\, dy, \tag{6.4}$$

where the double integral is a two-dimensional Fourier transform modeling the frequency spectrum of the light leaving the lens. The function $F(x, y, t)$ is

$$F(x, y, t) = I(x, y) D_1(x, y) \exp\left[jk\eta(n_1 - n_2)\right]. \tag{6.5}$$

The spatial frequencies of the Fourier plane are $x_f = x/(\lambda f)$ and $y_f = y/(\lambda f)$. The spatial frequency spectrum transmitted to the Fourier plane is [2]

$$S(x_f, y_f, t) = U(x_f, y_f, t) \exp\left[-j\pi\lambda f(x_f^2 + y_f^2)\right]. \tag{6.6}$$

With the canceling of the phase terms in front of the Fourier transform and with neglecting the spatially constant phase terms in front of the integration, the complex field at the Fourier plane becomes

$$S(x_f, y_f, t) = \iint_{-\infty}^{\infty} F(x, y, t) \exp\left[\frac{-jk}{f}(xx_f + yy_f)\right] dx\, dy, \tag{6.7}$$

which is a two-dimensional Fourier transform of the function $F(x, y, t)$, that contains the complex image multiplied by the complex first phase mask, multiplied by the liquid surface height changes. Given the second 16-bit phase mask D_2 in the Fourier plane (x_f, y_f), the complex instantaneous encrypted image is given as

$$E(x, y, t) = \iint_{-\infty}^{\infty} S(x_f, y_f, t) D_2(x_f, y_f) \exp\left[\frac{-jk}{f}(xx_f + yy_f)\right] dx_f\, dy_f. \tag{6.8}$$

Decryption can be performed by undoing the operations on the plaintext image. The recovered image $R(x, y)$ can be found with

$$R(x, y, t) = W(x, y, t) \exp\left[jk\eta^*(x, y, t)(n_1 - n_2)\right] D_4(x, y), \tag{6.9}$$

where

$$W(x, y, t) = \iint_{-\infty}^{\infty} Q(x_f, y_f, t) D_3(x_f, y_f) \exp\left[\frac{jk}{f}(xx_f + yy_f)\right] dx_f\, dy_f, \tag{6.10}$$

and

$$Q(x_f, y_f, t) = \iint_{-\infty}^{\infty} E(x, y, t) \exp\left[\frac{-jk}{f}(x_r x_f + y_r y_f)\right] dx\, dy. \tag{6.11}$$

When phase masks $D_3(x_f, y_f) = D_2^*(x_f, y_f)$ and $D_4(x, y) = D_1^*(x, y)$, and the liquid height is $\eta^*(x, y, t) = -\eta(x, y, t)$, the original image is recovered $R(x, y, t) = I(x, y, t)$.

For decryption to be possible, the liquid surface topology at the time of encryption must be known. The liquid surface component of the keyspace is four-dimensional (3-D space and time). This component is realized by either knowing the liquid excitation input and estimating the liquid surface profile with a sufficiently accurate model, or by estimating the liquid surface profile with measurements performed during encryption. In this document, a simple example of successful decryption with a single oscillating liquid mode is used for encryption at time t_e and $h^*(x, y, t) = -h(x, y, t_e + \pi)$, with a canceling constant phase retardation term $\exp(jk\phi_w)^* = \exp(-jk\phi_w)$.

Modeling the physical characteristics of an optical system yields a different expression for the encrypted image. A complex encrypted image in systems that do not vary over time can be measured using digital interference holography [115, 91], such as the system described in Chapter 3. Photons are collected over a finite exposure time τ from the beam propagating through the liquid-crypto system and a reference beam. To model a physical recording of a liquid-crypto system with the encrypted image changing over time, an adaptation to Equation 6.8 is needed. The integration of the intensity of the complex encrypted image $E(x, y, t)$ and a reference beam $E_{rb}(x, y)$ over the exposure time τ from initial time t_0 can be shown as

$$E_{rc}(x, y, t_0, \tau) = \iint_{t_0}^{t_0+\tau} |E(x, y, t) + E_{rb}(x, y)|^2\, dt. \tag{6.12}$$

The encrypted image and reference beam intensity can be written as a function of pixel number (q, v) in an array of size $Q \times V$. If we discretize with $\Delta t = \tau/K$, with K being the total amount of time steps in one full exposure, we can use a trapezoidal integration method to give

$$E_{rc}(x, y, t_0, K) = \Delta t K E_{rb}(q, v) + \frac{\Delta t}{2} \sum_{k=1}^{K} [E(q, v, t_0 + k\Delta t) + E(q, v, t_0 + (k-1)\Delta t)] \tag{6.13}$$

Two options for decryption are presented. If the exposure time τ is much smaller than the fluctuations of intensity, the exposed image becomes

$$E_{rc}(q, v, t_0, K) \approx |E(q, v, t_0) + E_{rb}(q, v)|^2 \, \Delta t K \tag{6.14}$$

A holographic recording of the encrypted image can yield the phase and amplitude of $E(q, v, t_0)$. If the complex image is recovered, decryption can be performed using Equations 6.9–6.11.

With a larger exposure time τ the recorded compound encrypted image $E_{rc}(q, v, t_0, \tau)$ can be thought of as a summation of encrypted images, each recorded over a sufficiently short duration of time. To illustrate this, Figure 6.3 shows intensity fluctuations in one recorded pixel over a full liquid oscillation period.

As shown in Figure Figure 6.3, the encrypted image of interest $E_s(q, v, t_s + \Delta t)$ can be found by subtracting the unwanted encrypted images from the total recorded intensity E_{rc}, and then using an integration rule to estimate $E_s(q, v, t_s)$ from $E_s(q, v, t_s + \Delta t)$. If the encrypted image of interest is at the beginning of the exposure, this is

$$\Delta t E_s(q, v) \approx E_{rc}(q, v) - \Delta t \sum_{k=1}^{K-1} [E(q, v, t_0 + k\Delta t) + E(q, v, t_0 + (k+1)\Delta t)] \tag{6.15}$$

6.3 Numerical investigation

Numerical simulations of the liquid-crypto system were conducted for different liquid oscillation modes $m = 0, 1$ and $n = 2, 3, ..., 30$. Matlab [116] was used to calculate fast Fourier transforms (FFTs) and element by element multiplication to find the encrypted images and the recovered images. A digital pseudo-random number generator was used to construct the random phase masks. There was some variation in the results, and so simulations were repeated with different randomly generated phase masks to calculate mean and variance values. A focal length of $f = 100$mm, a wavelength of $\lambda = 632.8$nm, an image length of $L = 4$mm were used so that the simulations resembled hypothetical experiments using a He-Ne laser, and so that simulations used a critical Fourier optics sampling number for image matrices 256×256 [117].

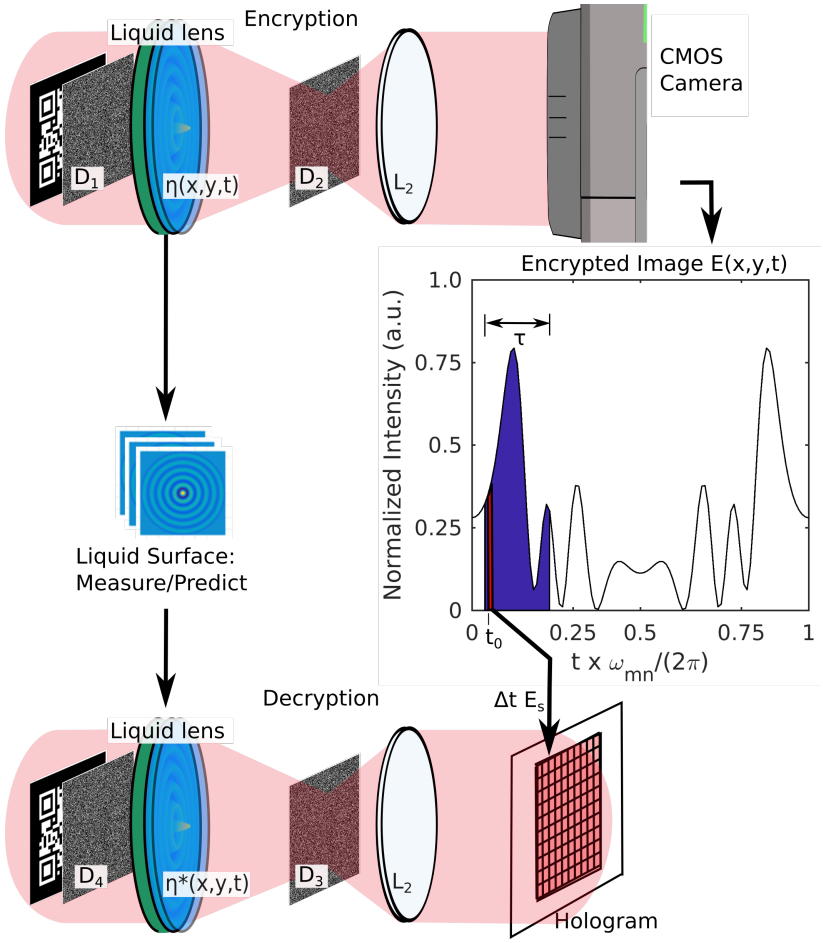

Figure 6.3: The encryption and decryption of a quick response (QR) code at discrete times with an oscillating liquid lens system and two random phase masks. The CMOS camera is shown recording a typical encrypted image intensity, which is shown to the right for a single pixel over time. The blue shaded region in the intensity plot is the recorded encrypted image integrated over exposure time τ while the red region is the intensity of encrypted image of interest E_s that is used for decryption.

An exposure time of 1/2 the liquid oscillation period $\tau = \pi/\omega$ was used in all of the results presented in this document. As shown on the right side of Figure 6.3, the intensity of the encrypted image at each pixel will vary over 1/2 of the liquid oscillation period π/ω. If the image is recorded for a full period $\tau = 2\pi/\omega$, the intensity is doubled. Recording over π/ω enables pixels with little variation over time to increase in intensity at a different rate than pixels without much variation over time, which may give rise to a signature of

the liquid system in the encrypted image. A vulnerability also arises if the exposure time is much smaller than the intensity fluctuations, and multiple plaintext-encrypted image pairs are recorded successively. This would produce a temporal frequency signature that can be traced back to oscillation frequency of the liquid system.

6.3.1 Measure of success for decryption

For comparisons between the phase of a recovered image $R_p(q, v, t)$ with pixels (q, v) in the (x, y) plane and the phase of the original quick response (QR) code image $P(q, v)$, we use a mean squared error (MSE) defined as

$$MSE = \frac{1}{QV} \sum_{q}^{Q} \sum_{v}^{V} |R_p(q, v, t) - P(q, v)|^2 \tag{6.16}$$

To show that the liquid oscillations are an important and irreplaceable part of the keyspace, simulations that used a mismatch of liquid oscillations for encryption and decryption were conducted. A certain liquid oscillation mode $m = 0$, and $n = 2, 3, \ldots, 30$ was used for encryption, and a certain oscillation mode $m = 0$, and $n = 2, 3, \ldots, 30$ was used for decryption, giving a total of 841 possible encryption/decryption combinations. Simulations were repeated 244 times for each combination case so that mean MSE values converged. Simulations that produced encrypted images exposed over half of the oscillation period $\tau = \pi/\omega$ were used for the MSE calculations.

When the conjugate phase masks and conjugate liquid oscillation profile was used for decryption (the same oscillation mode), there was no difference (within machine epsilon) between the recovered image and the plaintext image. When there was a mismatch in the liquid oscillation patterns, there was a signification difference between the recovered images and the plaintext image. Figure 6.4(a) shows the calculated MSE values for each case.

A mismatched liquid surface profile produced significant MSE values in the recovered images, increasing with lower mode number n. For a particular oscillation mode shape used during encryption, a correct match creates a zero MSE value when that same mode shape was used for decryption, as seen in the sharp drops in Figure 6.4(a). From Figure 6.4(a), it can be seen that the MSE ranges from 0.28 to 0.62 when the liquid profile is mismatched for

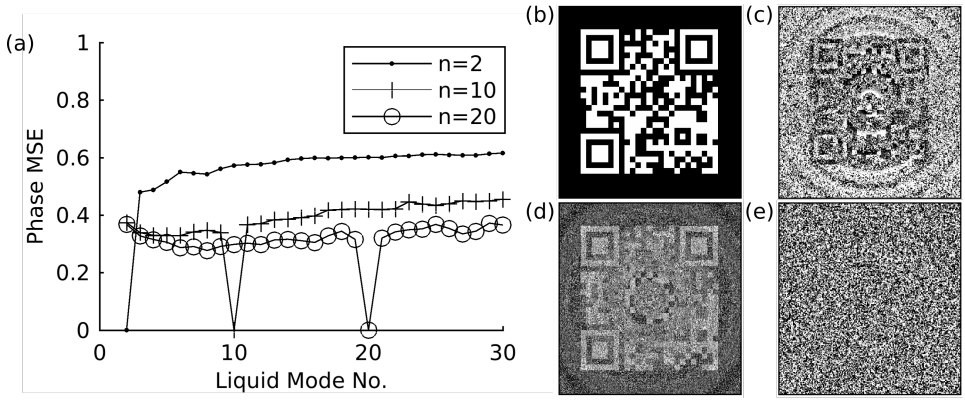

Figure 6.4: (a) The mean squared error (MSE) when comparing the phase of recovered images and the original QR code phase image when different liquid surface mode shapes are used for decryption (Mismatched liquid surfaces). (b) The original QR code used for the simulations. Recovered phase images for (c) a mismatched liquid surface, (d) a mistiming of the liquid system used during decryption of $\tau/10$ and (e) for correct timing but one incorrect random phase mask. From [8].

decryption. This can be compared to $MSE = 0.42$, found when an incorrect random phase mask is used with no liquid system (Figure 6.4(e)). Fig. 6.4(a) shows the max $MSE = 0.37$ for $n = 20$, while the max $MSE = 0.62$ for $n = 2$ used during encryption. The MSE declines with an increase in the liquid mode number used for encryption. It should be noted that although the MSE values from a mismatched liquid surface approach the $MSE = 0.42$ mark for an incorrect random phase mask, and in some cases pass this mark, the recovered images still show signs of an axis symmetric phase element in the system, as shown by the example in Figure 6.4(c). The high MSE values, meaning a significant different in the recovered image from the original image, when a mismatched liquid surface pattern is used for decryption demonstrates the ability of the liquid system to vary the encryption and decryption of images with a tunable surface, even if the same random phase masks are used.

Signification MSE values were also found when the timing of the liquid surface profile was altered during decryption. The MSE between recovered image phase and the original image phase was calculated for a time mismatch of $t_d = \{1/10, 3/10, 1/2\} \cdot 2\pi/\omega$. The MSE values ranged from 0.20 to 0.46, with the largest MSE values coming from low liquid

oscillation mode numbers and mismatch fraction of $t_d = (1/10)2\pi/\omega$. An example is shown in Figure 6.4(d). This study shows the need for precision in the user's estimation of the liquid surface profile over time. A time mismatch contribution to high MSE values further shows the difficulty an adversary would have in estimating an unknown liquid surface profile.

6.3.2 Recording Considerations

The fringe stability requirements when choosing the exposure time for the encrypted image must be addressed. Considering the dynamics of the proposed system, a reference beam interferometry technique, like the one presented in Chapter 2 and Chapter 3, can be used for recording [81]. Typically, an optical path variation of 1/4 to 1/10 of the wavelength λ should not be exceeded during exposure [81]. Variations that exceed this amount will give too great of a shift in the fringes. The greatest liquid height change for the axis symmetric cylindrical oscillations over time is at the center $r = 0$. This means that if an amplitude of $A = \lambda/(2(n_1 - n_2))$ is used, there needs to be

$$\frac{\lambda}{2}|\cos(\omega(\tau + t_0)) - \cos(\omega t_0)| \leq \frac{\lambda}{10} \tag{6.17}$$

If the exposure time is selected so that this is always true, the exposure time should be approximately $\tau \leq 1/(5\omega)$. The simulations in this document that use $\tau = \pi/\omega$ are a conservative scenario for security considerations, but not a practical scenario. If electrowetting lenses are used, with oscillations from 50 –1000 Hz, an exposure time less than 0.6 ms – 0.03 ms should be used. From the author's experience, this is well within the capabilities of most industrial cameras.

In addition to evaluating the security of a liquid system double random phase mask encryption method, we also estimate the expected contributions of a liquid system to the noise in recovered images. An often cited disadvantage of double random phase encryption is the noise found in the recovered images [115, 118]. To understand the contribution of noise by the liquid system, we add noise to the encrypted image and error to the model of the liquid surface patterns over time. An expected amount of noise in a recovered image given additive Gaussian error for the encrypted image was formulated by Javidi et al. [115]. However, to model noise from the liquid system, we add error before the first Fourier

transforms in Equation 6.8 and after the inverse Fourier transforms to recover an image (Equation 6.9). Therefore we use numerical simulations to test the random process in order to understand the expected amount of noise in the recovered image.

We use a modified model for the height of the liquid oscillations $\eta_e(x, y, t)$, which for the amplitude error is

$$\eta_e(x, y, t) = \eta(x, y, t)(1 + \chi), \tag{6.18}$$

and for the horizontal positioning error is

$$\eta_e(x, y, t) = \eta(x, y - \delta, t). \tag{6.19}$$

Gaussian noise is added to the encrypted image phase, giving a modified encrypted image of

$$E_e(x, y, t) = E(x, y, t) \exp\left[j\gamma(x, y)\right] \tag{6.20}$$

the amplitude error χ, horizontal error δ, and encrypted image noise γ are centered at zero and have standard deviations σ_χ,σ_δ,σ_γ, respectively. A mean MSE for recovered images from multiple simulations is non-zero, because the amplitude and horizontal position error are present during both the encryption and decryption.

Simulations were conducted to estimate how much error in recovered images can be expected from additive noise in the encrypted image and error in the positioning or modeling of the liquid system. A Gaussian distribution with a standard deviation of $\sigma_\chi = \{10, 50, 100\}\%$ was used to model error in the estimation of the liquid oscillation amplitude. With an amplitude tuned to provide a π phase shift, the oscillation height is $max\{\eta(x, y, t)\} = 2.611$ μm. Similarly, a Gaussian distribution to model horizontal position error a standard deviation of $\sigma_\delta = \{4, 8, 12\}$ pixels was used. In this study, this corresponds to a physical shift standard deviation of $\sigma_\delta = \{72, 144, 216\}$ μm. Gaussian noise with a standard deviation of $\sigma_\gamma = \{\pi/10, \ldots, \pi\}$ radians was added to the phase of encrypted images at an instant of time for each simulation. Numerical simulations were performed 100 times for each error case. The mean MSE of recovered images with oscillation amplitude error and horizontal position error are shown in Figure 6.5(a) and Figure 6.5(b), respectively.

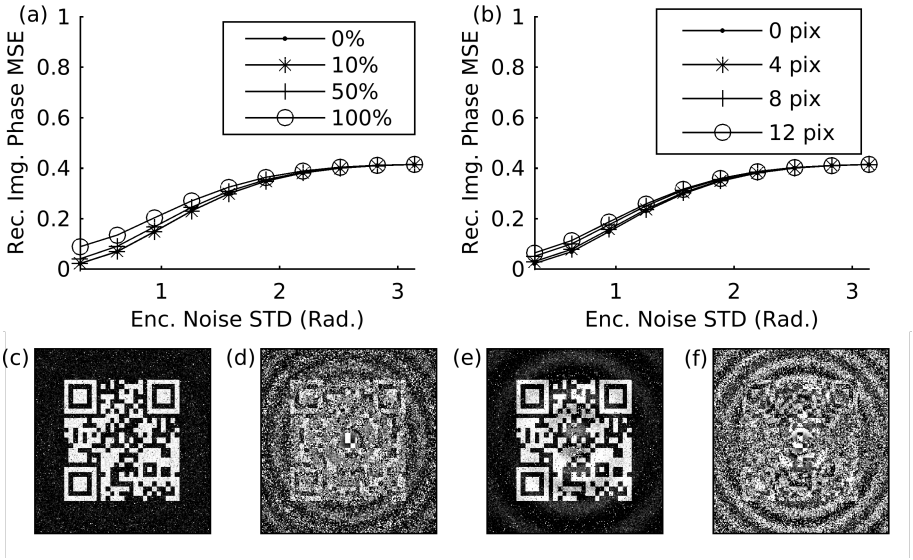

Figure 6.5: (a)–(b) The mean squared error (MSE) when comparing the phase of recovered images and the original QR code phase image when noise is added to the encrypted image phase and there is error with varying standard deviation in the (a) amplitude of the liquid oscillations or (b) the horizontal positioning of the liquid system. Recovered phase images with Gaussian error in the encrypted image $\sigma_\gamma = \pi/10$, and amplitude error $\chi = 0.05$ for (c) an instantaneous encryption and (d) exposed encryption. Recovered phase images with Gaussian error in the encrypted image $\sigma_\gamma = \pi/10$, and horizontal position error $\delta = 4$pixels for (e) instantaneous encryption and (f) exposed encryption. From [8].

The error in recovered images increases when encryption is performed over an increasing time duration. This is intuitive, as accurate estimation of the liquid oscillation amplitude and horizontal position is needed to extract an encrypted image at an instant of time from an exposed encrypted image. A comparison between recovered images when the encryption is instantaneous and when it is exposed over half of the oscillation period $\tau = \pi/\omega$ shown in Figure 6.5(c)–Figure 6.5(f), with Figure 6.5(c) and Figure 6.5(e) coming from instantaneous encryption. The longer the encrypted image is exposed, the more error will be found in the recovered image.

6.3.3 Security Considerations

Evaluation of the security of a scheme is an ongoing task with lack of a mathematical proof that the encryption problem is hard to solve. For this reason, researchers considering new a new optical security scheme with mathematical complexity will evaluate numerically or experimentally found encrypted images, and calculate the information entropy. The information entropy is a quantitative measure of the randomness of an image. The entropy of an image can be calculated by summing bins for intensity of phase into a histogram. For a histogram with N_b bins, the numerical calculation of entropy is

$$Entropy = \sum_{i=1}^{N_b} p(\alpha_i) log_2 p(\alpha_i), \tag{6.21}$$

where $p(\alpha_i)$ is the normalized histogram count of bin i. An image with maximum entropy with yield an entropy calculation of 8 when using 256 bins. This is reached with a phase-only random phase mask system without a liquid system present [115, 91].

The mean entropy values for encrypted images at an instant of time were different for the intensity and phase of the simulated encrypted images, as shown in Figure 6.6. The phase of encrypted images was consistently at the maximum of 8 (to three significant digits) for both axis symmetric $m = 0$ and asymmetric $m = 1$ surface patterns. This is consistent with the entropy of the phase without the liquid system, which corresponds to documented DRPE systems [115]. The liquid surface changes the phase of the wavefront at an instant of time after it has already been changed by random amounts by the first phase mask, which makes the liquid phase change not deleterious to the entropy of encrypted image phase.

The entropy of the intensity of encrypted images was higher with an exposure time of half of the liquid oscillation period $\tau = \pi/\omega$ than it was at an instant, as shown in Figure 6.6. The entropy at an instant of time is consistently at 5.93 for all mode numbers of axis symmetric and asymmetric liquid surface shapes. The entropy of the exposed images, however, shows an inverse relationship with increasing mode number n, as seen in Figure 6.6(a). This may be related to the relationship between the ratio of mean liquid wavelength over phase mask pixel width $\lambda_f/\Delta x$, which is an inverse relationship over liquid mode number n. This ratio is plotted for $n = 2 - n = 30$ in Figure 6.7. Though this relationship points to the possibility

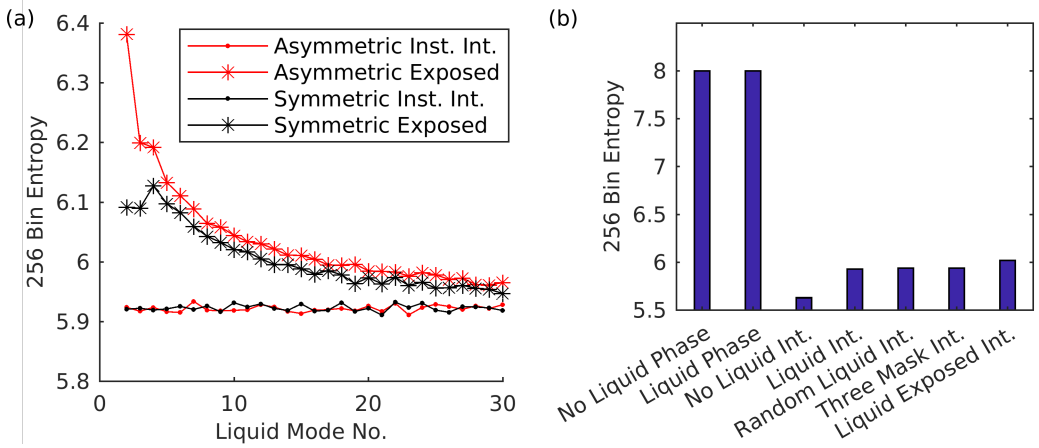

Figure 6.6: Entropy of phase and intensity (int.) of encrypted images for axis symmetric and asymmetric liquid surface mode shapes of mode number n. Encrypted images taken at an instant of time $t = 0$ (inst.) and exposed over a full liquid surface oscillation period $\tau = \pi/\omega$ (exposed) were used. From [8].

of an adversary using the entropy of the intensity to guess the liquid profile, it should be noted that given only a few encrypted images, the entropy is statistically not a reliable indicator of what the liquid mode number is, or whether the liquid profile is axis symmetric or not. Though information should be contained in the phase of the encrypted image, it would be of note if the entropy of the intensity of encrypted images was lower when a liquid system is used.

To measure how much encrypted images from the liquid-crypto system correlate to the liquid pattern used for encryption, we compare phase and intensity values across the midsection of the pattern/image. The midsection of the liquid surface pattern with a length L at $t = 0$ is defined as $u(x = L/2, y)$, while the midsection of the encrypted image is defined as $v(x = L/2, y)$. these two data series are taken from the pixels along a line through the center of the two images, as shown by arrows in Figure 6.8. We use the correlation coefficient ρ_c for the comparison. The correlation coefficient can be calculated by [93]

$$\rho_c = \frac{C_{uv}}{\sigma_u \sigma_v}, \tag{6.22}$$

with C_{uv} being the covariance of the two data series u and v, while σ_u and σ_v are the square

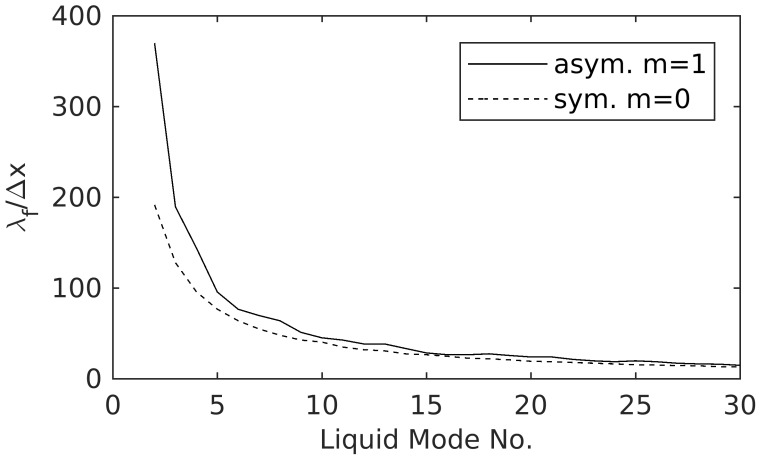

Figure 6.7: The ratio of the mean wavelength of the liquid oscillations λ_f to the width of the phase mask pixels Δx

root of the variance of u and v, respectively.

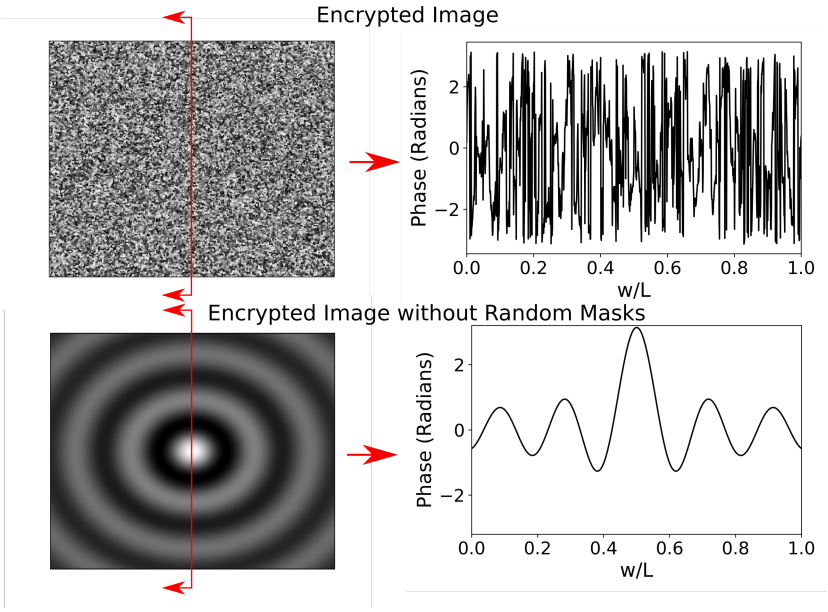

Figure 6.8: The phase values at the centerline of (top) an encrypted image using the liquid system and the random phase masks, and (bottom) the relevant liquid profile. A correlation coefficient is calculated using these two data series for each liquid surface mode number n. From [8].

The mean correlation coefficient between encrypted images and the liquid surface mode pattern was near zero, with a variance that increased when one of the random phase masks wasn't used. As shown in Figure 6.8, the phase values from the mid-line of the axis symmetric ($m = 0$) liquid surface pattern and QR code, and the instantaneous encrypted image were taken as two data series and compared. An encrypted image resulting from each liquid surface mode shape was compared with the corresponding liquid mode shape. The mean correlation coefficient when one or both of the random phase masks was used was on the order of 10^{-3}. When no random phase masks were used, the mean correlation coefficient ranged from +0.53 to -0.28, as shown in Figure 6.9(a). This is to be expected, as the resulting image is just the QR code multiplied pixel by pixel with the liquid surface profile. The variance was below 10^{-2} when both random phase masks were used. However, when only one of the random phase masks was used, the variance was 2–10x higher (phase) and showed an inverse relationship with increasing liquid mode number n, as shown in Figure 6.9(b). This could be due to the frequencies of the liquid surface profile not being completely concealed by the second random phase mask when it is absent. Although the lack of a statistically meaningful correlation coefficient when the liquid system and both random phase masks are used does not prove there is no correlation between encrypted images and the relevant liquid surface profiles [93], it does provide a strong case for there being no easily found relationship.

6.4 Conclusions and Future Work

An oscillating liquid lens system that modulates phase over time can be used to add a tunable and time-dependent element to a double random phase mask system. This can potentially be used to reduce vulnerability to multi-image known-plaintext and ciphertext-only attacks. The necessary assumption of an unchanging first phase mask in multiple image attacks will no longer be valid in a system with a time-dependent first lens. In order to use a liquid system as a phase modulating encryption device, the liquid system must be either predictable or measurable during encryption and decryption. During encryption, if the encrypted image is recorded over a sufficiently short period of time, the encrypted image can be directly decrypted by undoing the operations done during encryption. With a

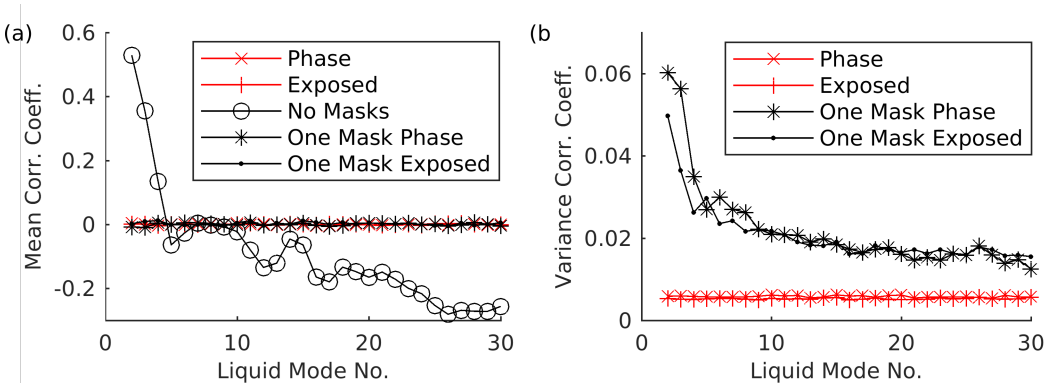

Figure 6.9: The (a) mean and (b) variance of the correlation coefficient for $n = 2, 3, \ldots, 30$, calculated between centerlines of recovered phase images and the original plaintext phase image. Both the liquid system and the two random phase masks were used for the data series "Phase" and "Exposed", while only one random phase mask was used for data series labeled "One Mask". No random phase masks were used for series "No Masks". From [8].

longer encryption exposure time, the encrypted image can be extracted from the recorded encrypted image by subtraction. We found no significant correlation between the liquid system patterns and the resulting encrypted images, and the entropy of encrypted images did not decrease with the use of a liquid system. Simulations showed that entropy of the phase of instantaneous encrypted images is at a maximum, the same as with a traditional phase-only DRPE. The entropy of the intensity of an instantaneous and exposed encrypted images is slightly higher (0.30 to 0.31) than that found using a traditional phase-only DRPE (Figure 6.6), and increases with the use of multiple liquid mode numbers forced at once. It was found that the mean correlation coefficient is near zero between the liquid profiles and the encrypted images. The variance in the correlation coefficient between simulations is less than 0.01. However, when one of the random phase masks is removed, we found the variance to increase to levels between 0.06 and 0.01. The liquid system, in combination with two random phase masks gives way to no statistically significant correlation with the encrypted images.

The tunable and time-dependent nature of the liquid surface can add noise to the recovered image, but may not be as significant as error in the encrypted image from the other optics. A reasonable error in oscillation amplitude of 131 nm, and horizontal positioning of

72 μm does not make the image unrecoverable, even when simulated with additive Gaussian noise in the phase of the encrypted image with a standard deviation of $\sigma_\gamma = \pi/10$. This shows the feasibility of implementing an oscillating liquid surface in a double random phase mask system.

An incorrect liquid surface profile mode number, or mistiming significantly alters the recovered image. The mean squared error (MSE) between the recovered image and the original image was shown to be between 0.28 to 0.62 when the liquid was mismatched during decryption. Mismatching of the liquid during decryption gave MSE values from 0.20 to 0.46. This demonstrates the tunable and time-dependent, yet significant, change in encryption/decryption produced by a dynamic liquid lens system. This tunable, time-dependent change in the system transfer function may be used to also prevent single image known-plaintext attacks. A vulnerability to Dirac delta known-plaintext attacks can be overcome if the second lens in the system (labeled L2 in Figure 6.2) is also a liquid system with the capability of tunable oscillations. An illustration of such a system is given in Figure 6.10. If the lens oscillations have radially random oscillation amplitude, such as the example in Fig. 2b, a physical system similar to the one proposed in Kumar et al. [119] to prevent chosen-plaintext attacks would be realized.

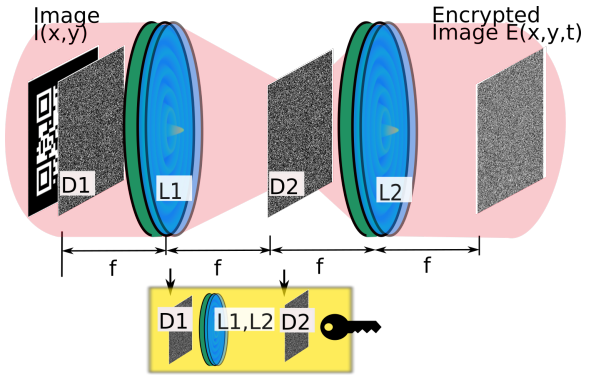

Figure 6.10: The encryption and decryption of a QR code with two oscillating liquid lens systems and two random phase masks. This system is considered to be a solution to the problem of Dirac delta known plaintext attacks.

Future studies will involve experiments and multi-frequency forcing of liquid systems

for randomly varying phase modulation. After generating a random map of liquid surface heights, multi-frequency forcing could then be used to produce the desired heights. An example of a computer generated axis-symmetric random surface profile is shown in Figure 6.11 Further study is needed to determine if multi-frequency forced liquid surface could potentially be used to replace one of the random phase masks in a double random phase mask system. Experiments demonstrating the added security from a dynamic liquid lens are currently being prepared, and should demonstrate for the first time a time-dependent optical image encryption.

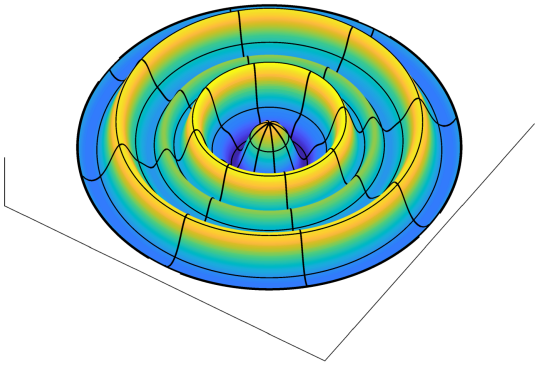

Figure 6.11: A numerically calculated liquid lens meniscus profile with random variation with increasing radial distance r from the center axis.

BIBLIOGRAPHY

[1] Robert K. Tyson. *Principles of adaptive optics*. Boston: Academic Press, 1991. ISBN: 0-12-705900-8.

[2] Joseph W. Goodman. *Introduction to Fourier optics*. 3rd ed. OCLC: ocm56632414. Englewood, Colo: Roberts & Co, 2005. ISBN: 978-0-9747077-2-3.

[3] Frank L Pedrotti, Leno M Pedrotti, and Leno S Pedrotti. *Introduction to optics*. Cambridge University Press, 2017.

[4] Shoufeng Lan et al. "Metasurfaces for near-eye augmented reality". In: *ACS Photonics* (2019).

[5] S. Kuiper and B. H. W. Hendriks. "Variable-focus liquid lens for miniature cameras". en. In: *Applied Physics Letters* 85.7 (Aug. 2004), pp. 1128–1130. ISSN: 0003-6951, 1077-3118. DOI: 10.1063/1.1779954. URL: http://aip.scitation.org/doi/10.1063/1.1779954 (visited on 12/29/2016).

[6] Andrew Maimone, Andreas Georgiou, and Joel S Kollin. "Holographic near-eye displays for virtual and augmented reality". In: *ACM Transactions on Graphics (TOG)* 36.4 (2017), p. 85.

[7] Lidong Wei et al. "Design and fabrication of a compact off-axis see-through head-mounted display using a freeform surface". In: *Optics express* 26.7 (2018), pp. 8550–8565.

[8] David R Schipf and Wei-Chih Wang. "Optical encryption using a liquid phase mask". In: *OSA Continuum* 1.3 (2018), pp. 1026–1040.

[9] Sanghoon Kim et al. "Design and implementation of a low-cost, portable OCT system". In: *Biomedical optics express* 9.3 (2018), pp. 1232–1243.

[10] Kiri Lee et al. “High-speed dual-layer scanning photoacoustic microscopy using focus tunable lens modulation at resonant frequency”. In: *Optics express* 25.22 (2017), pp. 26427–26436.

[11] Hyeonseung Yu et al. “Recent advances in wavefront shaping techniques for biomedical applications”. In: *Current Applied Physics* 15.5 (2015), pp. 632–641.

[12] Yi-Hsin Lin and Hung-Shan Chen. “Electrically tunable-focusing and polarizer-free liquid crystal lenses for ophthalmic applications”. In: *Optics Express* 21.8 (2013), pp. 9428–9436.

[13] Yang Cheng et al. “Reducing defocus aberration of a compound and human hybrid eye using liquid lens”. In: *Applied optics* 57.7 (2018), pp. 1679–1688.

[14] Ireneusz Grulkowski et al. “Swept source optical coherence tomography and tunable lens technology for comprehensive imaging and biometry of the whole eye”. In: *Optica* 5.1 (2018), pp. 52–59.

[15] Max Born and Emil Wolf. *Principles of optics: electromagnetic theory of propagation, interference and diffraction of light*. Elsevier, 2013.

[16] Peng Xiao, Mathias Fink, and A Claude Boccara. “Retinal imaging with adaptive optics full-field OCT”. In: *Optical Coherence Tomography and Coherence Domain Optical Methods in Biomedicine XXI*. Vol. 10053. International Society for Optics and Photonics. 2017, 100530K.

[17] Helge Sudkamp et al. “Simple approach for aberration-corrected OCT imaging of the human retina”. In: *Optics letters* 43.17 (2018), pp. 4224–4227.

[18] Stefano Bonora et al. “Wavefront correction and high-resolution in vivo OCT imaging with an objective integrated multi-actuator adaptive lens”. In: *Optics express* 23.17 (2015), pp. 21931–21941.

[19] Jason D Marsack and Raymond A Applegate. “Corrections in highly aberrated eyes”. In: *Handbook of Visual Optics, Volume Two: Instrumentation and Vision Correction* (2017), p. 203.

[20] Yu-Jen Wang et al. "Augmented reality with image registration, vision correction and sunlight readability via liquid crystal devices". In: *Scientific reports* 7.1 (2017), p. 433.

[21] Haiwei Chen et al. "Beam steering for virtual/augmented reality displays with a cycloidal diffractive waveplate". In: *Optics express* 24.7 (2016), pp. 7287–7298.

[22] FC Wippermann et al. "Bifocal liquid lens zoom objective for mobile phone applications". In: *Sensors, Cameras, and Systems for Scientific/Industrial Applications VIII*. Vol. 6501. International Society for Optics and Photonics. 2007, p. 650109.

[23] Ermanno Borra et al. *Magnetically deformable ferrofluids and mirrors*. US Patent 8,444,280. 2013.

[24] Ermanno F Borra, Anna Ritcey, and Etienne Artigau. "Floating mirrors". In: *The Astrophysical Journal Letters* 516.2 (1999), p. L115.

[25] Denis Brousseau et al. "Modal dynamics of magnetic-liquid deformable mirrors". In: *Applied optics* 53.22 (2014), pp. 4903–4909.

[26] Denis Brousseau, Ermanno F Borra, and Simon Thibault. "Wavefront correction with a 37-actuator ferrofluid deformable mirror". In: *Optics express* 15.26 (2007), pp. 18190–18199.

[27] Phil R Laird et al. "Ferrofluid-based deformable mirrors: a new approach to adaptive optics using liquid mirrors". In: *Adaptive Optical System Technologies II*. Vol. 4839. International Society for Optics and Photonics. 2003, pp. 733–741.

[28] S Thibault, D Brousseau, and EF Borra. "Liquid deformable mirror for advanced sub-optical system testing". In: *Modern Technologies in Space-and Ground-based Telescopes and Instrumentation*. Vol. 7739. International Society for Optics and Photonics. 2010, p. 773910.

[29] Eric S. ten Have and Gleb Vdovin. "Characterization and closed-loop performance of a liquid mirror adaptive optical system". In: *Applied optics* 51.12 (2012), pp. 2155–2163. URL: `http://www.opticsinfobase.org/ao/fulltext.cfm?uri=ao-51-12-2155` (visited on 04/24/2015).

[30] Eric Stephan Ten Have. *Adaptive Optics based on Liquid Total Internal Reflecton Mirrors*. Delft University of Technology (TU Delft), 2014.

[31] Hanyang Huang and Yi Zhao. "Optofluidic lenses for 2D and 3D imaging". In: *Journal of Micromechanics and Microengineering* (2019).

[32] Euan McLeod and Craig B Arnold. "Complex beam sculpting with tunable acoustic gradient index lenses". In: *Complex Light and Optical Forces*. Vol. 6483. International Society for Optics and Photonics. 2007, p. 64830I.

[33] Euan McLeod, Adam B Hopkins, and Craig B Arnold. "Multiscale Bessel beams generated by a tunable acoustic gradient index of refraction lens". In: *Optics letters* 31.21 (2006), pp. 3155–3157.

[34] Alexandre Mermillod-Blondin, Euan McLeod, and Craig B Arnold. "High-speed varifocal imaging with a tunable acoustic gradient index of refraction lens". In: *Optics letters* 33.18 (2008), pp. 2146–2148.

[35] Lifa Hu et al. "Phase-only liquid-crystal spatial light modulator for wave-front correction with high precision". In: *Optics express* 12.26 (2004), pp. 6403–6409.

[36] *Spatial Light Modulators*. URL: `https://holoeye.com/spatial-light-modulators/`.

[37] *Focus tunable lenses*. URL: `https://www.optotune.com/products/focus-tunable-lenses`.

[38] M Blum et al. "Optotune focus tunable lenses and laser speckle reduction based on electroactive polymers". In: *Moems and Miniaturized Systems Xi*. Vol. 8252. International Society for Optics and Photonics. 2012, p. 825207.

[39] Guo-Hua Feng and Jun-Hao Liu. "Simple-structured capillary-force-dominated tunable-focus liquid lens based on the higher-order-harmonic resonance of a piezoelectric ring transducer". In: *Applied optics* 52.4 (2013), pp. 829–837. URL: `https://www.osapublishing.org/abstract.cfm?uri=ao-52-4-829` (visited on 12/29/2016).

[40] Bruno Berge and Jérôme Peseux. "Variable focal lens controlled by an external voltage: An application of electrowetting". In: *The European Physical Journal E* 3.2 (2000), pp. 159–163. URL: http://link.springer.com/article/10.1007/s101890070029 (visited on 12/29/2016).

[41] Bnmo Berge. "Liquid lens technology: principle of electrowetting based lenses and applications to imaging". In: *18th IEEE International Conference on Micro Electro Mechanical Systems, 2005. MEMS 2005.* IEEE, 2005, pp. 227–230. URL: http://ieeexplore.ieee.org/xpls/abs_all.jsp?arnumber=1453908 (visited on 12/29/2016).

[42] Hongwen Ren and Shin-Tson Wu. *Introduction to adaptive lenses*. Vol. 75. John Wiley & Sons, 2012.

[43] Claude Gabay et al. "Dynamic study of a Varioptic variable focal lens". In: *Current Developments in Lens Design and Optical Engineering III*. Vol. 4767. International Society for Optics and Photonics. 2002, pp. 159–166.

[44] Mathieu Maillard, Julien Legrand, and Bruno Berge. "Two liquids wetting and low hysteresis electrowetting on dielectric applications". In: *Langmuir* 25.11 (2009), pp. 6162–6167. URL: http://www.varioptic.com/media/uploads/publication/two_liquids_wetting_and_low_hysteresis.pdf (visited on 12/13/2017).

[45] Alexander M Watson et al. "Ionic liquid-based variable focus electrowetting optics with bandwidths spanning the visible to mid-infrared". In: *arXiv preprint arXiv:1603.00421* (2016).

[46] Alexander M Watson et al. "Focus-tunable low-power electrowetting lenses with thin parylene films". In: *Applied optics* 54.20 (2015), pp. 6224–6229.

[47] *Corning Varioptic Lenses — Driver for Adjustable Lenses*. URL: https://www.corning.com/worldwide/en/innovation/corning-emerging-innovations/corning-varioptic-lenses.html.

[48] Alexander Maxwell Watson. "Electrowetting Variable Optics for Visible and Infrared Applications". In: (2015).

[49] Pierre-Gilles de Gennes, Francoise Brochard-Wyart, and David Quere. *Capillarity and Wetting Phenomena: Drops, Bubbles, Pearls, Waves*. Springer Science & Business Media, 2013.

[50] Mo Zohrabi et al. "Numerical analysis of wavefront aberration correction using multielectrode electrowetting-based devices". In: *Optics express* 25.25 (2017), pp. 31451–31461.

[51] Michael Faraday. "On a Peculiar Class of Aoustical Figures; and on Certain Forms Assumed by Groups of Particles upon Vibrating Elastic Surfaces". In: *Philosophical Transactions of the Royal Society A: Mathematical, Physical and Engineering Sciences* 121 (Jan. 1831), pp. 299–340.

[52] S. Douady. "Experimental study of the Faraday instability". In: *Journal of Fluid Mechanics* 221 (1990), pp. 383–409. URL: `http://journals.cambridge.org/abstract_S0022112090003603` (visited on 07/23/2015).

[53] Antonin Eddi et al. "Information stored in Faraday waves: the origin of a path memory". en. In: *Journal of Fluid Mechanics* 674 (May 2011), pp. 433–463. ISSN: 0022-1120, 1469-7645. DOI: `10.1017/S0022112011000176`. URL: `http://www.journals.cambridge.org/abstract_S0022112011000176` (visited on 02/11/2015).

[54] H. Arbell and J. Fineberg. "Pattern Formation in 2-Frequency Forced Parametric Waves". In: *Physical Review E* 65 (Apr. 2002), p. 036224.

[55] A. M. Rucklidge and M. Silber. "Design of Parametrically Forced Patterns and Quasipatterns". en. In: *SIAM Journal on Applied Dynamical Systems* 8.1 (Jan. 2009), pp. 298–347. ISSN: 1536-0040. DOI: `10.1137/080719066`. URL: `http://epubs.siam.org/doi/abs/10.1137/080719066` (visited on 07/24/2015).

[56] Jeff Porter, Chad Topaz, and Mary Silber. "Pattern Control via Multifrequency Parametric Forcing". en. In: *Physical Review Letters* 93.3 (July 2004). ISSN: 0031-9007, 1079-7114. DOI: `10.1103/PhysRevLett.93.034502`. URL: `http://link.aps.org/doi/10.1103/PhysRevLett.93.034502` (visited on 07/22/2015).

[57] John Miles and Diane Henderson. "Parametrically forced surface waves". In: *Annual Review of Fluid Mechanics* 22.1 (1990), pp. 143–165. URL: `http://www.annualreviews.org/doi/pdf/10.1146/annurev.fl.22.010190.001043` (visited on 02/11/2015).

[58] Raouf A. Ibrahim. *Liquid Sloshing Dynamics: Theory and Applications*. 2nd ed. Cambridge, UK: Cambridge University Press, 2013. ISBN: 978-0-511-12492-1.

[59] Horace Lamb. *Hydrodynamics*. Cambridge university press, 1993.

[60] Matthias Strauch et al. "Study of surface modes on a vibrating electrowetting liquid lens". In: *Applied Physics Letters* 111.17 (2017), p. 171106.

[61] Matthias Strauch et al. "Creation of aspheric interfaces on an electrowetting liquid lens using surface oscillations". In: *AIP Advances* 8.11 (2018), p. 115224.

[62] David R Schipf and Wei-Chih Wang. "Measurement and modeling of Electrowetting Lens Oscillations using Digital Holographic Interferometry and Bessel and Legendre polynomial functions". In: *Optics express* 27.12 (2019).

[63] L. D. Landau and E. M. Lifshitz. *Fluid mechanics*. 2nd ed. 6. Course on Theoretical Physics, v. 6. Amsterdam: Elsevier/Butterworth-Heinemann, 2004. ISBN: 0750627670.

[64] TB Jones. "More about the electromechanics of electrowetting". In: *Mechanics Research Communications* 1.36 (2009), pp. 2–9.

[65] Frieder Mugele and Jean-Christophe Baret. "Electrowetting: from basics to applications". In: *Journal of physics: condensed matter* 17.28 (2005), R705.

[66] Longquan Chen and Elmar Bonaccurso. "Electrowetting—From statics to dynamics". In: *Advances in colloid and interface science* 210 (2014), pp. 2–12.

[67] Shawn W Walker, Benjamin Shapiro, and Ricardo H Nochetto. "Electrowetting with contact line pinning: Computational modeling and comparisons with experiments". In: *Physics of Fluids* 21.10 (2009), p. 102103.

[68] Yi Lu et al. "Dynamics of droplet motion induced by electrowetting". In: *International Journal of Heat and Mass Transfer* 106 (2017), pp. 920–931.

[69] Jung Min Oh, Sung Hee Ko, and Kwan Hyoung Kang. "Analysis of electrowetting-driven spreading of a drop in air". In: *Physics of Fluids* 22.3 (2010), p. 032002.

[70] Philippe Dennery and André Krzywicki. *Mathematics for physicists*. Courier Corporation, 2012.

[71] Helmut F Bauer. "Oscillations of immiscible liquids in a rectangular container: a new damper for excited structures". In: *Journal of Sound and Vibration* 93.1 (1984), pp. 117–133.

[72] YL Sinai. "Fundamental sloshing frequencies of stratified two-fluid systems in closed prismatic tanks". In: *International journal of heat and fluid flow* 6.2 (1985), pp. 142–144.

[73] Helmut F Bauer and Werner Eidel. "Non-linear liquid motion in conical containers". In: *Acta Mechanica* 73.1-4 (1988), pp. 11–31.

[74] Milton Abramowitz and Irene A Stegun. *Handbook of mathematical functions: with formulas, graphs, and mathematical tables*. Vol. 55. Courier Corporation, 1965.

[75] *OpticStudio*. URL: `https://www.zemax.com/products/opticstudio`.

[76] *PDm200B Miniature High Voltage Amplifier*. URL: `https://www.piezodrive.com/modules/pdm200b/`.

[77] *Data Acquisition*. URL: `http://www.ni.com/data-acquisition/`.

[78] Jill E Seebergh and John C Berg. "Dynamic wetting in the low capillary number regime". In: *Chemical Engineering Science* 47.17-18 (1992), pp. 4455–4464.

[79] Š Šikalo et al. "Dynamic contact angle of spreading droplets: Experiments and simulations". In: *Physics of Fluids* 17.6 (2005), p. 062103.

[80] Xie Na, Zhang Ning, and Xu Rong-Qing. "Effect of driving voltage polarity on dynamic response characteristics of electrowetting liquid lens". In: *Japanese Journal of Applied Physics* 57.5 (2018), p. 052201.

[81] Ulf Schnars et al. "Digital holography". In: *Digital Holography and Wavefront Sensing*. Springer, 2015, pp. 39–68.

[82] Gregory R Toker. *Holographic Interferometry: A Mach–Zehnder Approach*. CRC Press, 2016.

[83] Leonard Meirovitch. *Principles and techniques of vibrations*. Vol. 1. Prentice Hall New Jersey, 1997.

[84] Jean Rajchenbach and Didier Clamond. "Faraday waves: their dispersion relation, nature of bifurcation and wavenumber selection revisited". In: *Journal of Fluid Mechanics* 777 (2015).

[85] Thomas Brooke Benjamin and Fritz Joseph Ursell. "The stability of the plane free surface of a liquid in vertical periodic motion". In: *Proceedings of the Royal Society of London. Series A. Mathematical and Physical Sciences* 225.1163 (1954), pp. 505–515.

[86] Doug Binks, Mark-Tiele Westra, and Willem van de Water. "Effect of depth on the pattern formation of Faraday waves". In: *Physical review letters* 79.25 (1997), p. 5010.

[87] Natalie Baddour and Ugo Chouinard. "Theory and operational rules for the discrete Hankel transform". In: *JOSA A* 32.4 (2015), pp. 611–622.

[88] Carlos A López and Amir H Hirsa. "Fast focusing using a pinned-contact oscillating liquid lens". In: *Nature Photonics* 2.10 (2008), p. 610.

[89] Lei Li et al. "Displaceable and focus-tunable electrowetting optofluidic lens". In: *Optics express* 26.20 (2018), pp. 25839–25848.

[90] Daniel Kopp and Hans Zappe. "Tubular astigmatism-tunable fluidic lens". In: *Optics letters* 41.12 (2016), pp. 2735–2738.

[91] Bahram Javidi and Takanori Nomura. "Securing information by use of digital holography". In: *Optics Letters* 25.1 (2000), pp. 28–30. URL: `https://www.osapublishing.org/abstract.cfm?uri=ol-25-1-28` (visited on 12/29/2016).

[92] Bahram Javidi et al. "Roadmap on optical security". In: *Journal of Optics* 18.8 (Aug. 2016), p. 083001. ISSN: 2040-8978, 2040-8986. DOI: 10.1088/2040-8978/18/8/083001. URL: http://stacks.iop.org/2040-8986/18/i=8/a=083001?key=crossref.166cb862d59298070bc1d965cecc2881 (visited on 12/29/2016).

[93] Joseph W. Goodman. *Statistical Optics*. 2nd ed. Hoboken, New Jersey: John Wiley and Sons, Inc., 2013. ISBN: 978-1-119-00945-0.

[94] Falk Töppel et al. "Classical entanglement in polarization metrology". In: *New Journal of Physics* 16.7 (2014), p. 073019.

[95] Alfredo Luis. "Coherence, polarization, and entanglement for classical light fields". In: *Optics Communications* 282.18 (2009), pp. 3665–3670. URL: https://doi.org/10.1016/j.optcom.2009.06.024 (visited on 02/11/2015).

[96] Bahram Javidi, Guanshen Zhang, and Jian Li. "Encrypted optical memory using double-random phase encoding". In: *Applied optics* 36.5 (1997), pp. 1054–1058. URL: https://www.osapublishing.org/abstract.cfm?uri=ao-36-5-1054 (visited on 12/29/2016).

[97] Bahram Javidi and Joseph L. Horner. "Optical pattern recognition for validation and security verification". In: *Optical engineering* 33.6 (1994), pp. 1752–1756. URL: http://opticalengineering.spiedigitallibrary.org/article.aspx?articleid=1073123 (visited on 12/29/2016).

[98] Wen Chen, Bahram Javidi, and Xudong Chen. "Advances in optical security systems". en. In: *Advances in Optics and Photonics* 6.2 (June 2014), p. 120. ISSN: 1943-8206. DOI: 10.1364/AOP.6.000120. URL: https://www.osapublishing.org/aop/abstract.cfm?uri=aop-6-2-120 (visited on 12/29/2016).

[99] Hukum Singh. "Cryptosystem for securing image encryption using structured phase masks in Fresnel wavelet transform domain". In: *3D Research* 7.4 (2016), p. 34.

[100] Y. Xin R. Tao and Y. Wang. "Double image encryption based on random phase encoding in the fractional Fourier domain". In: *Optics Express* 15.24 (2007), pp. 16067–16079. URL: https://doi.org/10.1364/OE.15.016067 (visited on 02/11/2015).

[101] M. Pohit G. Unnikrishnan and K. Singh. "A polarization encoded optical encryption system using ferroelectric spatial light modulator". In: *Optics Communications* 185.1 (2000), pp. 25–31. (Visited on 02/11/2015).

[102] S. Liu and J. T. Sheridan. "Optical encryption by combining image scrambling techniques in fractional Fourier domains". In: *Optics Communications* 287 (2013), pp. 73–80. (Visited on 02/11/2015).

[103] Zhengjun Liu et al. "Image encryption algorithm by using fractional Fourier transform and pixel scrambling operation based on double random phase encoding". In: *Optics and Lasers in Engineering* 51.1 (2013), pp. 8–14.

[104] Myungjin Cho and Bahram Javidi. "Three-dimensional photon counting double-random-phase encryption". In: *Optics Letters* 38.17 (2009), pp. 3198–3201. URL: https://doi.org/10.1364/OL.38.003198 (visited on 02/11/2015).

[105] María S Millán Elisabet Pérez-Cabré Héctor C Abril and Bahram Javidi. "Photon-counting double-random-phase encoding for secure image verification and retrieval". In: *Journal of Optics* 14.9 (2012), p. 094001. URL: http://iopscience.iop.org/article/10.1088/2040-8978/14/9/094001/meta (visited on 02/11/2015).

[106] Elisabet Pérez-Cabré et al. "Photon-counting double-random-phase encoding for secure image verification and retrieval". In: *Journal of Optics* 14.9 (2012), p. 094001.

[107] Wan Qin and Xiang Peng. "Asymmetric cryptosystem based on phase-truncated Fourier transforms". In: *Optics Letters* 35.2 (2010), pp. 118–120. URL: https://doi.org/10.1364/OL.35.000118 (visited on 02/11/2015).

[108] Xiaogang Wang et al. "Discussion and a new attack of the optical asymmetric cryptosystem based on phase-truncated Fourier transform". In: *Applied optics* 53.2 (2014), pp. 208–213.

[109] Xiaoli Liu et al. "Vulnerability to ciphertext-only attack of optical encryption scheme based on double random phase encoding". en. In: *Optics Express* 23.15 (July 2015), p. 18955. ISSN: 1094-4087. DOI: 10.1364/OE.23.018955. URL: https://www.osapublishing.org/abstract.cfm?URI=oe-23-15-18955 (visited on 12/29/2016).

[110] Yann Frauel et al. “Resistance of the double random phase encryption against various attacks”. In: *Optics Express* 15.16 (2007), pp. 10253–10265. URL: https://www.osapublishing.org/abstract.cfm?uri=OE-15-16-10253 (visited on 12/29/2016).

[111] Kazuya Nakano et al. “Security analysis of phase-only DRPE based on known-plaintext attack using multiple known plaintext ciphertext pairs”. en. In: *Applied Optics* 53.28 (Oct. 2014), p. 6435. ISSN: 0003-6935, 1539-4522. DOI: 10.1364/AO.53.006435. URL: https://www.osapublishing.org/abstract.cfm?URI=ao-53-28-6435 (visited on 12/29/2016).

[112] J. Joseph G. Unnikrishnan and K. Singh. “Optical encryption by double-random phase encoding in the fractional Fourier domain”. In: *Optics Letters* 25.12 (2000), pp. 887–889. URL: https://doi.org/10.1364/OL.25.000887 (visited on 02/11/2015).

[113] Osamu Matoba et al. “Optical Techniques for Information Security”. In: *Proceedings of the IEEE* 97.6 (June 2009), pp. 1128–1148. ISSN: 0018-9219. DOI: 10.1109/JPROC.2009.2018367. URL: http://ieeexplore.ieee.org/document/4939407/ (visited on 12/29/2016).

[114] H. T. Chang H.-E. Hwang and W.-N. Lie. “Multiple-image encryption and multiplexing using a modified Gerchberg-Saxton algorithm and phase modulation in Fresnel-transform domain”. In: *Optics Letters* 34.24 (2009), pp. 3917–3919. URL: https://doi.org/10.1364/OL.34.003917 (visited on 02/11/2015).

[115] Bahram Javidi et al. “Error-reduction techniques and error analysis for fully phase- and amplitude-based encryption”. In: *Applied optics* 39.23 (2000), pp. 4117–4130.

[116] Matlab. *The Mathworks, Inc.* 2017. URL: http://www.mathworks.com/products/matlab.html.

[117] David George Voelz. *Computational fourier optics: a MATLAB tutorial*. SPIE press Bellingham, WA, 2011.

[118] Nasser Towghi, Bahram Javidi, and Z. Luo. “Fully phase encrypted image processor”. In: *JOSA A* 16.8 (1999), pp. 1915–1927. URL: https://www.osapublishing.org/abstract.cfm?uri=josaa-16-8-1915 (visited on 12/29/2016).

[119] Pramod Kumar et al. “Impulse attack free double-random-phase encryption scheme with randomized lens-phase functions”. In: *Optics letters* 34.3 (2009), pp. 331–333.